MICROFLUIDIC DEVICES AND SYSTEMS FOR NEUROSCIENCE STUDIES IN *Caenorhabditiselegans (C. elegans)*

by

Trushal Vijaykumar Chokshi

A dissertation submitted in partial fulfillment
of the requirements for the degree of
Doctor of Philosophy
(Electrical Engineering)
in The University of Michigan
2011

Doctoral Committee:

Assistant Professor Nikolaos Chronis, Co-Chair
Assistant Professor David D. Wentzloff, Co-Chair
Professor Kensall D. Wise
Professor Euisik Yoon
Assistant Professor Jianping Fu

To My Family

In

India and Michigan (Michigan Family)

Table Of Contents

List Of Figures

List Of Appendices

ABSTRACT

C. elegans, a tiny, transparent roundworm with a simple nervous system (302 neurons) and a diverse repertoire of behavioral outputs, has been extensively used as a model organism in neuroscience. Its optically accessible, compact nervous system offers a unique advantage for understanding the ability of the nervous system to compute various behaviors of an organism. *C. elegans*, however poses a challenge as a model organism – due to its small size (1 mm in length and 40 – 50 μm in diameter), conducting experimental procedures on the worm is skill-intensive and time consuming. To this end, microfluidic technology has recently emerged as a preferred tool for conducting experimental procedures on the worm, and this thesis contributes towards the development of such microfluidic approaches.

We demonstrated the design and development of microfluidic devices and systems that serve the following applications :

a) Immobilization - We developed two microfluidic approaches for immobilizing *C. elegans* on-chip. These approaches are easy to implement, allow worm recovery within a few seconds after immobilization and can be easily adopted for conducting cell developmental and neuron regeneration studies in *C. elegans*.

b) Calcium Imaging - We developed an automated microfluidic platform for collecting stimulus-evoked calcium imaging data from single neurons. We utilized the platform to monitor neural activity in the chemosensory neuron - ASH - in response to different stimuli (chemical and electrical) and characterized its dependence on the age of the worm. The platform enabled us to hypothesize that the neuronal functionality is altered with age.

We believe that the microfluidics/imaging approach will allow the observation of large scale neuronal dynamics in *C. elegans*. Consequently, we foresee the use of computational procedures for uncovering new insights about the worm's nervous system. To this end, we propose a hardware based computational platform for emulating the worm's nervous system. And, as a step towards this futuristic goal, we present an analog circuit that emulates the observed ASH neuronal activity in *C. elegans*.

We envision that the work demonstrated in this thesis will expand the toolsets available for conducting neuroscience studies in *C. elegans*.

CHAPTER 1

INTRODUCTION

1.1 Motivation

How do individual neural circuits communicate with each other in a biological neural network? How does the sensory information get transduced into a behavioral response in an organism? What are the underlying biological processes that control the development of these neural circuits? Answers to these fundamental questions hold the key for comprehending the biological computational platform – The Nervous System.

In order to unravel the mysteries of the nervous system, neuroscientists rely on different types of animal models that includes vertebrate (Rodents [1, 2], Zebrafish [3], Chick [4, 5] and Xenopus [6]) and invertebrate (*C. elegans* [7], Drosophila [8], Ascaris [9, 10] and Cephalopods such as Squids [11]) organisms. The decision to use a particular animal model is typically based on its validity and simplicity in conducting experimental studies for answering specific research questions. To understand the functional role of neurons – i.e., how a neuronal network processes information to generate a particular behavior – it is critical to decode the signals from individual neurons and correlate them with the organism's behavior. And order to do so, the challenge is to find a model species that not only displays interesting behavior but also has an easily accessible nervous system. One such model species is the nematode *C. elegans*.

C. elegans is a free living, transparent nematode (roundworm), about 1 mm in length and lives in temperate soil environments [12]. The key features that make this organism ideal for many neuroscience studies are :

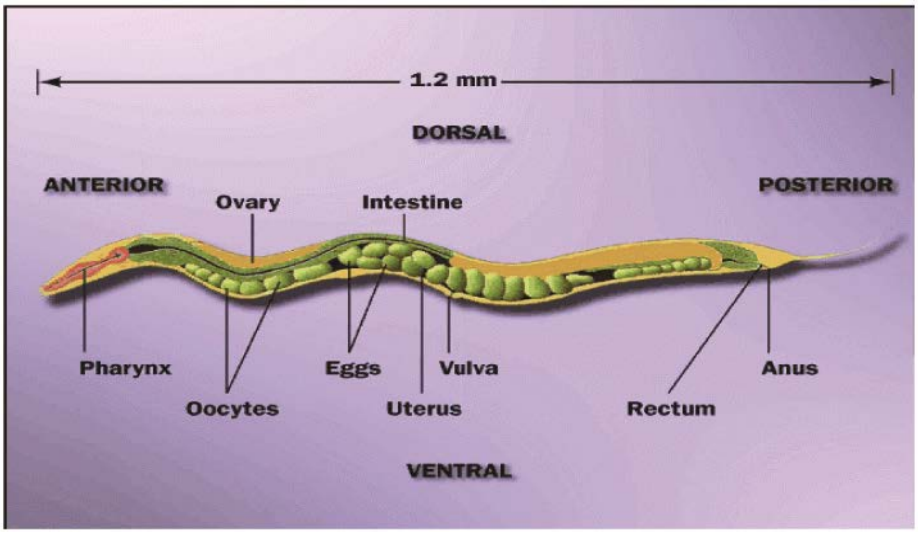

Figure 1.1: Image of *C. elegans* [adapted from [1]].

- It is the first multicellular organism to have its genome completely sequenced. Its development is characterized better than any multicellular organism, i.e., the developmental pattern of each somatic cell – from zygote to the adult worm – is known. In other words, one can know the fate of a particular cell at any point in its developmental period [12].
- It is a eukaryote organism, implying that its cellular and molecular structures and control pathways are similar to that of other higher organisms. Of particular interest, is that, about 40-50% of its genes have human homologs. Thus, the biological information learned from *C. elegans* may apply to humans as well [12].
- *C. elegans* is one of the simplest organisms with a diverse repertoire of behavioral outputs and a very well defined nervous system. Its nervous system comprises 302

neurons whose pattern of connectivity has been completely mapped out. In fact this is the only animal for which the complete ‘wiring diagram’ of the nervous system is known [12].

To summarize, the diverse repertoire of behavioral outputs, genetic conservation with higher organisms and an optically accessible compact nervous system, make *C. elegans* an ideal organism for studying the ability of the nervous system to compute the behavior of an entire organism. Next, we review the conventional techniques used for studying the worm’s nervous system.

1.1.1 Techniques for studying *C. elegans* nervous system.

(A) Behavioral Genetics

Traditionally, behavioral genetics has been employed as a prime method for neurobiological studies in *C. elegans* [13]. With the availability of a detailed database of the nematode’s genome and the ease of transgenesis, it has been possible to decipher the molecular and cellular basis of behavior. Mutants with abnormal behavior are used to identify the genetic basis underlying neural development, sensory perception, motor activity, etc. This, combined with laser ablation studies, has further helped to elucidate the role of individual neurons in governing the behavior. Thus, behavioral genetics can be a great tool for indirectly measuring the activity and decoding the role of individual neuronal cells in *C. elegans*.

However, to understand the functional role of neurons, it is also important to comprehend the manner in which their spatial and temporal activity patterns correlate

with the behavioral events. Further, it is desirable to determine the effect of a particular gene on the functional properties of neurons. And, the use of behavioral genetics has significant limitations for conducting such studies. To address these questions, neurophysiologists have developed a few other techniques as discussed below.

(B) Electrophysiology

Electrophysiology is a technique for electrically recording the neural activity in an organism and by far this approach has been the only way of directly measuring the neurophysiological parameters, *in-vivo* in most organisms. Few electrophysiological preparations that have been implemented for *C. elegans* neural recording include the measurement of ionic conductances in neurons and at neuromuscular junctions, mediated by nicotinic acetylcholine receptors [14], GABA receptors [14], glutamate receptors [15], voltage gated calcium channels [16] and mechanosensory transduction channels [17]. Although successful, its use with respect to *C. elegans* has been very limited because of the following reasons:

- *The presence of a hydrostatic skeleton [12]: C. elegans* body is enclosed by a tough proteinaceous cuticle which presents a highly resilient barrier to the recording electrode. Due to this, the nematode must be dissected in order to access its neurons. However, nematode dissections often result in disrupting its hydrostatic skeleton, making *in vivo* electrical recordings difficult to succeed.
- *Small-sized cell bodies [12]:* The size of the nematode's neuronal cell body is only a few microns in diameter (2-4 μm). Thus, even if the nematode is dissected

successfully, probing the neuronal cell body with an electrode is a significant challenge.

(C) Optical imaging

As opposed to electrophysiology, optical imaging is a less invasive technique for monitoring the neuronal activity in biological organisms. This technique allows monitoring the amount of Ca^{2+} inside a cell without dissecting the organism's body and is based on the use of molecules known as calcium indicators that can respond to the binding of Ca^{2+} ions by changing their spectral properties. The structure of these calcium indicators typically comprises three domains, which include, 1.) Fluorescent chromophores such as GFP, 2.) calcium binding proteins (such as calmodulin) and 3.) peptide molecules that can bind to the calcium binding proteins (such as M13 - a synthetic peptide that can bind to calmodulin). When the calcium binding domain binds to calcium, it initiates a conformational change in the entire molecule and hence results in a change in its spectral properties.

The neuronal dynamics *in vivo* in *C. elegans* are monitored through the use of a special class of calcium indicators known as Genetically Encoded Calcium Indicators (GECI). The most widely used calcium indicators for monitoring *C. elegans* neuronal activity can be categorized into two types (Type I and Type II) based on the mechanism they employ to sense Ca^{2+} ions. Upon binding to calcium, Type I indicators (such as GCaMP [18]) directly change their spectral properties, while Type II indicators (such as Cameleon [19]) change their spectral properties via the phenomenon of FRET

(Fluorescence Resonance Energy Transfer). The use of such calcium sensitive probes for monitoring the worm's neuronal activity has been feasible because of two key reasons:

- *Presence of calcium channels [12]:* Calcium fluctuations inside the neuron are indicative of the worm's neuronal excitability [16]. And, the calcium based optical probes offer a great tool for monitoring the calcium transients associated with the neuronal activity.
- *Optical Transparency [12]:* The transparent body of *C. elegans* allows optical recordings without any dissections. Hence, the neuronal activity can even be monitored during its normal behavior.

As can be seen, each of the techniques described above have advantages and disadvantages, and thus their use for studying the worm's nervous system generally depends on the specific research question to be answered. However, one common need and bottleneck of the experimental procedures utilized for implementing these techniques, is the precise manipulation of the worm. For example, immobilizing and stimulating the worm are two typical manipulation steps. Traditional methods immobilize the worm by either gluing it on a substrate [20, 21] or by anesthizing it [22]. Although successful, these methods are very laborious, skill intensive and low-throughput. Similarly, methods for stimulating the worm include the use of fluid-filled pipettes (for delivering chemical stimuli) [21], temperature controlled plates (for delivering thermal stimuli) [23] or sharp probes (for delivering mechanical stimuli) [24]. Despite the initial success, these methods do not allow a precise control over the stimulation parameters or over the worm's micro-environment.

1.2 Thesis Objective

In order to conduct neuroscience studies in *C. elegans*, experimental methodologies need to be developed that would be simple to implement, not be skill intensive and allow precise manipulation of the worm and its micro-environment. This thesis aims at utilizing the potential of microfluidic technology for developing such methodologies.

1.2.1 Microfluidic technology

The field of microfluidic engineering deals with the precise control and manipulation of fluids in a system of channels, typically sub-millimeter in dimensions. The technology provides a junction between engineering and pure sciences with an immense potential for offering simple and practical solutions for applications in the field of ‘genomics’, ‘proteomics’ and ‘cellomics’. These applications primarily include molecular biology procedures for enzymatic and DNA analysis, clinical pathology, biochemical sensing of toxins and many other protocols, routinely executed in a biological laboratory. Previous work has shown the development high-density microfluidic devices that integrate a number of microfluidic modules (valves, multiplexers, microchambers and pumps) and enable complex on-chip integrated functionality [25]. These devices are becoming a preferred tool for single cell studies as they allows the integration of the cell-analysis process steps (eg. selection, lysis, separation, detection of cellular analytes, etc) on a common platform. Several microfluidic devices for trapping, stimulating and analyzing single cells and embryos have been reported in the literature [26].

Moving a few dimensions above single cell studies, microfluidics has also been adopted for tissue engineering and culturing experiments. Microfluidic scaffolds have been designed to house the tissue cells in well defined 3D environments and control their extracellular chemistry. Scaffolds equipped with microfluidic bioreactors have allowed the control of global mass transfer to the cell surface [27] and to their bulk through perfusion [28]. Scaffolds embedded with sophisticated microfluidic networks have also been reported that allow control over the spatial and temporal delivery of different metabolites and signals in the bulk of 3D cell cultures [29].

Starting from applications concerning single cell studies to tissue engineering and culturing experiments, the wave of microfluidic technology is now seen to extend its contribution towards whole-animal studies also. An appropriate example in this aspect is the introduction of microfluidic devices for conducting *C. elegans* research studies. Here, we intend to utilize microfluidics for conducting neuroscience studies in *C. elegans*. This thesis aims at achieving the following objectives:

1.2.2 Research goals

1. To realize microfluidic approaches for immobilizing and imaging C. elegans

Immobilization of the worm is a critical step for research studies that include laser ablation of the neuron, imaging stimulus-evoked neuronal responses, analyzing the nematode's anatomical features and imaging cellular development. However, the conventional immobilization techniques are labor and time intensive (thus low-throughput), toxic and moreover, not amenable to automation. Here, we aim to develop

microfluidic approaches for immobilizing and imaging the worm. These methods should be simple to implement, not be skill intensive, non-toxic, allow precise worm manipulation and amenable to computer automation.

2. *To build a microfluidic-based platform for high-throughput calcium imaging in C. elegans*

Calcium imaging is a powerful technique for monitoring the neuronal activity in *C. elegans in-vivo* at a single cell level, as well as at a whole organism level. However, the conventional experimental methods for calcium imaging are low-throughput and thus impractical for collecting calcium imaging data from a large population of worms – typically required while identifying statistically significant trends or eliminating stochastic variations in the data. Here, we aim to develop an automated microfluidic platform for performing high-throughput calcium imaging in *C. elegans*. Such a platform could possibly enable novel, high-throughput functional-imaging based screening assays platform could also enable novel, high-throughput functional-imaging based screening assays.

3. *To utilize the high-throughput calcium imaging platform developed in 'Aim 2' for conducting aging studies in C. elegans*

C. elegans has been used as a model organism for several aging studies. These studies have unveiled over a hundred aging-related genes and several of them have been shown to be expressed in the sensory neurons. This suggests that the nervous system might be affected by aging. However, to date, the effect of aging on the functionality of

the worm's nervous system is not known. Here, we intend to utilize the high-throughput calcium imaging platform described in 'Aim 2' to study the effect of aging on the biophysical properties of the worm's nervous system.

4. To realize a hardware-based platform for modeling C. elegans nervous system

Hardware based emulation of the nervous system has long been envisioned as a computational platform for real-time simulation and investigation of biological neural networks. We believe that, compared to other model organisms, the development of such a computational platform for *C. elegans* nervous system is a feasible goal because : a) it has a simple nervous system (302 neurons with approximately 7000 synapses), and b) there exists a complete description of the morphology and synaptic connectivity of its entire nervous system. We foresee the use of such a platform as a tool for uncovering new insights about the connections, architecture, and overall functionality of worm's nervous systems. As a small step towards this futuristic goal, here we aim to design a transistor level circuit to emulate the response characteristics of the *C. elegans* chemosensory neuron - ASH.

1.3 Thesis Organization

The work presented in this thesis is organized as follows :

Chapter 2 – Literature Review

This chapter reviews the recent development of microfluidic devices for *C. elegans* research studies.

Chapter 3 – Microfluidic Approaches For Immobilizing C. elegans On-Chip

This chapter presents two different microfluidic approaches for immobilizing *C. elegans* and characterizing its behavior on-chip. A microfluidic device was fabricated using soft lithography to implement these approaches. We demonstrate the applicability of the proposed approaches for performing laser ablation of individual neurons and for conducting cellular developmental studies in the worm.

Chapter 4 – A Microfluidic Platform For High-throughput Calcium Imaging In C. elegans Chemosensory Neurons Using Chemical Stimulation.

This chapter presents a microfluidic-based platform for monitoring the worm's neuronal activity in a high-throughput fashion. The platform immobilizes individual worms, delivers a chemical odor to their nose and collects calcium imaging data from single neurons without any manual intervention. We utilize the platform to study the effect of aging on the functionality of the chemosensory neuron – ASH.

Chapter 5 – Probing The Physiology Of ASH Neuron In C. elegans Using Electric Current Stimulation.

This chapter demonstrates the use of electric current stimulation as a technique to probe the nervous system of *C. elegans*. We utilize a modified version of the automated microfluidic platform described in chapter 4 to acquire calcium imaging data from the ASH chemosensory neuron in response to electric currents of varying strengths and polarities. We also present a first-order differential equation model to describe and quantify the electrical stimulation evoked ASH response. We further demonstrate that

electric current stimulation can also be used to study the effect of aging on neuronal functionality in *C. elegans*.

Chapter 6 – Hardware-based Emulation Of The Functionality Of The ASH Chemosensory Neuron In C. elegans.

This chapter presents a transistor level circuit that emulates the characteristic response of the ASH chemosensory neuron. The circuit is designed to implement the differential equation model presented in Chapter 5 that described the characteristic response of the ASH neuron. Practical realization of this circuit is shown by implementing it on a breadboard.

Chapter 7 – Conclusions and Future work

This chapter summarizes the work demonstrated in this thesis and presents the potential future directions.

CHAPTER 2

Literature Review

This chapter presents a family of microfluidic devices that have been designed for the manipulation and imaging of *C. elegans*. These devices are categorized on the basis of a class of application areas they serve, namely, i) Behavioral studies, ii) Genetic screening and iii) Neural functional imaging.

2.1 Introduction

The recent development of microfluidic devices for the precise manipulation of *C. elegans* and its micro environment has opened new avenues for experiments ranging from, studying the worm's behavior in a controlled environment to imaging its neuronal activity *in vivo* and to high-throughput genetic screenings for neurobiological studies. These devices hold several key features that make their use ideal for *C. elegans* studies : first, the technique of soft-lithography has made the fabrication of these devices simple and cheap; second, these device are made up of optically transparent materials such as glass or poly-dimethyl-siloxane (PDMS) which allows to perform optical imaging of experiments; third, the laminar fluid flow inside micro sized channels, allows to easily manipulate worm's micro environment and deliver fluid-borne stimuli with immense

precision; and lastly, these devices can be easily scaled to handle a large population of worms either in parallel or in series (via computer automation) for several high-throughput studies. Here, we review various microfluidic devices used for *C. elegans* studies. These devices are categorized on the basis of the class of application areas they serve, which are i) Behavioral studies, ii) Phenotyping and morphology-based screenings, iii) Neuronal functional imaging and iv) Nerve regeneration studies.

2.2 Microfluidic devices for *C. elegans* studies

2.2.1 Devices for behavioral studies

The worm's behavior reflects the activity of its nervous system, which is dependent on factors such as the neuronal structure, external stimuli, past experience and changes in worm's internal body environment. For this reason, behavioral assays provide a simple and powerful tool to interrogate neuronal function in *C. elegans*. *C. elegans* behavioral assays comprise a wide range of behaviors and methodologies to study them. Some of the typical behaviors investigated in *C. elegans* behavioral assays include, mechanosensation, osmotic avoidance and chemosensation.

Mechanosensation behavioral assays involve studying the worm's behavior in response to mechanical stimuli. These stimuli include a gentle touch stimulus delivered to worm's body or a harsh touch stimulus delivered either to the midbody, head or tail of the worm. Gentle touch stimulus is usually delivered by stroking the worm with an eyebrow hair by tapping the agar plate in which they reside, while a harsh touch stimulus is

delivered by prodding the worm with a platinum wire [24]. Osmotic avoidance behavioral assays involve studying the worm's avoidance response to high osmolarity (an environment with concentrated solutions). To conduct this assay, the worms are placed inside a high osmotic barrier which is formed by creating a high osmolarity disc shaped region on the agar plate. The rate at which the worms cross the osmotic barrier indicates the degree of osmotic avoidance [30]. Chemosensation behavioral assays investigate the worm's ability to sense different chemical odors. The chemical odors are delivered either by diffusion of odor molecules from a droplet source on the agar plate or by dissolving the chemical inside the agarose medium [31]. *C. elegans* also display electrosensory [32, 33] behavior. This behavior, termed as electrotaxis involves the directional locomotion of *C. elegans* towards the negative terminal in an electric field. Combined with molecular genetics, electrophysiological and optical recording techniques, these assays have been very successful in assessing the contribution of specific genes and neurons to the worm's behavior. However, the use of these assays is limited due to their extreme sensitivity to small variations in assay conditions, which are difficult to control using the conventional methodologies.

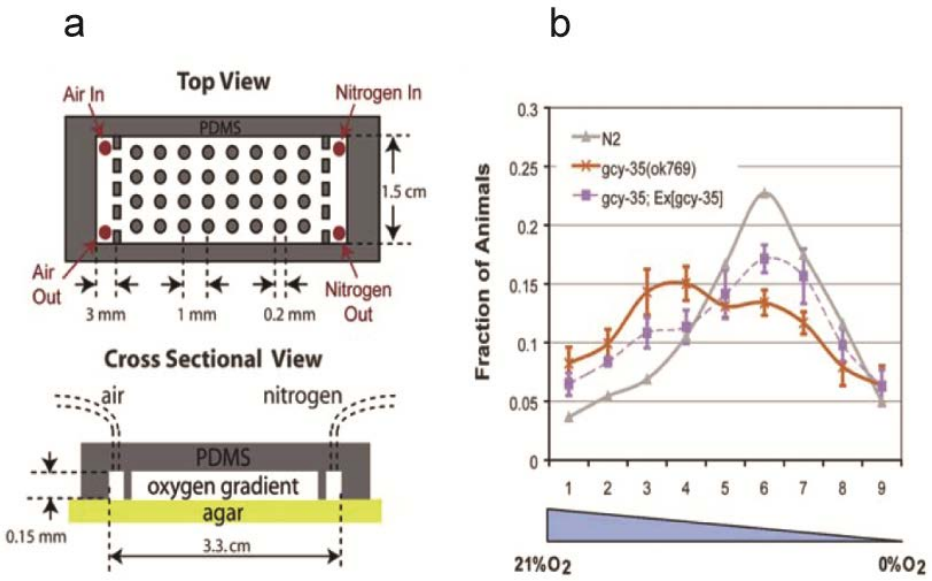

Figure 2.1: A microfluidic chip for studying oxygen sensation in *C. elegans* [adapted from [34]]. **(a)** Top and cross sectional view of the device. A 0-21% oxygen gradient is created by passing air and nitrogen into the device. **(b)** Wild-type worms that are allowed to navigate through the oxygen gradient are observed to avoid hyperoxic environments. Mutant worms lacking GCY-35 protein (red curve) are observed to be defective in hyperoxia avoidance.

To address this problem, several groups have recently utilized microfluidics for worm behavioral studies. A microfluidic device (**Figure 2.1**) has been developed to generate precise oxygen concentration gradients on-chip for conducting chemosensation and osmotic avoidance behavioral assays [34]. The worms are allowed to navigate through these gradients to identify the most attractive concentration value. Microfluidic mazes with concentration gradients comprising multiple chemical compounds or odors have also been created for studying learning behavior in worms [35, 36]. Besides creating controlled micro-environments, microfluidics based behavioral assays allow optical quantification (due to the transparent nature of PDMS) of the worm's behavioral patterns. An example of this is a droplet-based microfluidic design (**Figure 2.2a**) for studying the

worm's swimming behavior [37]. Here, individual worms are isolated and transported by encapsulating them in nanoliter oil droplets. The worms are then imaged by passing the oil droplets through the field of view of the imaging setup. Another mircodroplet based design (**Figure 2.2b**) has also been reported for monitoring the worm's locomotion in response to temporal variations of odorants [38]. Here, single worms were confined in an array of microdroplets and their swimming behavior was quantified in response to an odorized airstream flown over the microdroplets. Such a design enabled to characterize the temporal dynamics of the worm's olfactory response and its sensitivity to the concentration and gradients of the odorant. Microdroplets and microchambers [39] have also been utilized to maintain worms for their entire lifespan. Such devices have enabled to determine the age-related changes in the worm's behavioral responses.

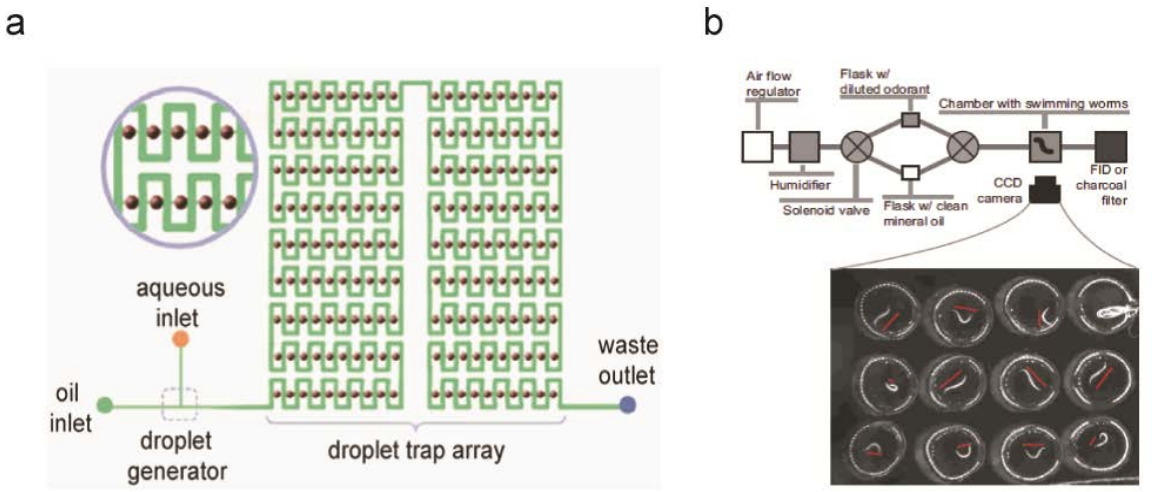

Figure 2.2: (a) Schematic representation of a droplet-based microfluidic design for studying worm swimming behavior [adapted from [37]]. The device comprises a T-junction droplet generator and a droplet trap array. The droplets are generated by shearing an aqueous phase with a constant oil phase at the T-junction. Individual worms are encapsulated into these droplets and then trapped inside the droplet trap array. This device has been used to study the worm behavior in response to neurotoxins at single-animal resolution. **(b)** Schematic of the microdroplet system designed to quantify the stimulus-evoked swimming behavior of worms [adapted from [38]]. Single worms are confined within the droplets while a stimulus is delivered to them by flowing an odorized

airstream over the droplets. The behavior of individual worms is recorded with a CCD camera.

A few other microfluidic architectures that are designed to mimic the worm's natural environment have been used for mechanosensation behavioral assays [40]. These devices consist of an array of obstacles (e.g. microfluidic posts) or special-shaped microfluidic channels patterned on agar or PDMS substrate (**Figure 2.3**). They have been used to study detailed worm locomotion characteristics (e.g. body curvature, speed and frequency) and other novel locomotion patterns that might have been missed in conventional behavioral assays. Additionally, micro devices incorporating MEMS elements such as piezoresistive cantilevers and posts have been fabricated and used for measuring forces generated during locomotion or for studying the mechanical properties of the worm cuticle [41, 42].

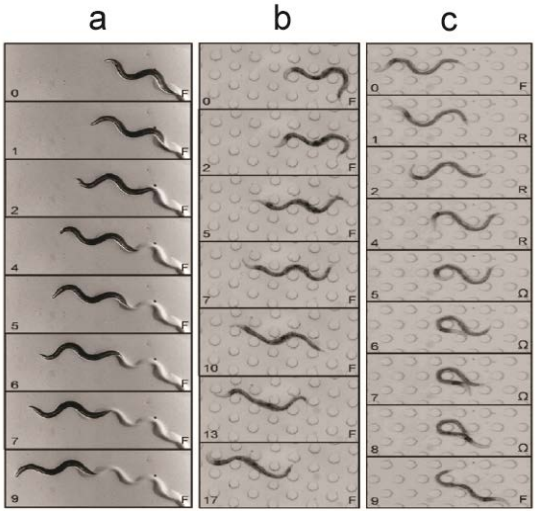

Figure 2.3: Comparison between the worm's locomotion behavior on agarose **(a)** and in the artificial soil device **(b&c)** [adapted from [40]]. The values shown on the lower left of each frame indicate the elapsed time (sec), while the letters on the lower right indicate the behavioral state of the worm (F. forward; R, reverse and Ω, omega-turn). The artificial soil device shown in B&C comprises a regular array of uniformly shaped posts. These devices have enabled to observe the worm's locomotion behavior in substrates that are

more complex and closely related to the worm's natural environment than an agarose surface.

Microfluidic device designs (**Figure 2.4**), equipped with electrodes have been reported for studying the worm's electrosensory/electrotactic behavior [43, 44]. These devices have been used to characterize the worm's locomotion in the presence of DC [43] as well as AC [44] electric fields. In the presence of DC electric field, worms of different ages have been observed to navigate towards the negative terminal at different speeds. This behavior has been utilized to sort worms based on their age. On the other hand AC electric fields have been shown to constrain the worm's navigational behavior and have been employed to confine the worm within a particular region in the microfluidic channel.

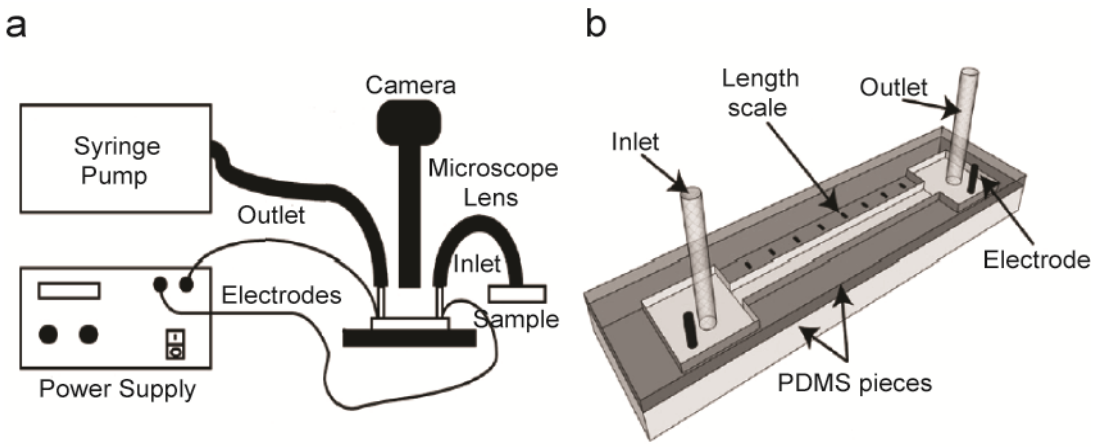

Figure 2.4: (a) Schematic of the experimental setup used to study the worm's electrotactic behavior. The setup comprises of, i) a worm handling unit (microfluidic device and syringe pump), ii) worm observation unit (microscope lens and the camera) and iii) worm stimulation unit (power supply and electrodes). **(b)** Microfludic device comprises a microchannel with embedded electrodes for electrical stimulation. [adapted from [43]].

2.2.2 Devices for genetic screens

A genetic screen is a procedure to identify and select individuals possessing a desired phenotype, where, a phenotype is defined as an observable characteristic or trait of an organism. Typical phenotypes in neural development and cell biology studies include morphology of cells and subcellular structures such as synapses or organelles. The availability of genetically encoded fluorescent markers along with the amenability of *C. elegans* to molecular genetics and an optically transparent body has made fluorescence morphology based phenotyping as a prime method for performing *C. elegans* genetic screens. Traditional methods used for performing these screens involve several worm handling steps that are manual, serial and non-quantitative in nature.

To address these problems, microfluidics has recently been adopted for performing fluorescence morphology based genetic screens in *C. elegans*. An automated microfluidic system has been designed for high-throughput genetic screens, sorting and gene-expression pattern analysis [45]. The microfluidic device incorporated into this system is shown in **Figure 2.5**. Depending on the phenotype to be screened, this system is able to reliably screen and sort hundreds to thousands of worms in one hour. An on-chip cooling methodology allows to immobilize individual worms and enables high resolution imaging of cellular and subcellular structures such as axons, dendrites and synapses. Genetic screening with EMS (Ethyl Methanesulphonate)-mutagenized worm population was also demonstrated using such an automated system [46]. A few other microfluidic architectures that have been proposed for *C. elegans* genetic screening include, an array of microfluidic clamps that can simultaneously immobilize thousands of

worms [47] and a design that utilizes an intricate sequence of valve actuation schemes for performing multistep worm manipulation [48].

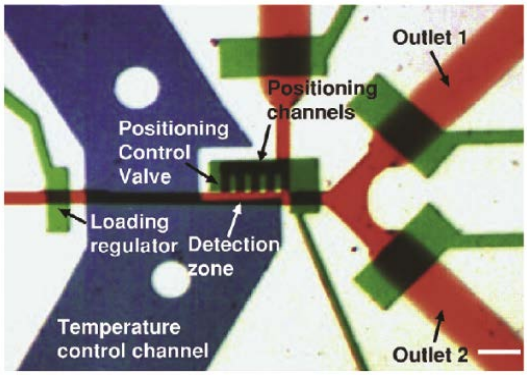

Figure 2.5: A two-layer PDMS microfluidic device for phenotyping and sorting of *C. elegans* [adapted from [45]]. Red represents the channels used for loading and unloading the worms, green represents the microfluidic valves and blue represents the temperature-control fluid. A mixed population of worms is loaded into the loading module by a constant pressure-driven flow. A microfluidic valve (the loading regulator) is used to allow individual worms to enter the immobilization module. The worms are immobilized by passing a coolant fluid through the temperature control channel. The immobilized worms are imaged, phenotyped and then sorted by unloading them through one of the channels in the sorting module (Outlet 1 or Outlet 2).

2.2.3 Devices for neuronal functional imaging

The development of genetically encoded fluorescent calcium indicators has made calcium imaging a prime method for studying *C. elegans* neural activity. A typical experimental setup for calcium imaging involves gluing the worm onto a hydrated agar pad and stimulating it with a chemical, mechanical or thermal stimuli [21, 49]. Traditional methods for delivering these stimuli include the use of fluid-filled pipettes (for chemical stimuli), temperature controlled plates (for thermal stimuli) or sharp probes (for mechanical stimuli). Although successful, these methods do not allow a precise spatiotemporal control of the stimulus. Further, concerns arise on the toxicity of the glue to the functionality of the nervous system. And most importantly, the glue procedure does

not permit most of the behaviors to be generated or correlated to the neuronal activity in real time.

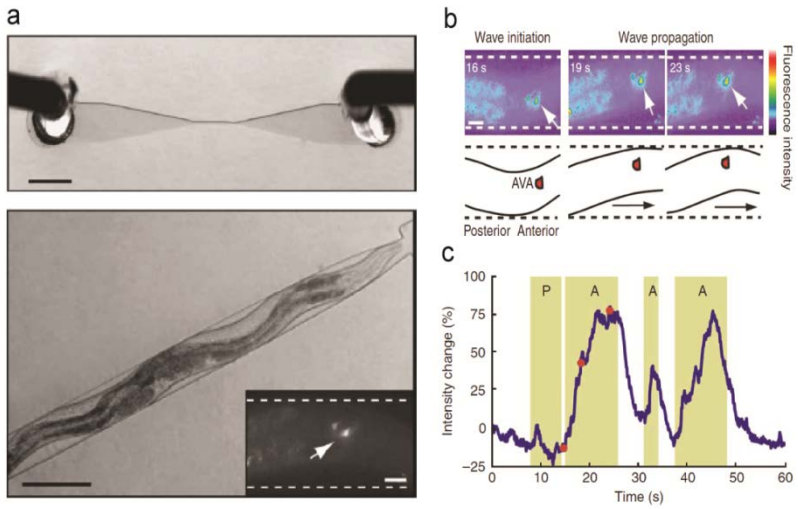

Figure 2.6: Microfluidic chip for correlating the worm's locomotion patterns with neuronal activity [adapted from [50]]. **(a)** The microfluidic chip (top) with a trapped worm (bottom). This chip was used to investigate the role of AVA interneuron in governing the worm's locomotion. Inset shows the fluorescence image of an AVA interneuron expressing fluorescent marker – G-CaMP. **(b)** Pseudocolor images showing changes in the G-CaMP intensity in AVA interneuron when the worm moves backwards or in other words, generates a posterior to anterior travelling body wave. **(c)** Plot shows the G-CaMP intensity changes corresponding to the anterior-travelling (A) and posterior-travelling (P) body waves.

To overcome these problems, several microfluidic devices have been developed for monitoring stimulus evoked neuronal activity in behaving worms. A microfluidic device, termed as the "behavior chip" (**Figure 2.6**) has been developed to correlate the worm's neural activity with its locomotion behavior [50]. This device comprises a micro channel to trap and image individual worms. The channel trap is designed to be slightly larger than the size of the worm so as to allow the worm to crawl in its typical sinusoidal pattern but not let it escape out of the field of view. This device was used to investigate the role of interneurons in governing the worm's locomotion.

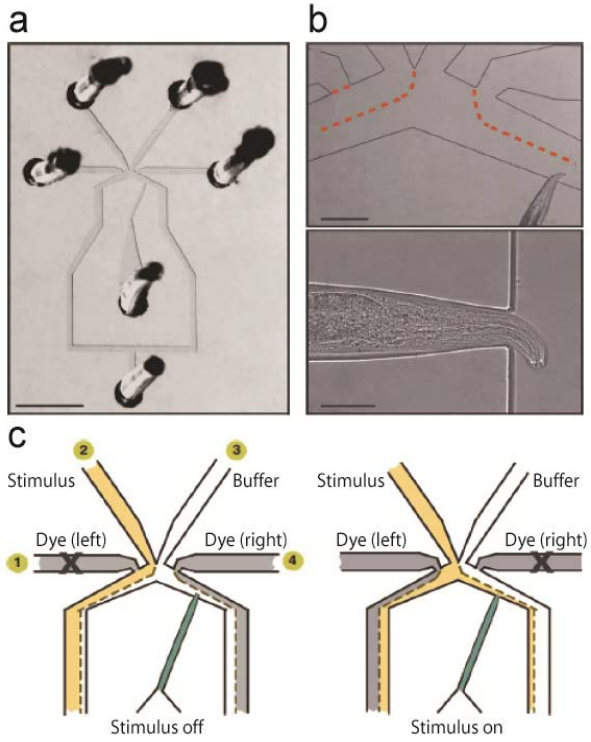

Figure 2.7: The 'olfactory' chip [adapted from [50]]. **(a)** The microfluidic device consists of a worm trap and a four-flow architecture for precisely delivering a stimulus to the worm's nose. The four-flow architecture consists of 2 side channels (channels 1& 4), a stimulus channel (channel 2) and a control channel (channel 3). **(b)** A high magnification image of the chip with a trapped worm. **(c)** Operation principle of the 'olfactory' chip. The stimulus is delivered over the worm's nose by switching the fluid-flow in the two side channels. In the 'off' state (left), the right side channel is open and the stimulus stream is pushed away from the nose of the worm. In the 'on' state (right), the left side channel is open and the stimulus is pushed towards the nose of the worm.

Another device, termed as the "olfactory chip" (**Figure 2.7**), was developed to study stimulus-evoked neuronal responses in *C. elegans* [50]. This device features a worm-sized trap and a four-channel microfluidic architecture which is designed to precisely deliver a chemical stimulus or an odor to the worm's nose. This device was used to monitor stimulus-evoked (1M glycerol) response of chemosensory neurons and it revealed new patterns in their response that were not observed in previous experiments. This device has also been used to decipher information processing strategies in a network

of olfactory neurons and interneurons that control food and odor evoked behaviors in the worm [51]. A variant of 'olfactory chip' (**Figure 2.8**) integrates a worm trap and a thin-gas permeable membrane with a two-layer architecture to deliver a gas stimulus to the worm [52]. This device was utilized to identify the molecular basis of rapid O_2-dependent behavior through calcium imaging of two distinct classes of O_2-sensitive neurons.

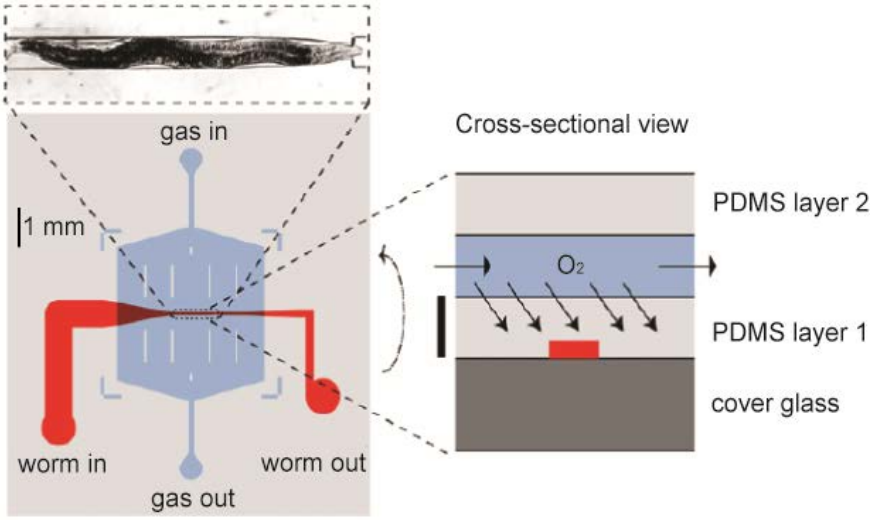

Figure 2.8: A two-layer microfluidic chip for studying the neuronal basis of oxygen sensation in *C. elegans* [adapted from [52]]. Microfluidic chip with a trapped worm (left) and its cross section (right). Red represents the channel used for trapping the worm while blue represents the overlying channel that is used for flowing O_2. This device was used for measuring the neural activity of BAG and URX neurons in response to different oxygen concentrations.

2.3 Conclusion

This chapter reviewed various microfluidic devices and systems that address the needs and bottlenecks of *C. elegans* research studies that included performing behavioral assays, genetic screening and neuronal functional imaging. The use of microfluidics for *C. elegans* research studies has not only eliminated the problems with conventional methodologies, but also revealed results that were not observed previously. The union of

microfluidics and *C. elegans* research studies seems poised to accelerate neurobiological studies in the worm and open new avenues for experiments that were not possible with conventional methods.

CHAPTER 3

Microfluidic Approaches For Immobilizing *C. elegans* On-Chip

This chapter presents two microfluidic approaches for immobilizing the roundworm *C. elegans* on-chip. The first approach creates a CO_2 micro-environment while the second one utilizes a deformable PDMS membrane to mechanically restrict the worm's movement. An on-chip 'behavior' module was used to characterize the effect of these methods on the worm's locomotion pattern. Our results indicate that both methods are appropriate for the short-term (minutes) worm immobilization. The CO_2 method offers the additional advantages of long-term immobilization (1-2 hours) and reduced photobleaching if fluorescent imaging during immobilization is required. We envision the use of these methods in a wide variety of biological studies in *C. elegans*, including cell developmental and neuronal regeneration studies.

3.1 Introduction

C. elegans has been a powerful model organism for studying the genetics of various biological processes, extending from cell apoptosis and aging to neural plasticity and mating behavior [53-56]. Immobilization of this tiny worm (~40-50 μm in diameter and 1 mm long) constitutes an important step for performing laser ablations of neurons for studying neuronal networks and axon regeneration [57-59], monitoring neuronal responses at the presence of various stimuli [60], analyzing the nematode's anatomical

features [61] and imaging cellular development and gene expression [62]. Conventional techniques for immobilizing the worm typically incorporate the use of glue [20, 21] or anesthetic compounds [22]. Although, such methods have been successfully used in the past, they have certain limitations. The ‘glue’ method is a single-worm and therefore labor-intensive, low-throughput technique that makes the immobilization of a large number of worms impractical. Moreover, it is not a reversible process as the worm cannot be released once glued. On the contrary, anesthetic compounds can be used to immobilize large population of worms, but their effects on the worm’s neuro-muscular system and their overall toxicity is unknown. This is an important limitation especially when the worm needs to be recovered and further studied [63]. Therefore, novel immobilization techniques that are reversible, minimally toxic and easy to implement would be a great tool for better understanding the various biological process in *C. elegans* as well as for performing experiments in a large population of worms.

Here, we present two microfluidic approaches for the short-term(minutes) and long-term(1-2 hours) immobilization of *C. elegans* on-chip and characterize the effect of these methods on the worm’s behavior. The two approaches that we explored were :

(i) The first approach creates a CO_2 micro-environment to cease the worm’s movement and it proved to be efficient for the long term worm immobilization (1-2 hours).

(ii) The second approach utilizes a deformable membrane to mechanically restrict the worm and it is appropriate for immobilizing the worm for shorter periods of time (minutes).

Both techniques can be used to immobilize worms of different age groups (L4's to adults). The proposed techniques are easy to implement and allow worm recovery within a few seconds after immobilization. Moreover, the device architectures of the two techniques allow optical access to the worm through a glass coverslip, and thus these techniques are compatible with high resolution optical microscopy.

3.2 Experimental Design

3.2.1 Microfluidic device design

The two immobilization techniques share the same microfluidic design and fabrication process. The design incorporates the well-established two-layer PDMS 'flow-control' channel architecture [64]. The device integrates two distinct modules (**Figure 3.1A**): (i) the 'behavior' module that is used to revitalize the worm after immobilization by mechanically stimulating it. It consists of a saw-shape microchannel that forces the worm to move in a sinusoidal pattern so that its locomotion can be further analyzed, (ii) the second module (**Figure 3.1B**), the 'immobilization' module, creates either a CO_2 micro-environment or mechanically compresses the worm ('compressive' immobilization) so that further manipulations (e.g. laser ablation) and imaging can be performed.

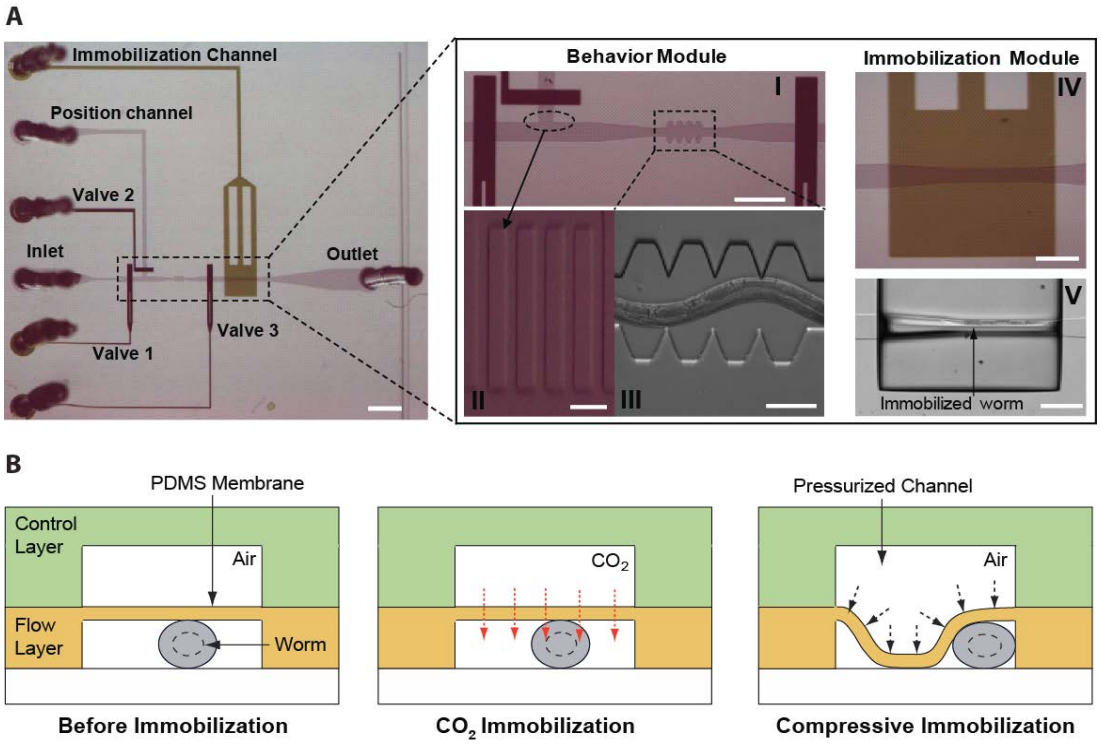

Figure 3.1: (A) The microfluidic device consists of the behavior (pictures I, II and III) and immobilization modules (pictures IV and V). The saw shape channel (III) is used to facilitate the revitalization of the worm and the on-chip quantification of the worm's locomotion pattern. PDMS pillars (II) do not allow the worm to enter the position channel. When high pressure (25 psi) is applied to the immobilization channel the worm is compressed on the microfluidic sidewalls (V). Scale bar, 1 mm (left picture). Scale bars are 300 μm, 500 μm, 10 μm, 100 μm, 300 μm for pictures I-IV respectively. **(B)** Immobilizing the worm by passing a CO_2 stream or by pressurizing the immobilization channel (control layer).

- **CO_2 immobilization**

The CO_2 micro-environment is created by passing pure CO_2 through the control layer and diffuses through the PDMS membrane into the flow layer. The high permeability of PDMS to nonpolar gases [65] results in the fast replacement of air with CO_2. The PDMS membrane is 30 μm thick and shows minimum deflection at moderate pressures (~69 kPa (10 psi)) exerted by CO_2.

- **Compressive immobilization**

The compressive immobilization approach utilized the deflection of a thin PDMS membrane to restrict the worm's movement, when high pressure (~172 kPa (25 psi)) is applied to the control channel. At such high pressures, the thin membrane (30 μm) collapses onto the worm squeezing it into the side of the microfluidic channel. In order to achieve large membrane deflections, a 20:1 PDMS mixing ratio is used for fabricating the flow layer. This reduces the PDMS elastic modulus by a factor of two when compared to the 10:1 ratio used for the flow layer in the 'CO_2 immobilization' device. The width of the microchannel in the immobilization module is made wider (110 μm) than the width of the saw-shape microchannel (90 μm) to allow large membrane deflections.

3.2.2 Experimental procedure

Worms are loaded into the main flow channel of the chip and manipulated by activating the integrated microfluidic valves (valves 1, 2 and 3 in Figure 3.1) via the control channel. A separate channel (the 'position' channel) perpendicular to the main loading channel was used to position the worm inside the behavior and immobilization modules. In order to prevent the worm from entering the position channel, PDMS pillars (**Figure 3.1A (II)**) are fabricated at its intersection with the loading channel.

To validate the effectiveness of proposed microfluidic methods to immobilize individual worms and to quantify the impact of such methods on the worm locomotion, we recorded on-chip the movement of the worm body. The experimental procedure consists of five steps (**Figure 3.2**): individual worms are initially loaded into the behavior

module for pre-immobilization behavior quantification, then positioned into the immobilization module and finally transferred back into the behavior module for post-immobilization behavior quantification. To control the worm's exact position inside the saw-shape region of the behavior module, we manually adjusted the pressure in the position channel. Worms (young adults) inside the behavior module were slightly compressed in the vertical direction and thus they were not able to escape. Worms were immobilized using air pressure of ~ 172 kPa (25 psi) or CO_2 supply at 69 kPa (10 psi).

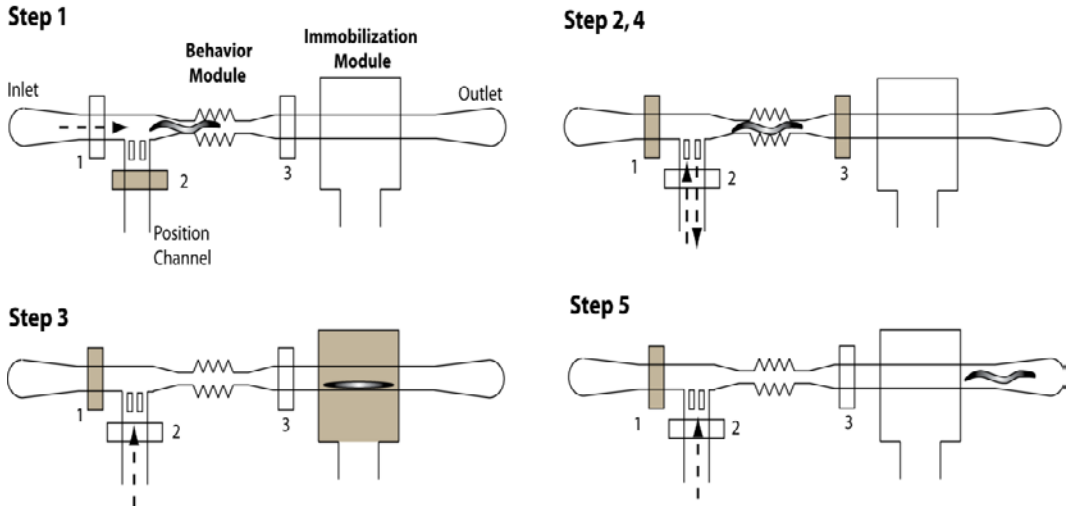

Figure 3.2: Sequence of events (five steps) for the on-chip characterization of the worm locomotion activity: 1) the worm is loaded inside the flow channel (valve 2 is closed), 2) the worm is positioned inside the behavior module by controlling the flow in the position channel (valves 1 and 3 are closed), 3) the worm is pushed into the immobilization module (valve 3 is open). The worm is immobilized by pressurizing the immobilization channel in the control layer with air (25 psi) or by applying CO_2 (10 psi), 4) the worm is released and sent back into the behavior module (valves 1 and 3 are closed), 5) the worm is forced out of the chip by applying positive pressure into the position channel (valve 3 is open). It should be mentioned that all valves are partially closed when activated, allowing flow through them. That 'leaky' operation is typical for valves of rectangular cross-section.

3.3 Results and Discussion

3.3.1 Effectiveness of the proposed immobilization approaches

We tracked the displacement over time of a small region (10 μm x10 μm) of the worm body (**Figure 3.3**) before, during and after immobilization. We avoided the use of fluorescent markers (e.g. GFP) for tracking the worm body motion to eliminate radiation damage that could cause locomotion abnormalities. Worms were active before immobilization and maintained completely immobile at the presence of CO_2 or when pressure was applied (immobilization periods up to 1 hour were performed). During the immobilization period, abrupt displacement peaks of 1.6 μm were observed. We attributed these peaks to movement artifacts generated by the tracking software. None of the methods affected the worm locomotion pattern when short immobilization periods (~1 min) were considered. The CO_2 method proved to be superior after long immobilization periods (>30 min) as the worm showed similar locomotion pattern before and after immobilization.

We also observed that worms were completely immobilized within 1-2 minutes upon CO_2 application. Such a delay (1-2 min) was attributed to the time that is needed for CO_2 to diffuse into the microfluidic chamber and partially remove the air content from the worm's body. To validate that hypothesis, we measured the concentration of CO_2 and O_2 in the immobilization module. The concentration of CO_2 was measured using a pH sensitive dye (thymol blue) while the concentration of O_2 was measured using an oxygen sensitive, fluorescent dye (tris(4,7-diphenyl-1,10-phenanthrolin) RU dichloride complex).

Within 1 min of CO_2 application, the CO_2 and O_2 concentrations reached an equilibrium level of ~76% (**Figure 3.9**) and 6-7% respectively. It should be emphasized that the immobilized channel (in the control layer) is closed at its end, not allowing a fresh CO_2 stream to continuously circulate through the chip. We believe that such a design of the immobilization channel (closed at its end) along with the leakage through the fluidic interconnections of the setup and the open architecture of the chip (the chip is exposed to air) are the major sources for not achieving an oxygen-free environment.

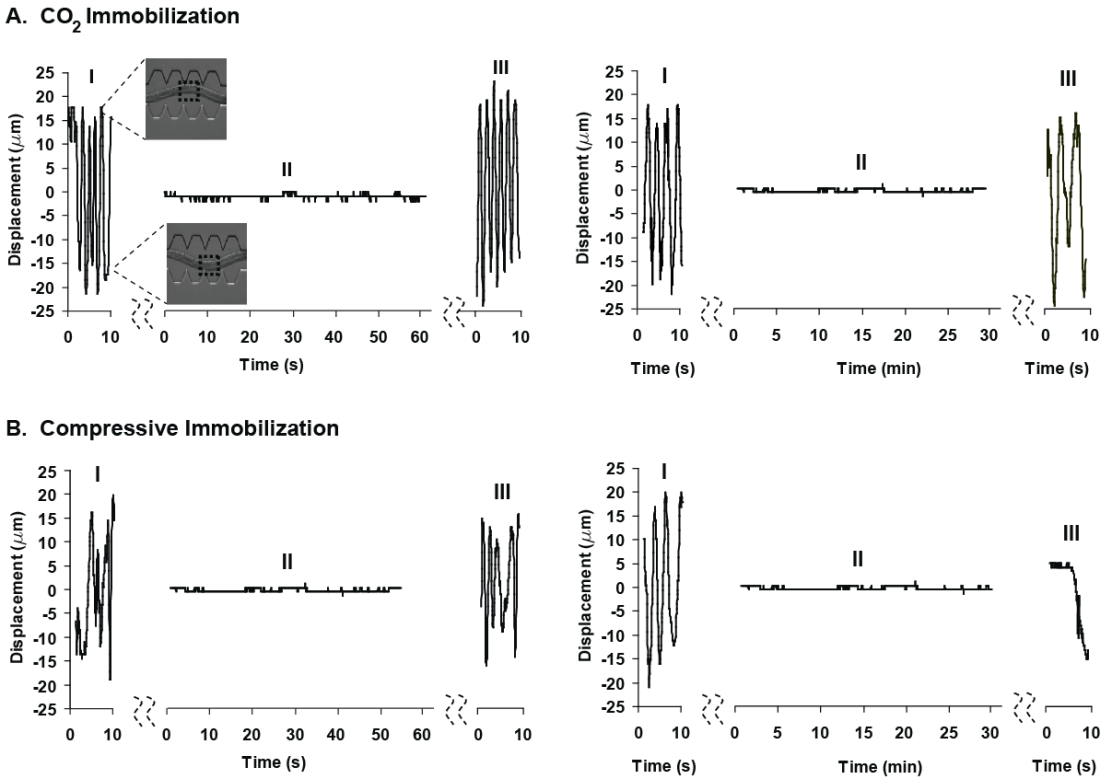

Figure 3.3: Characterization of the worm's locomotion pattern after subjecting it to CO_2 and compressive immobilization for a period of 1 min and 30 min. Graphs indicate the vertical displacement of a 10 µm x 10 µm rectangular area (shown in the upper left figure) in the mid-portion of the worm's body before (I), during (II) and after (III) immobilization.

To identify whether the low-oxygen environment (6-7% O_2) or the presence of CO_2 resulted in the immobilization of the worms, we replace CO_2 with pure N_2. The

presence of N_2 considerably slowed down the worm's movement but it did not immobilize them completely. This is consistent with the fact that worms are still mobile at low-oxygen concentration environments [34]. We thus believe that the presence of CO_2 and the low-oxygen environment act synergistically in altering the functionality of the worm's neuromuscular system.

3.3.2 Anesthetic effects of CO_2

Several studies have reported the use of CO_2 as an anesthetic for invertebrates with an almost immediate recovery upon its removal [66], but the molecular mechanism underlying its anesthetic action is unclear. As CO_2 is known to reduce the pH of an aqueous environment, it has been hypothesized that CO_2 creates an intracellular acidic environment resulting in the deformation of transmembrane proteins and modification of the cell membrane permeability. However, a recent study in *Drosophila melanogaster* does not support that argument [67]. The presence of CO_2 was shown to inhibit the synaptic transmission at the neuromuscular junctions (NMJs) by reducing their sensitivity to glutamate receptors. Other studies hypothesized that CO_2 has an effect on acetylcholine and quantify the effect on dopamine and octopamine neurotransmitters. As these molecular mechanisms have been conserved in *C. elegans*, we anticipate that the CO_2 anesthesia directly affects the NMJ transmission properties.

At the sensory level, CO_2 was recently implicated in affecting neuronal functionality in *C. elegans* through several regulatory molecules [68, 69]. A CO_2 avoidance behavior in well-fed nematodes was found to be mediated by cGMP signaling

through the DAF-11 receptor and the TAX-2/TAX-4 cGMP-gated channel. On the contrary, a reduced CO_2 avoidance behavior in starved worms was found to be regulated by insulin and TGFβ pathways.

3.3.3 Side-effects of the proposed immobilization approaches

A second set of experiments was performed to quantify the off-chip worm behavior after immobilization. Worms were flushed out of the chip to a food-free agar plate after immobilizing them for different time intervals and their average speed was measured (**Figure 3.4**). As no food was present during immobilization, worms were in their dispersal state while on the agar plate. The dispersal state is initiated after prolonged starvation (>5-10 min off food) and it is identified by the significant decrease in the number of short and long reversal as well as omega turns [70]. The corresponding control experiment was performed by loading worms into the chip and flushing them out on an agar plate without immobilizing them.

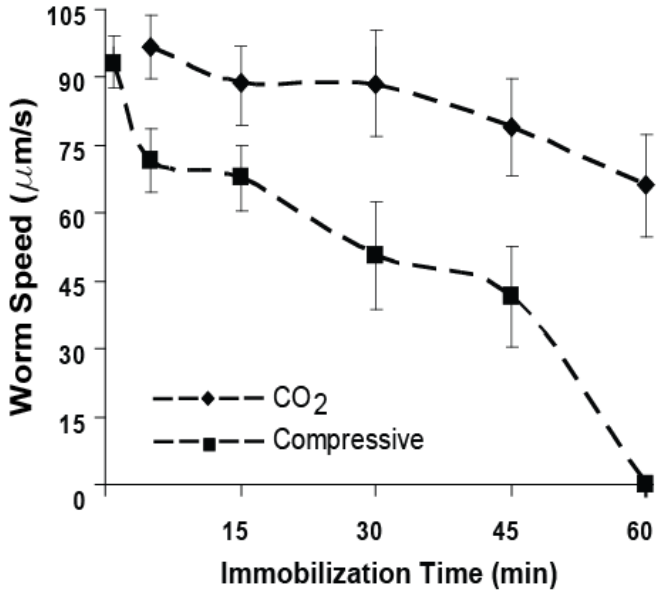

Figure 3.4: Post-immobilization worm locomotion speed on a food-free agar. The horizontal axis represents the duration of the immobilization step. Worms that were

subjected to compressive immobilization for 1 hour did not show any locomotion activity (zero speed). Worms before immobilization (control experiment) had an average speed of 95μm/s (data not shown). Errors bars represent SEM from 8 worms.

We observed that the average speed of the worms on the plate decreased as the immobilization period increased. Immobilization periods of 1 hour resulted zero average speed (immobile worms) and speed reduction of ~70% for the compressive and CO_2 immobilization methods respectively. It should be noted that neither methods resulted in the death of worms for the tested conditions. Worms appeared to slowly recover after left on the agar plate for a few hours. Additionally, we also investigated for the worm's survival to longer periods (up to 4 hrs) of CO_2 immobilization. The preliminary survival test results show a complete recovery of the worms for immobilization periods of up to 2.5 hours. The recovered worms were observed to behave normally on the bacterial lawn.

3.3.4 Applicability of CO_2 immobilization for long-term fluorescence imaging

Furthermore, the absence of oxygen is known to reduce photobleaching of fluorescent markers [71] and therefore the CO_2 immobilization method can be appropriate for long-term fluorescence imaging experiments such as time-lapse imaging of cell development. Photobleaching due to the removal of O_2 was quantified by fluorescent imaging of GPF-expressing motorneurons (**Figure 3.5**). Worms were immobilized using the two proposed methods and the fluorescent intensity of the neuronal cell body was continuously recorded for 4 min. At the low-oxygen environment, a 20% reduction in the fluorescent intensity was observed, significantly smaller than the 55% reduction observed during compressive immobilization.

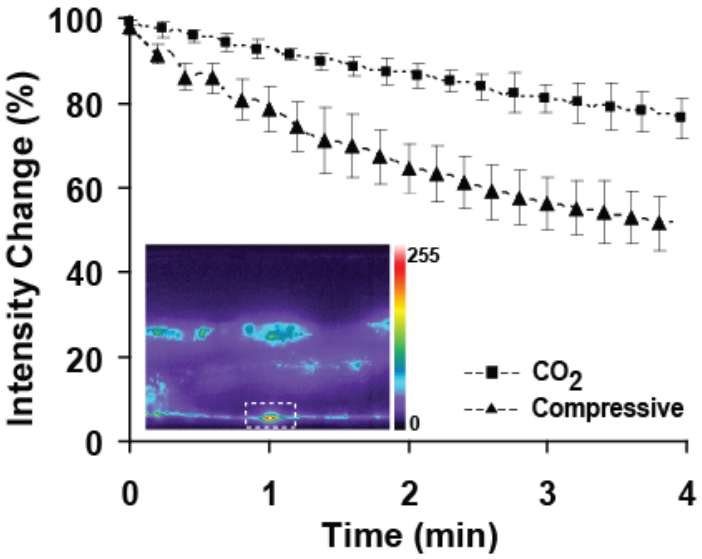

Figure 3.5: Photobleaching curves of GFP-expressing neurons during CO_2 and compressive immobilization. Plot shows the percentage change in the cell body fluorescence intensity with respect to the intensity measured at time t = 0. Error bars represent the standard error of mean from 8 worms. The dashed white rectangle in the picture denotes the position of one of the VA motorneurons where fluorescence was measured.

In order to show the applicability of CO_2 immobilization method for long-term fluorescence imaging, we visualized the movement of bivalent chromosomes in the gonadal cells undergoing meiotic prophase. The bivalent chromosomes undergo restructuring during the late meiotic prophase [72] and the ability to visualize the chromosomal movements during this cell cycle may facilitate the understanding of the chromosomal restructuring process. The chromosomal movements were observed in nematodes expressing GFP in the H2B histone proteins. The gonadal cells undergoing meiotic prophase were imaged continuously for a period of 10 minutes. We tracked the movement of the bivalent chromosome (**Figure 3.6A**) and measured its displacement relative to that of the cell over time (**Figure 3.6B**). It should be noted that there was no

significant photobleaching observed, despite the continuous 10-min fluorescent illumination.

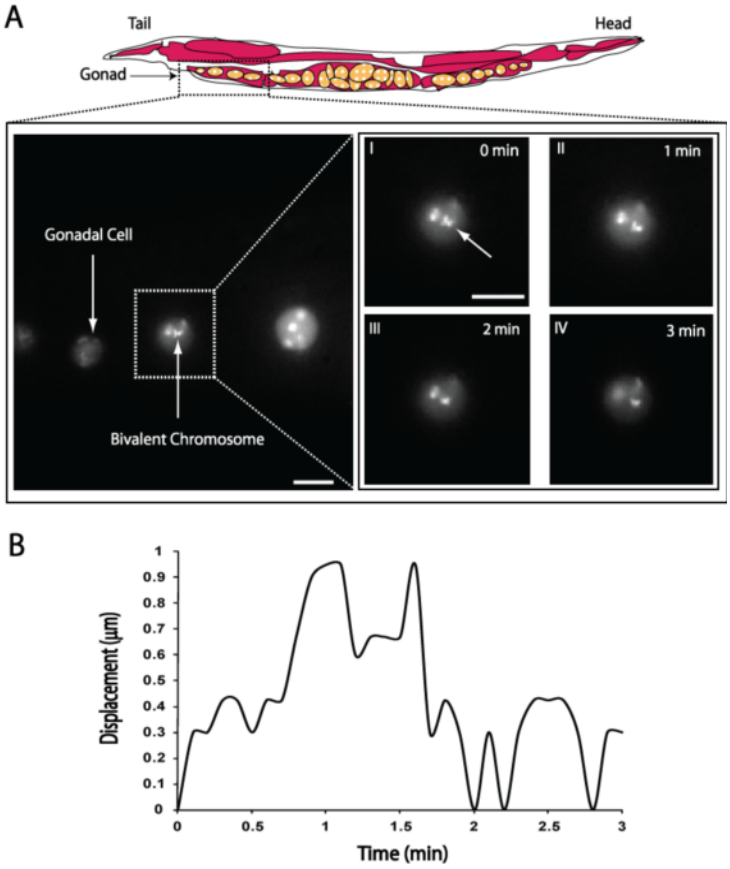

Figure 3.6: (A) Fluorescent images of gonadal cells undergoing meiotic prophase. Pictures I-IV represent the position of a bivalent chromosome at different time instants, **(B)** the graph indicates the total displacement of a single bivalent chromosome from its initial position (at t = 0 min) relative to the displacement of the cell. Imaged were obtained with a 100x oil immersion objective. Scale bar is 2 µm in all images.

3.4 Conclusion

We developed two microfluidic methods for immobilizing *C. elegans* and characterized their impact on the worm's behavior. The first method uses CO_2 to immobilize the worm while the second one mechanically compresses the worm through the use a deformable PDMS membrane. Both methods are easy to implement, allow

worm recovery and can be used to immobilize worms of different ages (**Figure 3.7**). The microfluidic device also incorporates a behavior module that mechanically stimulates the worm and enables the on-chip characterization of its behavior. Our results indicate that the compressive and CO_2 methods are appropriate for short-term (minutes) and long-term (1-2 hours) immobilization respectively.

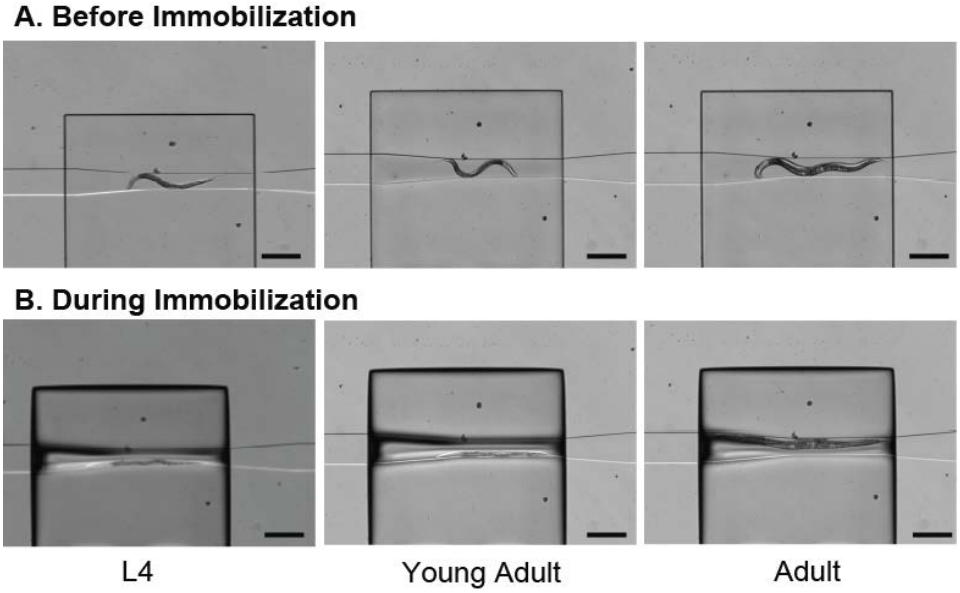

Figure 3.7: Images of worms of different ages (and thus of different sizes) before and during compressive immobilization. Scale bar is 500 µm.

We anticipate that the proposed immobilization approaches can have an impact in a variety of applications, including neuron ablation for studying axon regeneration and neural circuits and time lapse imaging for studying cell development. Both methods can be further applied to accurately identify mutant phenotypes in genetic screening experiments [62] or quantify gene expression over time. The CO_2 method offers the advantage of long-term fluorescent imaging due to the creation of low-oxygen environment that reduces fluorescent photobleaching. Furthermore, the proposed methods

can be automated to immobilize large number of worms in a serial manner [45], thus making them attractive tools for various high-throughput screening applications.

3.5 Experimental Methods

3.5.1 Device fabrication

Soft lithography [64, 65] was used to fabricate the microfluidic devices. The flow and control channels were patterned on two different silicon wafers by spinning SU-8 2025 and SU-8 2050 at thicknesses of 30 µm (2750 rpm) and 70 µm (1750 rpm) (Microchem Corp., Newton, MA, USA), respectively. PDMS was poured onto the two SU-8 masters to create the control (1 cm thick) and flow (70 µm thick, spun at 1100 rpm) layers. The control PDMS layer was peeled off from the SU-8 mold and subsequently aligned and air plasma bonded (50 W, 250 mtorr, 35 s) to the flow PDMS layer. The two-layer PDMS replica was then peeled off from the silicon substrate and punched with using a sharpened, 19-gauge needle (0.031 inch I.D., O.D: 0.042 inch O.D.; Kathetics) to form the fluidic inlets and outlets. Finally, the PDMS slab was bonded to a glass coverslip (#1.5) using air plasma. Access to the flow and control layers was provided by using polyvinyl tubes (0.023 inch I.D., 0.038 inch O.D.; BD Intramedic) connected via a steel pin (0.016 inch I.D., 0.025 inch O.D.) to the various ports of the device.

3.5.2 Transgenic worm strains

The integrated *unc-4::gpf* strain [73] was used to monitor GFP fluorescence from the VA motorneurons. Wild type worms were *C. elegans* Bristol strain N2. All strains

were cultured under standard conditions, fed *E. coli* OP50 and maintained at 20-23°C. Worms homozygous both for integrated transgene */ruIs32/* expressing histone H2B::GFP under control of a germline promoter [74] and */glo-1/ (/zu391/)* mutation lacking autofluorescent and birefringent gut granules [75] were used for live observation of germline chromosomes.

3.5.3 Worm loading and manipulation

Worms were loaded into the chip using the procedure described in [50]. For all of our experiments, we used young adults. Activation of the integrated microfluidic valves for transferring individual worms between the behavior and immobilization modules was achieved with the help of external solenoid valves (LFAA1201610H - Lee Company) (**Figure 3.8**). The valves were controlled using a digital controller (ValveBank II from AutoMate Scientific).

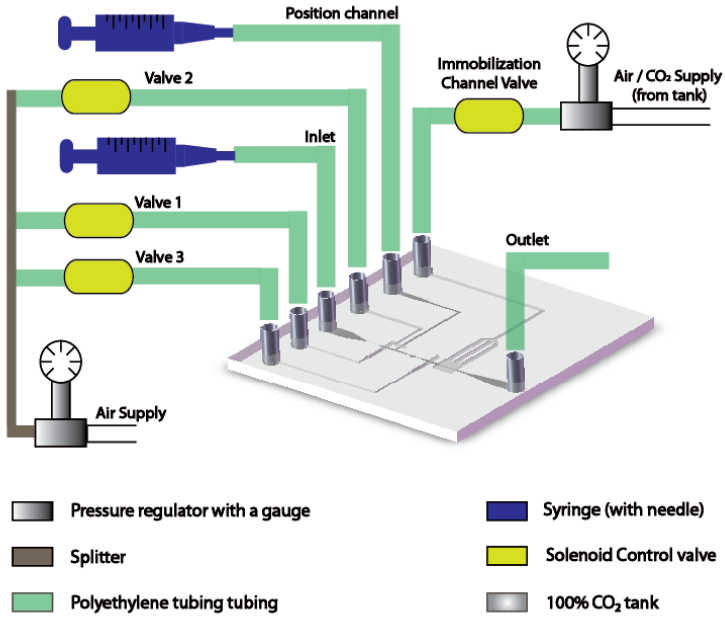

Figure 3.8: Schematic of the experimental setup

3.5.4 Quantification of the on-chip worm locomotion pattern

The displacement measurement experiments (**Figure 3.3**) were done using an inverted microscope (IX71, Olympus) equipped with a 20x objective and a back illuminated CCD camera (QUANTEM:512SC, Photometrics). A black and white real-time streaming video of the worm's movement was obtained and analyzed in Metamorph software. The software tracked the worm body movement and extracted the coordinates of a 10 µm x 10 µm rectangular area superimposed on the mid-section of the worm's body. The optical resolution of the imaging setup was 1.6 µm (each pixel in the image corresponded to 1.6 µm).

3.5.5 Average speed measurement on an agar plate

A video of the worm's motion was recorded for a minute and then uploaded to Matlab. Image thresholding was then performed to render a black and white image, where the white area represented the worm body and the black area represented the background. The video file along with the threshold values was then uploaded to a custom-made Matlab code. The code computed the coordinates of the worm's body centroid in each video frame and used the displacement of the centroid between successive frames to calculate the average speed of the nematode's movement.

3.5.6 Fluorescence imaging

Fluorescence imaging experiments were performed using an inverted microscope (IX71, Olympus) equipped with a 40x oil immersion objective. Before each recording, worms were exposed (10-20 sec) to fluorescent light until the average intensity in the cell

body of the VA motorneurons was decreased to approximately 10,000 fluorescent units. Metamorph software was used to calculate the average fluorescence intensity from the real-time streaming video captured with the back-illuminated camera (QUANTEM:512SC, Photometrics). The exposure time for each frame was 60 ms. The data extracted using Metamorph was then input to a custom-made Matlab code that calculated the percentage change in the average fluorescence intensity over the entire cell body area, relative to the average intensity measured at the start of the recording.

3.5.7 Measurement of the CO_2 concentration

We estimated the concentration of CO_2 during immobilization by measuring CO_2-induced changes in the absorption properties of a pH sensitive dye (thymol blue). A 5 mM solution of the dye was prepared in ethanol and its pH was adjusted to 9.6 by adding 0.1 M of NaOH solution. The dye solution was introduced into the flow channel of the microfluidic device and its absorption intensity change was measured before and after CO_2 application at 69 kPa (in identical conditions to the worm immobilization conditions). The dye was illuminated with yellow light using the transmission mode of an inverted microscope.

To obtain the calibration curve between the CO_2 concentration and the absorption intensity of the dye (**Figure 3.9**), we applied known CO_2 concentrations (0.035% (air), 5%, 20% and 100% CO_2) through a microfludic device that was hermetically sealed. A CO_2-impermeable tubing was used to connect the CO_2 tank supply

to the microfludic device. The calibration data were curve-fitted using a logarithmic relationship.

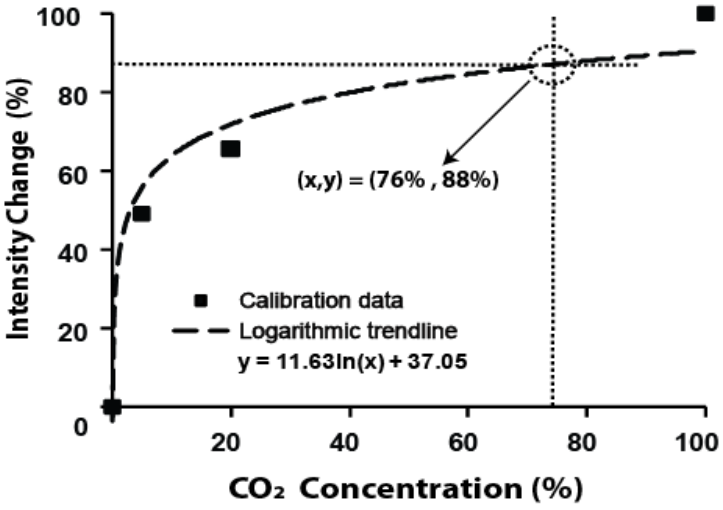

Figure 3.9: Change in intensity of the pH indicator (Thymol Blue) as a function of the CO_2 concentration inside the chip. Solid line represents the measured change in intensities while the dashed line represents a logarithmic curve fit for the measured data. The measured intensity change of ~88% under actual experimental conditions corresponds to a value of ~75% CO_2 concentration (represented by the dashed circle).

CHAPTER 4

A Microfluidic Platform For High-throughput Calcium Imaging Of Chemosensory Neurons In *C. elegans* Using Chemical Stimulation

Functional fluorescence imaging methods are widely used to study cellular physiology. When applied to small organisms, these methods suffer from low-throughput due to the laborious immobilization/stimulus delivery procedure that is typically involved during imaging. This chapter describes the development of an automated microfluidic-based platform for performing high-throughput neuronal functional (calcium) imaging in the roundworm *C. elegans*. The platform immobilizes individual worms, delivers a chemical odor to the their nose and collects calcium imaging data from tens to hundreds of worms per hour without any manual intervention. We used the developed platform to obtain a large number of calcium responses from worms of different ages (212 worms were imaged in total). The calcium imaging data revealed significant difference in the responses from young and old worms, indicating that neural functionality is age-dependent. We believe that such a technology will be an essential tool for obtaining repeatable and accurate functional imaging data from a large population of worms, in order to minimize stochastic biological noise and identify statistically significant trends.

4.1 Introduction

Calcium imaging is a powerful technique for monitoring cellular activity in a variety of model organisms including worms [21], fruit flies [76] and mice [77]. In the roundworm *C. elegans*, calcium imaging has enabled researchers to study the physiology of sensory neurons and muscles [21, 49, 78], to decode activation patterns of neuronal networks at the single cell level [51] as well as to correlate behavior output with neuronal depolarization events [50, 79]. The typical imaging procedure involves the immobilization of a single worm using a glue [60] or a microfluidic biochip [50] and exposing the worm's nose to the desired stimulus. The use of microfluidic biochips [80-82] reduces the number of manipulation tasks associated with the glue technique and provides a controllable, chemical-free microenvironment for performing functional imaging and behavioral experiments. These chip-based approaches rely on manual manipulation tasks, allowing the collection of data from only a small number of worms.

An automated calcium imaging methodology would enable the characterization and statistical analysis of neural functionality from large populations of worms. Such a methodology would not only facilitate the conduction of comparison studies and the elimination of stochastic variations, but it could potentially enable novel, high-throughput (thousands of worms/day), functional-imaging screening assays for discovering unknown molecular pathways and identifying new drugs.

Here, we demonstrate an automated microfluidic-based platform for high-throughput calcium imaging in single worms. The platform is capable of capturing

stimulus-evoked neuronal responses from tens of worms per hour without any manual intervention. We showed that by obtaining a large number of calcium imaging data (we imaged a total of 212 worms), it is possible to reveal the effect of aging on the neuronal functionality of the ASH chemosensory neuron. Understanding the physiology of aged neurons is a particularly challenging task, as aging is considered a stochastic process and thus aging studies require a large number of data in order to obtain statistically significantly trends [53]. Previous studies have unveiled over a hundred aging-related genes [83]. Several of them have been shown to be expressed in sensory neurons [84], suggesting that the functionality of the worm's nervous system might be affected by aging. Our calcium imaging data support the validity of such a hypothesis. The use of the proposed automated platform is not limited to aging research. It is a generic tool for obtaining repeatable and accurate functional imaging data from a large population of worms in studies where neuronal stimulation and monitoring is desired.

4.2 Experimental Design

4.2.1 The automated calcium imaging platform

The automated platform consists of a microfluidic biochip, an epifluorescent microscope equipped with a z-moving stage, a dual-color imager (for FRET imaging) attached to a back-illuminated CCD camera, and a valve manifold connected to the stimulus, buffer and worm-containing solutions (**Figure 4.1a**).

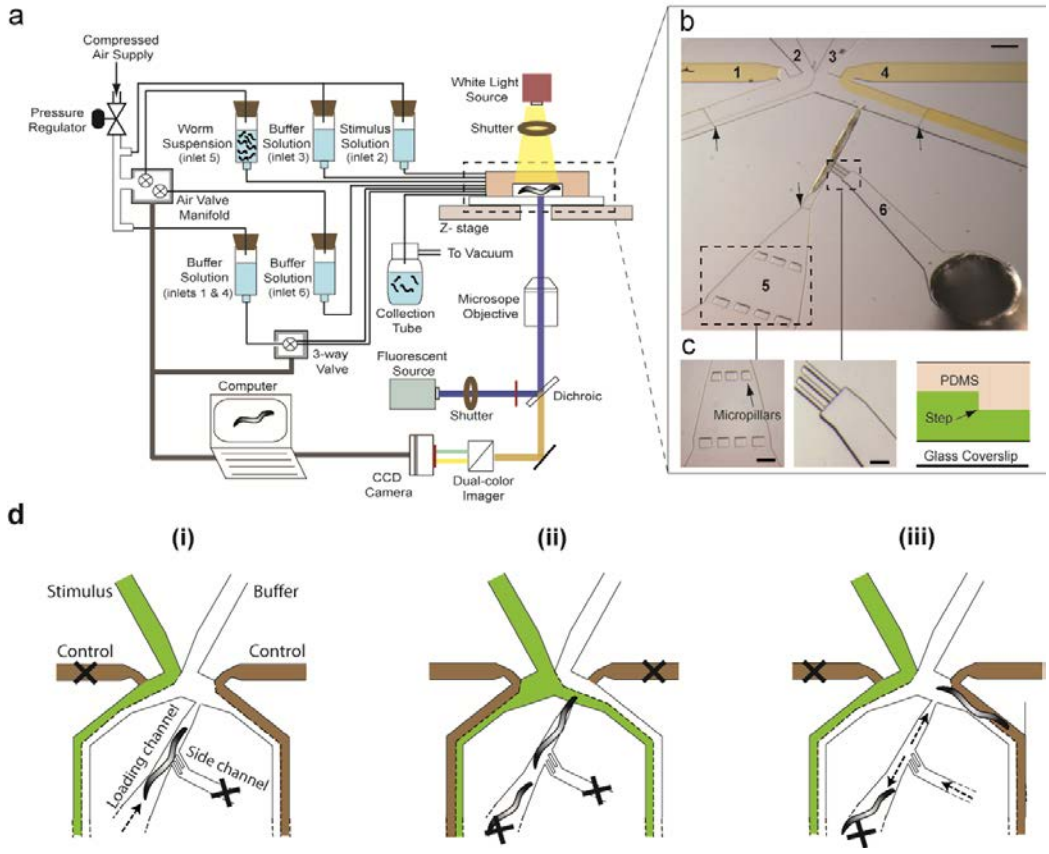

Figure 4.1: The high-throughput functional imaging platform. **(a)** The platform incorporates a microfluidic biochip, a microscope capable of FRET imaging and various fluidic components for worm handling. Scale bar, 300 µm. **(b)** The microfluidic biochip consists of a worm trap and a 4-flow microfluidic network (labeled as 1, 2, 3 and 4) for stimulus delivery. Scale bar, 50 µm. **(c)** The biochip integrates an array of PDMS micropillars (left), labeled as 5 in **b**, a flush-channel to unload the worm (middle), labeled as 6 in **b**, and a step architecture as illustrated in the cross-sectional view (right). These steps are marked with 'arrows' in **b**. Scale bars, 50 µm (left, middle). **(d)** The working principle of the biochip (X denotes a closed microchannel): a single worm is loaded into the trap by pressurizing the inlet (left), the presence of the worm inside the trap is identified and the inlet pressure is released, the ASH cell body is then located, brought into focus and its response to the applied stimulus is recorded (middle), and the worm is unloaded by pressurizing the flush channel (right).

- **Microfluidic biochip design**

The microfluidic biochip is a modified version of the previously developed 'olfactory' biochip [50]. It integrates a 'worm-trap' for immobilizing single worms and a

4-flow microfluidic architecture that precisely delivers the stimulus of interest to the worm's nose (**Figure 4.1b**). An array of micropillars, a 'flush' microchannel and a 'step' architecture, were implemented to the original biochip design to enable automated operation. The array of micropillars was fabricated near the device inlet to help load the worms inside the trap with head-to-tail orientation (**Figure 4.1c**). The pillars act as obstacles in the worm's passage towards the trap. In the presence of constant pressure at the inlet, the worms tend to escape through the micropillar array with their head. We observed that ~70% of the nematodes entered the trap with head-to-tail orientation as compared to less than 5% in the absence of pillars. An additional microfluidic channel - the flush channel – was added on the side of the worm-trap to unload trapped worms from the biochip (**Figure 4.1c**). When a worm is trapped, pressurizing the flush channel generates a bi-directional flow inside the worm trap. The flow directed towards the outlet, forces the worm to exit the trap, while the flow directed towards the inlet prevents other worms from entering the trap. Finally, we adopted a two-thickness ('step') architecture to facilitate easy loading and unloading of worms (**Figure 4.1c**). To achieve that, the thickness of the worm trap and the 4-flow microfluidic channels was designed to match the diameter of the worm's body, while the thickness of the inlet and outlet microchannels was 8-10 μm larger than the diameter of the worm's body, so that worms can easily flow through these microchannels.

- **Operational procedure**

A custom-made graphical LabVIEW interface was used to automate the operation of the platform and the acquisition of calcium imaging data. The operational procedure

consists of five steps: (1) individual worms are loaded inside the worm trap by a constant pressure driven flow applied at the inlet (**Figure 4.1d(i)**), (2) an image-recognition algorithm identifies the worm's orientation and discards worms entering the trap with tail-to-head orientation by activating the flush channel (**Figure 4.1d(ii)**), (3) the neuronal cell body is detected and brought into focus using the z-moving stage (the software discards the worms if it is unable to detect the neuron, e.g., due to low expression level of the fluorescent indicator) (**Figure 4.1d(ii)**), (4) a chemical stimulus is delivered to the worm's nose and the corresponding response is recorded (**Figure 4.1d(ii)**), and (5) the nematode is unloaded by pressurizing the flush channel (**Figure 4.1d(iii)**).

4.3 Results and Discussion

4.3.1 Throughput of the automated calcium imaging platform

To obtain the throughput of the platform, we measured the total time required to process an individual worm, i.e., worm loading, imaging and unloading. Specifically, we used the TN-XL genetically encoded FRET indicator [85] to record glycerol-evoked response from the ASH neuron. To eliminate ASH response to fluorescent light [21], we pre-expose every trapped worm to UV light (power intensity – 3 μW) for a period of 40 s prior to recording (**Figure 4.2**). The process of worm loading, worm recognition, neuron detection and worm unloading took approximately 7 seconds. We observed that ~70% of the worms entered the trap with head-to-tail orientation (we processed 85 worms in a single run and 60 of them came with head-to-tail orientation), which is attributed to the presence of the pillar array. The platform proved to be robust during continuous

operation: in a single run we collected calcium imaging data (response of ASH to a stimulus pulse of 70 s) from 60 worms in 2 h without any manual intervention. It should be emphasized the throughput was limited by the pre-exposure (40 s) and recording time (70 s) which accounted for ~90% of the total worm processing time (2 minutes/worm). Other type of experiments might require shorter recording times and/or no pre-exposure. The throughput therefore depends on the specific study.

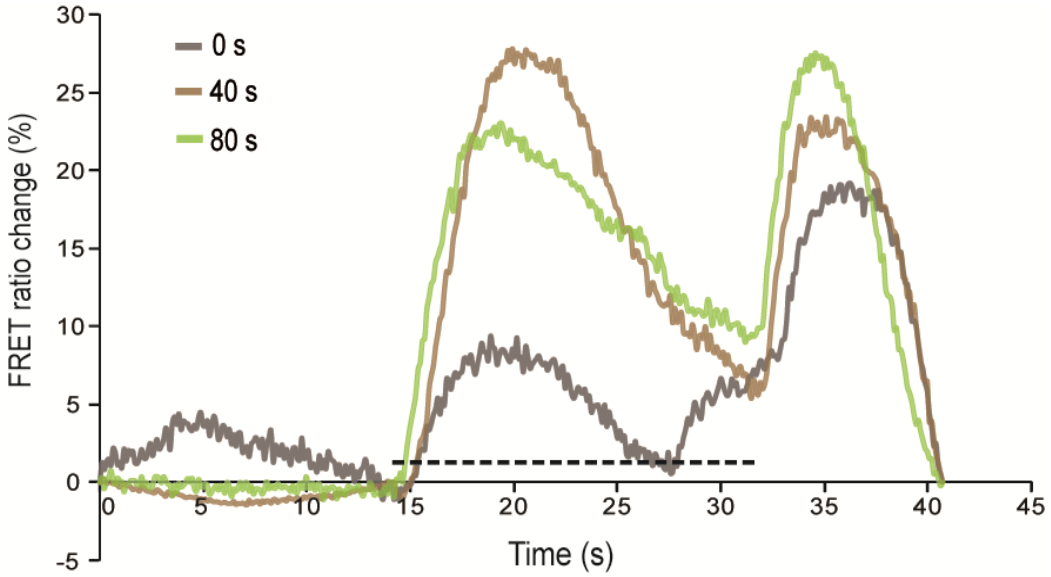

Figure 4.2: Effect of UV pre-exposure to the calcium transients of the ASH neuron from Day 1 worms. A 18 s pulse of glycerol (1 M) was used as a stimulus. Each trace represents percent change in the average FRET ratio from a population of 5 worms. Traces represent the responses obtained after 0 s, 40 s and 80 s UV pre-exposure. We should highlight that, the absence of UV pre-exposure resulted in several irregularities in the ASH calcium transients. An example of this is the upward kink observed in ratio trace (green) at t = 27 s (prior to switching off the stimulus).

4.3.2 Use of the calcium imaging platform for studying the effect of aging on the *C. elegans* neuronal functionality

We utilized the microfluidic platform to characterize and quantify the effect of aging to the excitability of the ASH chemosensory neuron. We monitored the activity of

ASH in response to a 70 s stimulus pulse (1 M glycerol) in an age-synchronous population of worms using the TN-XL indicator (**Figure 4.3a,b**). We imaged a total of 212 worms aged L4 + 1 day (denoted as 'Day 1' worms) to L4 + 5 days (denoted as 'Day 5' worms) at a processing speed of 30 worms/h: 80 recordings were obtained from Day 1 worms, 60 recordings from Day 3 and Day 4 worms, and 12 from Day 5 worms. The low throughput of the platform with respect to Day 5 worms was attributed to the diminished level of TN-XL expression in these worms. The platform processed over 100 Day 5 worms but it was able to collect data only from those that showed bright fluorescence (~10% of the total number of processed worms). To account for the Day 5 worms that showed weak fluorescence, we manually recorded the ASH response using a commercially available image acquisition and analysis software (Metamorph) and compared it to the response recorded by the LabVIEW automation software.

4.3.3 Age dependent ASH neuron response

To quantify the stimulus-evoked calcium transients, we obtained the corresponding FRET ratio changes and identified parameters that were age-dependent. Specifically, we calculated the slope and peak of the rising phase in the ratio traces, at the onset of stimulus (**Figure 4.3c**). We observed that the average slope and peak increased with age for Day 1, 3 and 4 worms, while they declined significantly for Day 5 worms. Studies have shown that stimulus-evoked calcium transients in the ASH neuron are mediated by voltage gated ion channels (TRPV) through the activation of G-protein coupled receptors [86]. Thus, it is most likely that the properties of these transmembrane channels and/or the activity of the related signal transduction pathway are altered with

age, as changes in the function of ion channels have already been correlated with physiological aging [87].

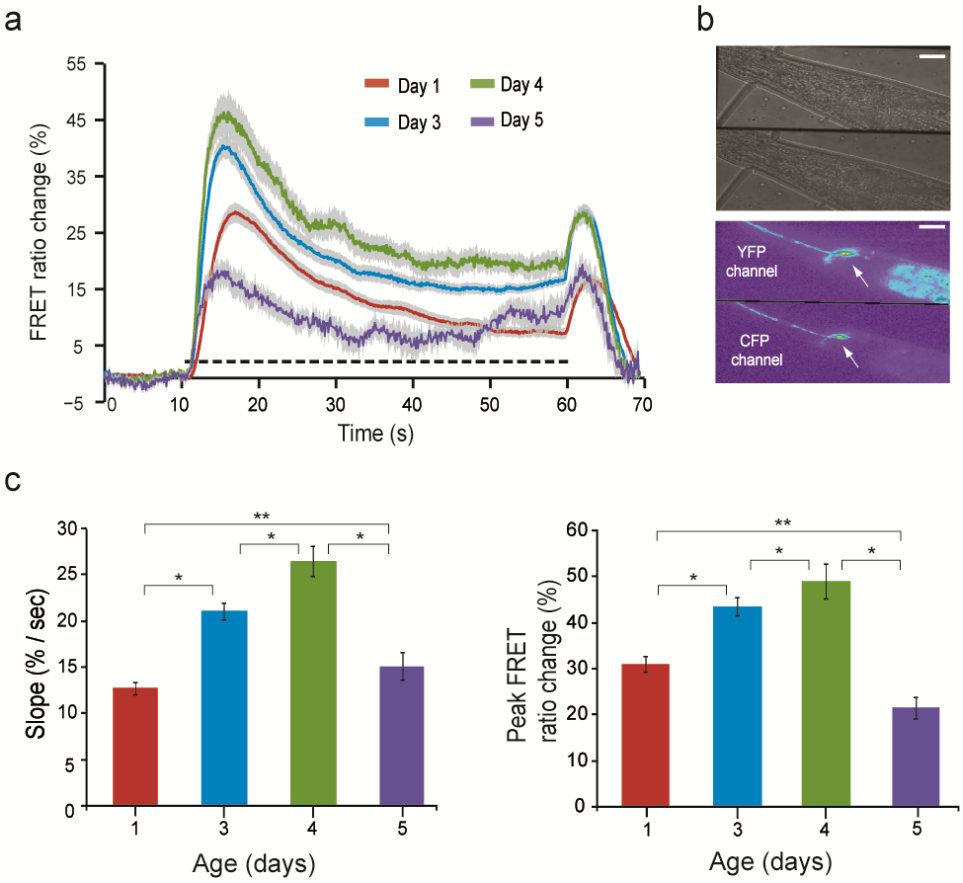

Figure 4.3: ASH ratiometric transients in response to a hyperosmotic stimulus (1 M glycerol) for different ages (L4 worms are taken as Day 0 worms). **(a)** The individual curves represent an average of 80, 60, 60 and 12 recordings from Day 1, Day 3, Day 4 and Day 5 worms respectively. The dashed line represents the presence of the stimulus. **(b)** Bright-field (top) and pseudo color fluorescence (bottom) image of a trapped worm. The ASH neuron is marked with the arrow. In the pseudo color image, the top and bottom half represent the YFP and CFP channels respectively. Scale bars, 5 µm (**a**, **b**). **(c)** The slope (left) and peak (right) of the on-response (extracted from **a**). Error bars indicate standard error of mean. $^{**}P < 0.001$ and $^{*}P < 0.01$ (Student's *t*-test).

We also noticed oscillations in the ratio intensity for Day 1 worms (**Figure 4.4**). The occurrence of these oscillations was observed to decrease with age: ~40% occurence

in younger worms compared to just ~8% in older worms (Day 3). Such oscillations were completely diminished in Day 4 and 5 worms.

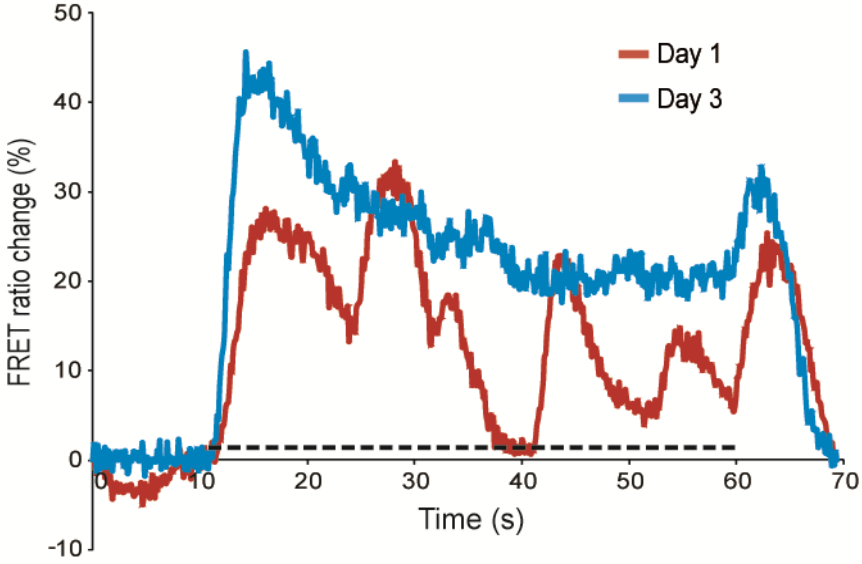

Figure 4.4: Typical oscillatory and non-oscillatory glycerol-evoked calcium transients in the ASH neuron from Day 1 and Day 3 worms respectively. The occurrence of these oscillations decreased with age. We observed 40% occurrence (32 out of 80 worms) in Day 1 worms and 8% occurrence (5 out of 60 worms) in Day 3 worms. Calcium transients in all Day 4 and Day 5 worms had a non-oscillatory pattern (similar to the one shown in this Figure for the Day 3 worm).

To quantitatively describe the calcium oscillations, we performed a Fourier analysis on the ASH calcium transients from Day 1 worms [88]. Specifically, we compared the normalized energy spectral density (see supplementary methods) of the ASH calcium transients that showed oscillations with those that did not (**Figure 4.5a**). The energy spectral density of the oscillatory and non-oscillatory ASH responses differed significantly in the frequency range 0.04 - 0.2 Hz. The oscillatory ASH calcium transients showed a 47% increased band power (see supplementary methods) in this frequency range (0.04 – 0.2 Hz) compared to the non-oscillatory ones (**Figure 4.5b**). This

analysis clearly suggested the presence of oscillations with a period of 5 – 25 sec (0.04 – 0.2 Hz).

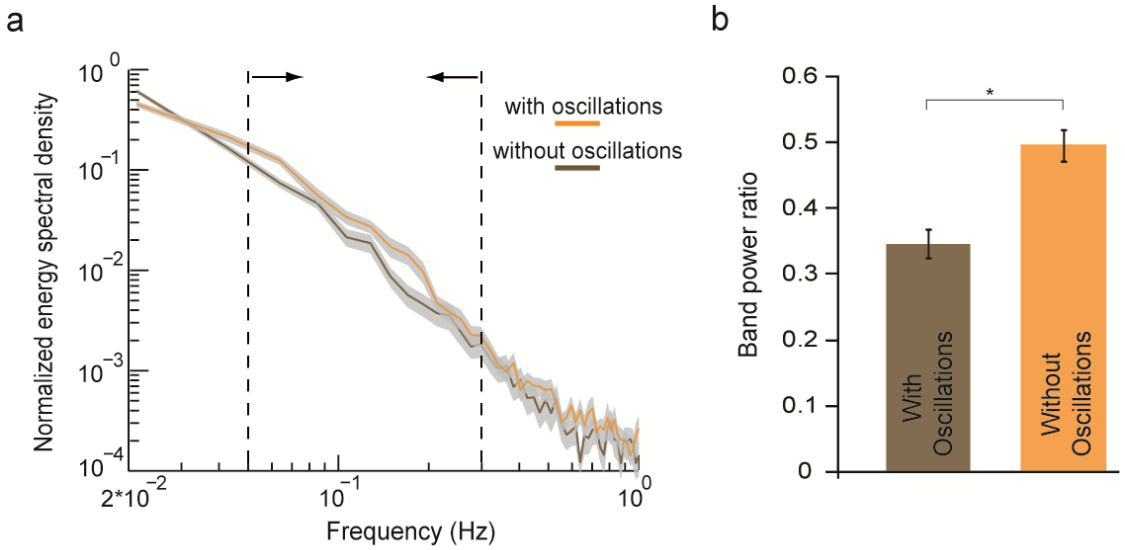

Figure 4.5: Fourier analysis of ASH calcium transients from Day 1 worms. **(a)** Normalized energy spectral density averaged over the Day 1 worm population that showed oscillatory (32 out of 80 worms) and non-oscillatory response (48 out of 80 worms). The arrow indicates the frequency range (0.04 – 0.2 Hz) in which oscillations were prominent. Shaded regions represent the standard error of mean. **(b)** The average band power ratio in the 0.04 – 0.2 Hz frequency range for the two types of ASH calcium transients (with and without oscillations). *$P < 0.01$ (Student's *t*-test).

We should point out that the ratio changes depend on the baseline (prior to stimulation) intracellular calcium level, as the TN-XL sensor does not have a linear response over its entire dynamic range [85]. This suggests that the age dependent changes in the baseline intracellular calcium concentration can possibly affect the slope and peak of the calcium transients. To eliminate such a possibility, we measured the initial calcium concentration for worms of different ages. The difference in the initial calcium concentration between any two ages was found to be within 2-7% (**Figure 4.6**). This difference is not significant to alter the response of TN-XL sensor across the worm ages investigated in this study.

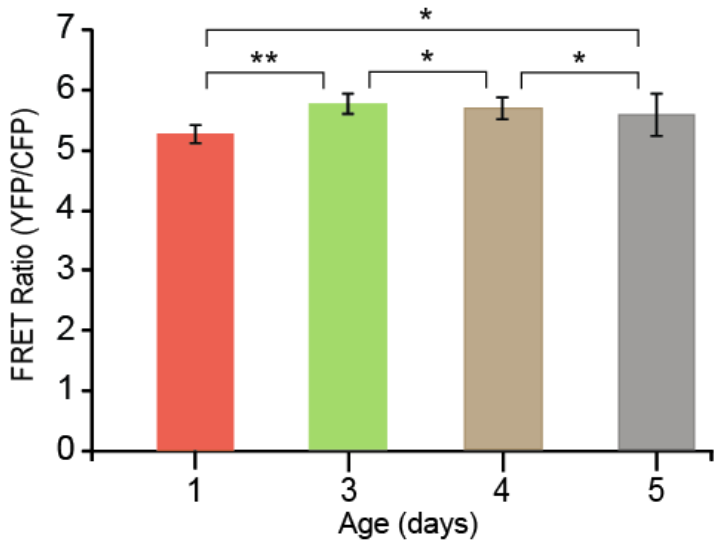

Figure 4.6: Baseline intracellular calcium concentration in the ASH neuron in worms of different ages. These values were obtained by calculating YFP/CFP ratio prior to recording. The difference in the baseline calcium concentrations between any two worm ages was found to be within 2-7%. Error bars indicate standard error of mean (s.e.m). $^{**}P > 0.01$ and $^{*}P > 0.1$ (Student's *t*-test).

4.3.4 Behavioral significance of the age dependent neuronal functionality in *C. elegans.*

Our results indicated that the depolarization amplitude and slope of the on-response increased with age, reached a maximum for gravid adults (Day 4 worms), and eventually declined for the older worms (Day 5 worms). On the behavioral level, the age-dependent variation in the stimulus-elicited ASH responses might account for evolutionary-justifiable functions of the worm's nervous system, with egg laying [89] being one of the most prominent. Since the temporal and spatial positioning of egg laying events are regulated by environmental conditions [90, 91], we speculate that worms during their reproduction peak, have to be accurately guided by sensory cues in order to avoid unfavorable conditions in which eggs have to be retained. We believe that the magnitude and timing of depolarization events, in the presence of an osmotic shock, are

critical for eliciting an immediate withdrawal response that would protect and maintain the egg laying behavior of gravid adults. According to this assumption, the same properties of the ASH stimulus-evoked responses would significantly decline in older animals that had passed their age-dependent egg laying peak. The same reduced excitability of the nervous system is also observed in Day 1 worms (young adults) that carry a limited number of unfertilized eggs.

Our results also indicate a prominent oscillatory response in the neuronal activity of young adults. That response was rather robust as it was observed in 40% of the cases (32 out of 80 worms tested). The oscillations are reminiscent of the oscillatory spikes observed in the olfactory systems of insects and vertebrates that lead to synchronization of the transient's in group of neurons, upon odor stimulation, and have been shown to be necessary for fine odor discrimination [92, 93]. Therefore, we hypothesize that these stimulus-evoked oscillatory events observed in the polymodal ASH neuron also serve in an early age-dependent learning process that includes stimulus detection and recognition. According to our data, the absence of these oscillations in older ages might signify the reduced pattern in cognitive abilities that accompanies aging. We believe that the properties of the optical indicator – TN-XL, made it possible to detect these oscillations, not previously observed using the G-CaMP [50] and cameleon indicators [60]. Compared to G-CaMP and cameleon, TN-XL has a lower affinity to bind to calcium ions [85, 94] and thus a higher sensitivity towards rapid variations in calcium oscillations.

4.4 Conclusion

The developed microfluidic-based platform automates the acquisition of stimulus-evoked calcium responses from single worms *in vivo*. The single layer, step architecture of the microfluidic design allows the easy loading, immobilization and unloading of individual worms, eliminating the need for on-chip microfluidic valves. Such on-chip valves that are typically based on a two-layer PDMS architecture [64] are controlled through external valves and require extra microfabrication steps. The processing speed (throughput) of the platform is limited by the time required for a nematode to enter the micro-trap with the proper (e.g. head-to-tail) orientation and the recording time. Although the recording time is user-specific, (determined by the biological question that needs to be addressed), the worm loading time can be further reduced by adding an 'orientation' module [95] at the expense of increased complexity and cost (e.g. an xyz-scanning stage would be needed to alternate between worm imaging in the 'orientation' module and the 'worm-trap' module). Furthermore, with minor modifications in the image recognition code, the microfluidic platform can be used to obtain recordings from other sensory neurons or interneurons located at the head or tail. The use of a generic interface (LabVIEW) that is compatible with most off-the-shelf hardware devices (eg. CCD camera, shutter controllers, data acquisition boards, etc) makes the platform an easy-to-use tool that can be replicated by other researchers or interfaced with other imaging setups. Lastly, the operation of the platform is not limited to the use of the 4-flow chip: novel microfluidic designs that can deliver other forms of stimuli (e.g. mechanical, thermal, etc.) can be integrated into the platform as the basic processing functions (worm loading, recognition and unloading) remain unchanged.

The automated platform enabled us to obtain calcium imaging recordings from a large number of nematodes (a total of 212 recordings). These recordings revealed the age-dependent physiological properties of the ASH sensory neuron. Interestingly, the depolarization amplitude and slope of the on-response increased with age, reached a maximum for gravid adults and eventually declined for the older worms.

We believe that the proposed microfluidic/imaging platform will find many applications in various neurobiological studies where obtaining large number of functional imaging data is important. Furthermore, we envision the use of this platform in *in vivo* high-throughput, drug screening assays. That can be achieved by incorporating a multi-well plate robotic system where worms are treated with various compounds and subsequently transferred to the platform for screening. The platform can also be used for performing novel functional imaging-based genetic screening assay: by adding a sorting capability to the microfluidic design, one could sort out single mutants from a mutagenized worm population that show a distinct functional neuronal response. Such an assay can have a tremendous impact in identifying novel genes involved in, e.g. neuronal degeneration pathways or in other pathological conditions.

4.5 Experimental Methods

4.5.1 Transgenic strains and sample preparation

For all imaging experiments, we used an integrated line that expressed TN-XL in ASH neuron under the control of the *sra-6* promoter [NKC2311 micIs211(p_{sra-6}::TNXL)].

The line was integrated using a standard UV-exposure protocol [96]. The worms used in each experiment were age-synchronized [97] and grown at 20 ^{0}C on OP50 agar-plates.

4.5.2 Biochip microfabrication

The microfluidic biochip was fabricated using soft lithography. The two-layer SU-8 mold was created using a two-step photolithography process. The thinner microchannels were patterned on the first SU-8 layer that was spun to a thickness equal to the worm's body diameter. The thinner microchannels included the worm trap, the 4-flow channels (stimulus channel, buffer channel and 2 control channels) and the comb-structure that connects the flush-channel to the worm trap. The thicker microchannels were patterned on the second SU-8 layer that was spun to a thickness of 8-10 µm larger than the worm body diameter. The thicker microchannels included the worm inlet microchannel, the flush-microchannel and the outlet microchannels. PDMS was poured onto the SU-8 mold and allowed to cure at 65 ºC for approximately 3 hours. The PDMS layer was peeled off from the SU-8 mold and punched using a sharpened, 19-gauge needle (0.031 inch I.D., 0.042 inch O.D.; Kahnetics) to form the fluidic inlets and outlets. Finally, the PDMS slab was bonded to a glass coverslip (#1.5) using air plasma (50 W, 250 mTorr, 35 s). Access to the flow channels was provided by using polyvinyl tubes (0.023 inch I.D., 0.038 inch O.D.; BD Intramedic) connected via a steel pin (0.016 inch I.D., 0.025 inch O.D.) to various ports of the device.

We fabricated four different SU-8 molds for conducting experiments with Day 1, 3, 4 and 5 worms respectively. The table below **(Table 3.1)** lists the thicknesses of the two SU-8 layers and the type of SU-8 used to pattern them for each SU-8 mold.

Worm Age	SU-8 Layer 1		SU-8 Layer 2	
	Thickness (μm)	***Type***	***Thickness (μm)***	***Type***
Day 1	28	SU-8 2015	36	SU-8 2015
Day 3	32	SU-8 2015	42	SU-8 2015
Day 4	41	SU-8 2015	50	SU-8 2050
Day 5	50	SU-8 2050	60	SU-8 2050

Table 4.1: Thickness of the two layers in the SU-8 molds fabricated for conducting experiments with worms of different ages.

4.5.3 Platform setup

A set of 24 ml syringes containing a suspension of age-synchronized worms, the chemical stimuli (glycerol) and the buffer (S basal) solution is first connected to the biochip via polyethylene tubing. The biochip is then placed onto the stage of an inverted fluorescence microscope (IX71, Olympus) which is equipped with a back-illuminated CCD camera (QUANTEM:512SC, Photometrics), an image splitter for FRET imaging [DV^2 from MAG Biosystems, equipped with a dichroic (505dcxr) and two emission filters (470/30 nm and 535/30 nm)], two optical shutters (one for fluorescence and one for white-light) and a 40x oil immersion objective lens (1.3 NA, UPlanFLN, Olympus). The setup is completed with the use of three 3-way solenoid valves (LFAA1201610H, Lee company), a vacuum generator (Multi-stage high vacuum series, GAST), compressed air supply and a data acquisition board (BNC-2110, National Instruments). All the hardware equipments were controlled through a custom-made LabVIEW code. The code performs the following tasks (**Figure 4.7**): 1) loads a worm into the micro trap, 2) detects the ASH neuronal cell body, brings it in focus and records its response to the delivered

stimulus and 3) unloads the worm. A time sequence of 600 fluorescence images (80 ms exposure time, 1x1 binning) of the ASH neuron was obtained. All fluorescence images are stored for ratiometric data analysis. For all experiments, the compressed air was regulated at ~10 psi and the vacuum pressure was regulated at ~5 psi.

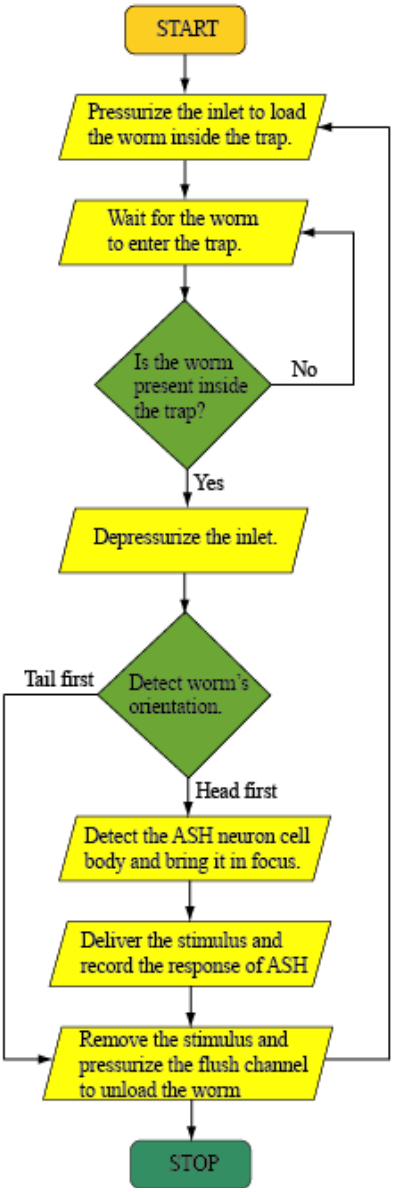

Figure 4.7: Algorithmic representation of the experimental protocol.

4.5.4 Automation software

The LabVIEW code consists of the following three modules:

Worm loading module. This module is used to load single worms into the microtrap. White-light images of the microtrap are continuously analyzed in order to detect the presence of a worm, while the worm suspension solution is pressurized at 10 psi. The worm's presence is determined by comparing the average pixel intensity to a pre-defined threshold value. When a worm is identified the pressure at the inlet microchannel and the worm suspension is released.

Calcium imaging module. This module is used to locate the ASH neuronal body and record its response to the stimulus (1 M glycerol in this study). A coarse stack (5 μm step size) of fluorescence images is initially acquired along the z-axis. Each image in the stack is first segmented using edge detection method. Regions with closed boundaries are then detected in order to locate fluorescent objects in the image. The ASH neuron is identified by comparing the size of the detected fluorescent objects with a pre-defined value. Next, a high-resolution z-stack (1 μm step size) of fluorescence images is acquired below and above the focal plane of the neuron and the images are analyzed to locate the best focal plane. The best focal plane is located by identifying the z-plane that corresponds to the highest average fluorescence intensity of the neuronal body. For that best-focal plane, a time sequence of fluorescence images, that captures the response of ASH to the application and removal of the stimulus, is obtained. These images are stored in the memory for further analysis.

Worm unloading module. That module is used to unload worms from the microtrap by pressurizing the flush-channel. In a similar fashion to the worm loading module, white light images are analyzed in real-time to determine the removal of the worm from the microtrap. The removal of the worm is confirmed by comparing the average pixel intensity to a pre-defined threshold value. This is then followed by the release of pressure in the flush-channel.

4.5.5 Image and Data analysis

We wrote a LabVIEW program to extract the mean FRET ratio from each fluorescent image. Each fluorescent image was split into two images, each one representing the YFP and CFP channels. Our program required four pieces of information that were specified by the user: 1) the region of interest defining the boundary of the neuron in YFP channel, 2) the region of interest in the YFP channel within which the neuron moves, 3) the region of interest defining the background fluorescence of the worm in the YFP channel and 4) the initial coordinates of the neuron in each channel (YFP & CFP). Our program first calculates the difference between the initial coordinates of the neuron's centre in each channel. It uses this difference to correct for any misalignment between the YFP and CFP images. It then tracks the neuron in each channel and extracts the corresponding background subtracted mean fluorescence intensity. The FRET ratio is calculated as the ratio of mean fluorescence intensity of the neuron in the two channels.

We corrected the FRET ratio traces for photobleaching by removing the exponential trends before and after stimulation [21]. To do this, the trends before and

after stimulation were curve fitted with exponential trendlines. We subtracted the curve fitted trendlines from the corresponding ratio traces and obtained new ratio traces that were compensated for photobleaching. We performed all the computations on the new ratio traces. For each trace, we calculated the percent change of the ratio relative to the average ratio during the first 5 s. We then calculated the slope, peak and duration of the rising phase at the onset of the stimulus.

4.5.6 Fourier analysis

We analyzed the spectral content of the ASH calcium transients using a discrete fourier transform. To distinctly quantify the calcium oscillations from the spectral content of the ASH response, we first removed the contribution of the secondary peak corresponding to the off-response of ASH from the raw data. We then computed the fourier transform of the clipped ASH response curves (defined as y(t)) using the FFT subroutine in MATLAB, at 512 equally spaced frequencies from f_0 = 0 Hz to f_{512} = 4 Hz. The fourier transformed data was then used to calculate the 'normalized energy spectral density' using the following equation:

$$\frac{|Y(f_k)|^2}{\sum_{f_1 \le f_k \le f_{N/2}} |Y(f_k)|^2} \qquad \textbf{Eq}^{\textbf{n}}\ \textbf{4.1}$$

where, $Y(f_k)$ = discrete fourier transform of y(t)

N = 512

f_1 = 0.008 Hz

$f_{N/2}$ = 2 Hz

We divided the energy spectral density curve (Fig. 4) into three different frequency bands – low, mid and high [25]. The lower frequencies (< 0.04 Hz) captured the primary ASH

response, mid frequencies (0.04 – 1 Hz) captured the calcium oscillations and higher frequencies (> 1 Hz) captured the noise content in the data. To quantify the contribution of calcium oscillations to the ASH response curves, we calculated the energy spectral density contained within the frequency range of 0.04 – 0.2 Hz defined as the 'Band Power Ratio' as shown in the following equation:

$$\frac{\sum_{f_{min} \leq f_k \leq f_{max}} |Y(f_k)|^2}{\sum_{f_1 \leq f_k \leq O_{N/2}} |Y(f_k)|^2} \qquad \textbf{Eq}^{\textbf{n}}\ \textbf{4.2}$$

where, f_{min} = 0.04 Hz

f_{max} = 0.2 Hz

The normalized energy spectral density and the band power ratio were then averaged across the two types of ASH calcium transients (with and without oscillations) from Day 1 worms (**Figure 4.5**).

4.5.7 Manual recording from Day 5 worms

The automated system discarded a significant population of Day 5 worms (~90%) as their ASH neuron displayed very weak fluorescence. Thus, to validate the results acquired for Day 5 worms, we manually recorded the ASH response from these worms using Metamorph software – a commercially available image acquisition/analysis softwarethe Metamorph software. Metamorph allowed us to access the 'enhanced gain' feature of the CCD camera and thus enabled the recording of ASH response from Day 5 worms that showed weak fluorescence. The enhanced gain feature allowed us to record from all Day 5 worms that were loaded in the device. We recorded the ASH response

from 15 Day 5 worms (**Figure 4.8a**). The average values of the peak and slope (**Figure 4.8b**) of the rising phase in the ratio trace at the onset of the stimulus were similar to that obtained using the microfluidic platform.

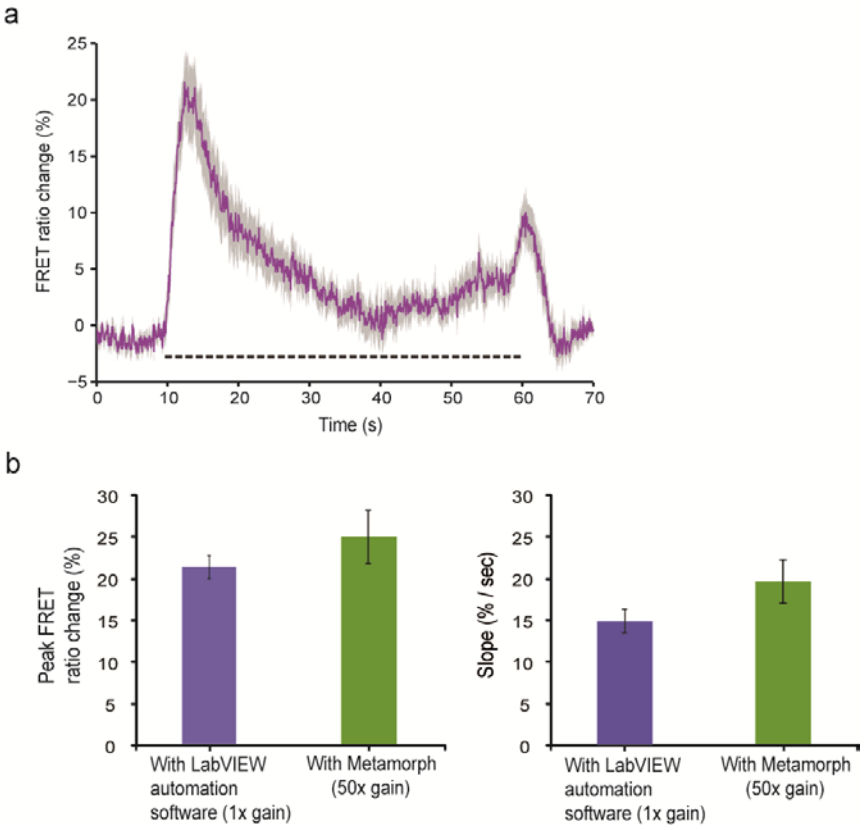

Figure 4.8: ASH ratiometric transient from Day 5 worms in response to a hyperosmotic stimulus, recorded using Metamorph with an enhanced gain of 50x. **(a)** The curve represents an average of the ASH response from 15 Day 5 worms. The dashed line represents the presence of the stimulus. Shaded region represents standard error of mean. **(b)** The peak (left) and slope (right) of the on-response recorded using the microfluidic platform and Metamorph.

CHAPTER 5

Probing The Physiology Of ASH Neuron In *C. elegans* Using Electric Current Stimulation.

Electrical stimulation has been widely used to modulate and study the *in vitro* and *in vivo* functionality of the nervous system. We utilized the calcium imaging microfluidic platform presented in chapter 4 and characterized the effect of electrical stimulation on the ASH neuron in *C. elegans*. We characterized the ASH neuronal activity in response to electric currents of varying strength and electrical polarity in age-synchronous populations of worms. The electrically induced ASH neuronal response was observed to be dependent on the magnitude, polarity and spatial location of the electrical stimulus as well as on the age of the worm.

5.1 Introduction

Electrical stimulation is known to trigger neuronal responses by directly affecting the neuronal membrane potential [98, 99]. This has made electrical field stimulation of neurons an exceptional technique for modulating and studying the functionality of the nervous system. Invasive as well as non-invasive electrical stimulation approaches have been utilized to create a functional map of the brain [100, 101] and modulate sensory perception in monkeys [102, 103]. Electrical stimulation has been used in cases of pathological conditions such as anxiety, depression, insomnia and motoneuron deficiencies. Furthermore, neuronal cells can respond to electric stimulation in the form

of directional migration and growth, a phenomenon termed electrotaxis that has been extensively used in nerve regeneration studies [105].

Electrical stimulation has also been shown to induce locomotory behavioral responses at the whole organism level [106]. This electrotactic behavior has been extensively investigated in the nematode *C. elegans*, a widely used model organism in the neuroscience field. *C. elegans* navigates towards the negative terminal in the presence of a DC electric field [32, 33, 43] while an AC electric field is known to constrain its navigation pattern [44]. It is speculated that this behavior is mediated by a network of amphid sensory neurons [33] and it has been used to robustly transport and sort *C. elegans* inside controlled microfluidic environments [43, 44] as well as on electrophoretic gels [107].

Here, we demonstrate that electric stimulation can be used to probe the physiology of the ASH neuron, a polymodal sensory neuron in *C.elegans* that has been implicated in electrotaxis as well [33].

5.2 Experimental Design

5.2.1 Microfluidic platform for Electrical stimulation and Calcium imaging

To acquire calcium imaging data in response to electrical stimulation, we fabricated a microfluidic chip (**Figure 5.1a**), the ‘e-chip’ (‘e’ stands for electric), that

enabled us to electrically stimulate the worm and interfaced it with a modified version of the microfluidic platform (**Figure 5.1b**) presented in chapter 4 ([108]).

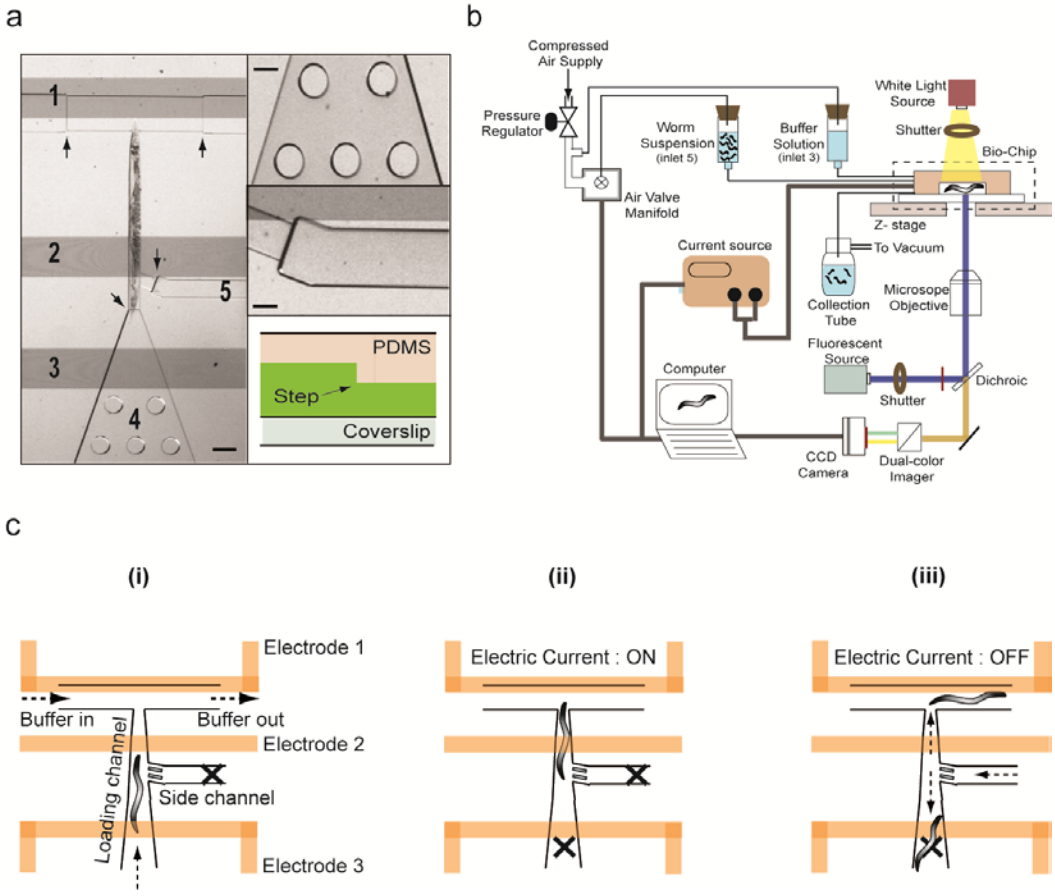

Figure 5.1: (a) The e-chip for electrically stimulating single worms. It consists of a worm trap, a set of ITO electrodes (labeled as 1, 2 and 3), an array of PDMS micropillars (labeled as 4) and a flush channel (labeled as 5). Scale bar, 150 µm. Magnified views and the step architecture of the e-chip are shown on the right. Scale bars, 100µm. **(b)** The automated platform for electrical stimulation and functional (calcium) imaging. **(c)** The working principle of the biochip (X denotes a closed microchannel). (i) Worm loading. (ii) Electrical stimulation and optical recording of ASH calcium transients. (iii) Worm unloading.

The 'e-chip' (**Figure 5.1a**), integrates a worm trap for immobilizing and imaging single worms and a set of transparent (indium tin oxide (ITO)) electrodes for applying a current to the worm's body at different locations. An array of micropillars at the inlet, a

‘flush’ microchannel and a ‘step’ architecture were also implemented, to facilitate automated operation as described in chapter 4 ([108]).

5.2.2 Operational procedure

The operational procedure consisted of three steps : (1) individual worms were loaded inside the worm trap by a constant pressure driven flow (a pressure of 10 psi was applied at the inlet of the e-chip) (**Figure 5.1c(i)**), (2) the fluorescently labeled ASH neuron was brought into focus using a piezoelectric stage, an electric current of a particular magnitude and polarity was applied to the worm’s body and the corresponding ASH response was recorded (**Figure 5.1c(ii)**) and, (3) the nematode was unloaded by pressurizing the flush channel (**Figure 5.1c(iii)**).

We recorded intracellular calcium transients in the ASH neuron using the genetically encoded FRET indicator TN-XL [85], while a 10s pulse of electric current was applied to the worm’s body with head-to-tail orientation (we term this as the positive polarity electric current).

5.3 Results and Discussion

5.3.1 Quantification of the electrically-evoked ASH response

A typical ASH calcium transient in response to an electric current is shown in **Figure 5.2a**.

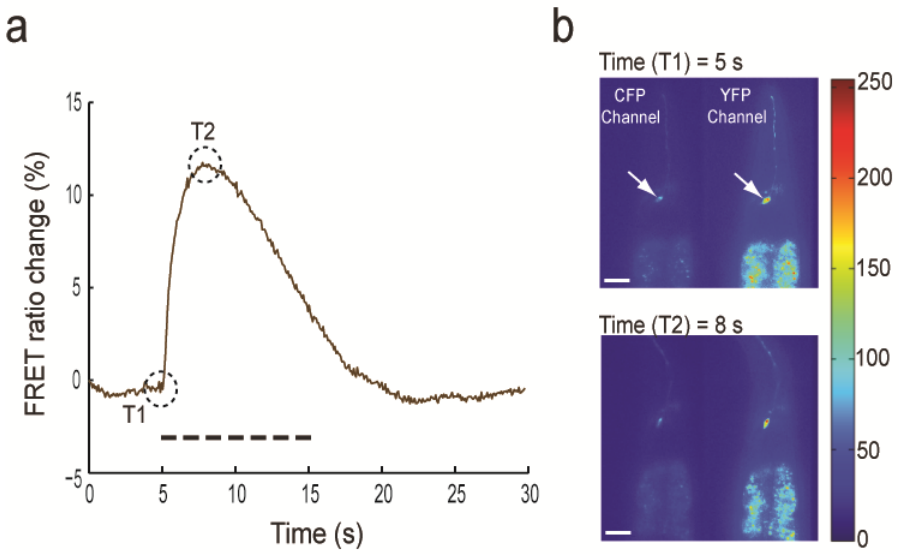

Figure 5.2: (a) Representative calcium transient from the ASH neuron in response to electric current stimulation. The dashed line represents the duration (10s) of the stimulus. The peak, steepness of the rising phase (α) and decay rate (β) were identified as the characteristic parameters of the transient. **(b)** Pseudocolor images of the worm depicting the fluorescence intensity of the ASH neuron (marked by the arrow in the two FRET channels) at two time points – T1 and T2 – marked in (a). Scale bar is 100µm.

To quantify the stimulus-evoked calcium (Ca^{2+}) transients, we established characteristic metrics that are representative of the electrically-evoked ASH response and are physiologically relevant. Particularly, we extracted the peak, steepness of the rising phase and the decay rate from the calcium transients at the presence of the stimulus (**Figure 5.2a**). These parameters are indicative of the maximum calcium concentration (peak), the rate of calcium influx (steepness of the rising phase) and the rate of calcium efflux (decay rate) in the ASH neuron. We utilized a curve fitting modeling approach to derive a quantitative estimate of these parameters [109]. We first modeled the ratio transients with a first-order differential equation (**Eq^{n} 5.1**) that relates the rate of change of intracellular calcium concentration (dCa(t)/dt) to the rate of calcium influx and efflux (indicated by parameters α and β respectively):

$$\frac{d\,Ca(t)}{dt} = \phi * I * e^{-I.\tau.t} - \beta * Ca(t) \qquad \textbf{Eq}^{\textbf{n}}\ \textbf{5.1}$$

The above equation states that, upon neuronal activation : (a) calcium enters the cell at a rate equal to 'α = ϕ*I' (calcium influx), which then decays exponentially with a time constant 'I*τ' and (b) the neuron depletes itself of calcium at a rate proportional to the extra calcium present inside the cell due to depolarization, with a proportionality constant, 'β' (Ca^{2+} efflux). We should highlight that, 'I' models the dependency between the rate of calcium influx and the duration of the calcium transient, stating that, shorter calcium transients are accompanied with higher rate of calcium influx. We curve fitted this differential equation to the experimentally obtained FRET ratio transients and extracted the values of the coefficients, 'α' and 'β'.

5.3.2 Age dependent ASH neuron response

To study the effect of aging on ASH functionality, we monitored electric current-evoked calcium transients in worms of 3 different ages (**Figure 5.3a**): L4+1 day, L4+ 3 days and L4+5 days (denoted as 'Day 1', 'Day 3' and 'Day 5' worms respectively) in response to an electric current of 0.01μA. All three parameters, the maximum calcium concentration, the rate of calcium influx ('α') and efflux ('β') were observed to increase with age (**Figure 5.3b**). These trends can be attributed to several mechanisms such as:

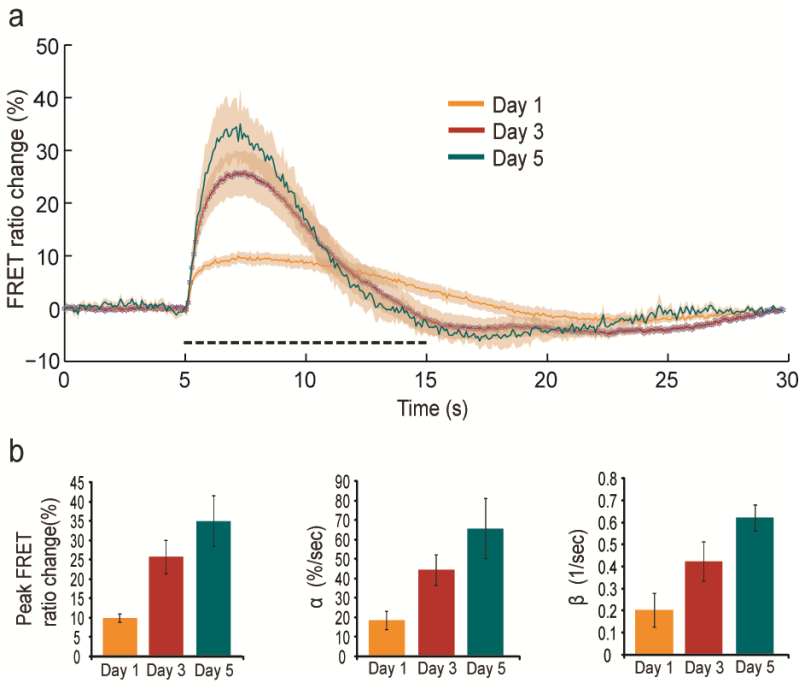

Figure 5.3: Age-dependent effects of electric current of positive polarity in ASH. **(a)** Individual curves represent an average of 15 recordings from Day 1, Day 3 and Day 5 worms. Shaded regions represents standard error of mean. The dashed line represents the presence of the stimulus. **(b)** Mean values of the peak, α and β constants of the calcium transients for three different ages. Error bars represent standard error of mean.

---

1) Age dependent decrease in Calcium Buffering mechanisms

Studies have reported an increase in neuronal calcium level in aged rat's adrenergic neurons due to an impairment of intracellular calcium regulatory/buffering mechanisms [110]. Ca^{2+} buffers regulate calcium transients and modulate the amplitude and duration of Ca^{2+} influx, by mechanisms that involve Ca^{2+} binding proteins and calcium sequestering organelles such as the mitochondria and the endoplasmic reticulum (**Figure 5.4a**). Strong calcium buffering slows the rate of intracellular calcium clearance from the cytoplasm, which is depicted by an increase in the duration of the intracellular calcium transients and a sustained Ca^{+2} influx (**Figure 5.4b**). On the other hand, weak calcium buffering results in an increased calcium influx and in a limited duration of the

calcium rise (**Figure 5.4b**), which is observed in the calcium transients from aged worms. Thus, it is possible that the age-dependent characteristics of the ASH calcium transients might be associated with the age-dependent decline in the calcium buffering mechanisms.

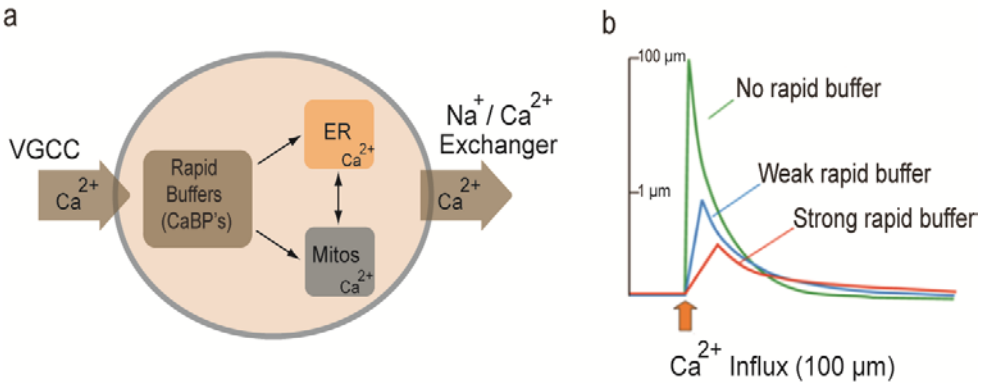

Figure 5.4: (a) Schematic representation of the major components involved in Ca^{2+} signaling and buffering in central neurons. Ca^{2+} enters the cytoplasm via the voltage-gated Ca^{2+} channels (VGCCs) upon cell depolarization. Rapid buffers such as calcium binding proteins (CaBP) along with organelles such as the endoplasmic reticulum (ER) and mitochondria consume Ca2+ and reduce the peak Ca^{2+} influx. Depending on the amount of Ca^{2+} influx exchange of Ca^{2+} might also take place between the organelles. Ca^{2+} is cleared from the cytoplasm also by extrusion through the cell membrane by the Na^{+} - Ca^{2+} exchanger. **(b)** Idealized intracellular calcium transients expected for different degrees of intracellular calcium buffering capability. Increasing strengths of calcium buffering capability results in a lower value of peak calcium influx and slower decay kinetics. Also note that, there is a delay in the peak Ca^{2+} level with increasing buffering strength. [Adapted from [111]].

---

2) Age dependent increase in the density of Voltage Gated Calcium Channels

It is also possible that electric current-evoked neuronal calcium transients are triggered directly by the activation of voltage gated calcium channels (VGCC's) (**Figure 5.4a**) such as the L-type calcium channels in the ASH neuron [16]. Studies have revealed an increase in the L-type Ca^{2+} channels and a subsequent increase in the voltage gated Ca^{2+} currents in aged rat hippocampal CA1 neurons [112]. Therefore, the observed age-

dependent calcium influx might also be due to an age-associated increase in the density of VGCC's in the ASH neuron, similar to the increase in hippocampal CA1 neurons.

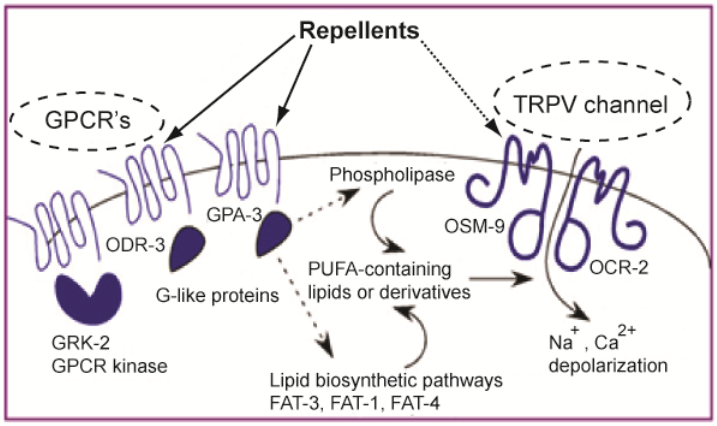

Figure 5.5: A probable signal transduction pathway for sensing noxious stimuli, in ASH neuron processes [adapted from [86]]. This pathway includes the involvement of Gi-like proteins, biosynthetic enzymes, TRPV channels and G protein coupled receptors (GPCRs). The noxious stimuli might be first detected by GPCRs, which then regulates the production or consumption of phospholipids containing PUFAs (omega-3 and omega-6 polyunsaturated fatty acids) via the activation of Gi-like proteins ODR-3 and GPA-3. The lipid mobilization then opens the TRPV ion channels, and consequently depolarizes the cell. There also exists a possibility that the TRPV ion channels get directly activated by the noxious stimuli (mechanical, chemical or osmotic stimuli).

We should point out that, the age-dependent ASH functionality has been previously studied using glycerol as a chemical stimulus (Chapter 4). In contrast to the electric current evoked responses, glycerol evoked ASH responses indicated an increased peak and rate of calcium influx in younger ages (up to Day 3), followed by a decrease in older ages (Day 5). While, glycerol-evoked ASH calcium transients also involve the participation of VGCC's, those channels are triggered by upstream signaling pathways involving the olfactory G-protein coupled receptors (GPCR's) [86] (**Figure 5.5**). GPCR's can recognize a specific chemical stimulus or an osmotic shock (e.g. glycerol), but might not be activated at the presence of an electrical stimulus. Thus, we speculate that the

observed age-dependent glycerol evoked ASH neuronal responses are due to age-associated changes in the glycerol induced signaling cascade that acts upstream of the VGCC's.

5.3.3 Dependence of ASH response on Electric Current Magnitude

We analyzed ASH responses of a particular age (Day 3 worms), as a function of the magnitude of the applied current (**Figure 5.6a**). These responses were positively correlated with electric current of up to 0.01µA. Magnitudes greater than 0.01µA, caused saturation in the peak neuronal responses (**Figure 5.6b**). Electric current of 0.01µA generated a potential difference of approximately 1.2V across the worm's body (which corresponds to an electric field strength of 10V/cm). As electric field intensities of approximately 14V/cm have been reported to induce paralysis to the worm [33], we believe that the observed saturation in neuron responses might be correlated with such damaging effects.

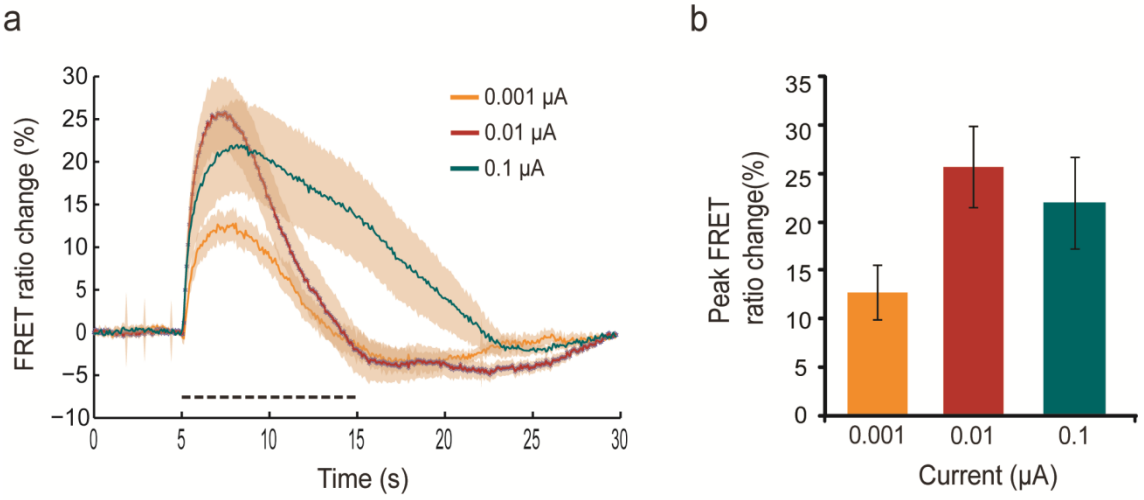

Figure 5.6: Effect of magnitude of the applied electric current (positive polarity) in ASH in Day 3 worms. **(a)** Individual curves represent an average of 15 recordings in response to electric current of magnitudes 0.001µA, 0.01µA and 0.1µA. Shaded regions represents standard error of mean. The dashed line represents the presence of the stimulus. **(b)** Mean

value of the peak of the calcium transients for three different current magnitudes. Error bars represent standard error of mean.

5.3.4 Dependence of ASH response on Electric Current Polarity

The electrotactic behavior of *C.elegans* has been reported to be sensitive to the polarity of the applied electric field [33, 43]. To investigate the effect of electrical polarity, we applied an electric current to the worm's body with a tail-to-head orientation (negative polarity electric current). We obtained ASH calcium transients from Day 1 worms, in response to three different electric current magnitudes (**Figure 5.7**). A preferential bias with respect to the polarity of electric current was observed. Increasing the magnitude, reduced neuronal depolarization while magnitudes higher than 0.01µA hyperpolarized ASH. This trend was also observed for Day 3 and Day 5 worms.

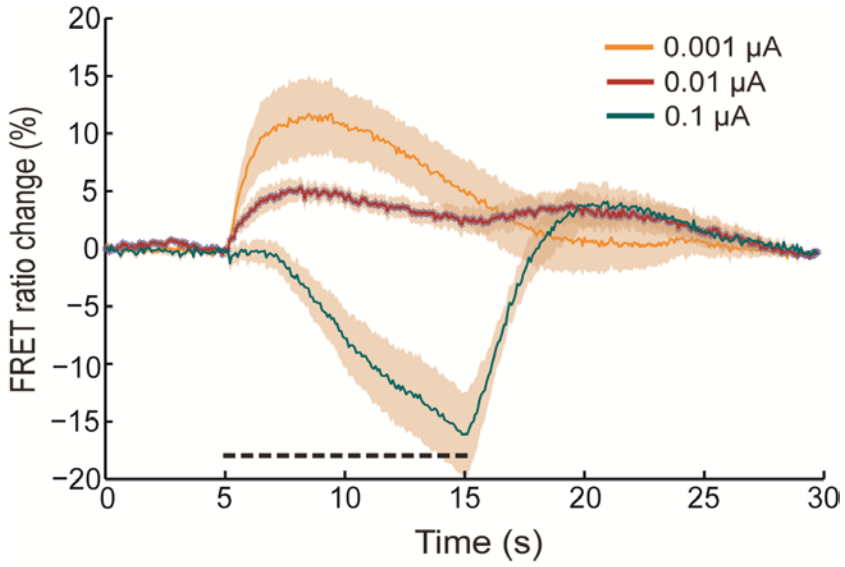

Figure 5.7: Effect of electric current of negative polarity in ASH in Day 1 worms. Individual curves represent an average of 15 recordings corresponding to electric current magnitudes of 0.001µA, 0.01µA and 0.1µA, respectively. ASH is hyperpolarized when stimulated with a current of 0.1µA. Shaded regions represent standard error of mean.

5.3.5 Dependence of ASH response on Spatial Location of Electric Current

We also obtained ASH calcium transients from Day 1 worms, in response to electric current applied between the head and the mid-body (electrodes 1 and 2 in **Figure 5.1a**) as well as between the tail and the mid-body (electrodes 2 and 3 in **Figure 5.1a**) of the worm. The above mentioned polarity dependent ASH response was only observed in the former case. No ASH response was observed in the latter case.

5.4 Conclusion

In conclusion, this study demonstrates 3 key aspects of electric current induced neuronal activation in *C. elegans* :

- Direct electric current pulse can be used to probe the functionality of the neuron and quantify parameters (eg. aging) that might affect it.
- The magnitude and polarity of the current results in distinct cellular phenomenon (i.e neuronal depolarization versus hyperpolarization).
- It is possible to selectively activate parts of the worm body due to the novel microelectrode-microfluidic integration scheme.

Furthermore, compared to other forms of stimuli (chemical, mechanical and thermal), the ease with which, an electrical stimulus can be precisely controlled in terms of delivery, strength and spatial location, makes it a powerful tool to probe into the physiology of the nervous system of *C. elegans* and study its age-dependent properties. We envision the use of electrical stimulation as a well controllable and highly tunable stimulus for performing *in vivo* functional imaging, as part of a high-throughput anti-aging drug screening assay.

5.5 Experimental Methods

All methods except for the 'e-chip' microfabrication are the same as that described in chapter 4 (section 4.4).

5.5.1 'e-chip' microfabrication

The microfabrication process consists of three steps:

Step 1: Fabrication of ITO (Indium Titanium Oxide) electrodes on a glass coverslip.

A layer of ITO is first sputtered to a thickness of 150 nm on a glass coverslip (#1.5). A positive photoresist is then spun over the ITO and patterned using photolithography to define the electrodes. The electrodes are formed by wet etching the exposed ITO for approximately 1 minute in a 1:1 solution of HCL:H_20. The remaining photoresist is stripped using acetone and the coverslip is cleaned using isopropanol.

Step 2: Fabrication of the PDMS microfluidic chip.

The PDMS microfluidic chip is fabricated using soft lithography. A three-layer SU-8 mold is first created using a three-step photolithography process. The first SU-8 layer contains the microfluidic channel that connects the flush-channel with the worm trap. The second SU-8 layer contains the worm trap, while the third layer includes the worm and buffer inlet channels, outlet channel and the flush channel. PDMS is poured onto the SU-8 mold and allowed to cure at 65 ºC for approximately 3 hours. The PDMS layer is then peeled off from the SU-8 mold and punched using a hole puncher to form the fluidic inlets and outlets. We fabricated three different SU-8 molds for conducting experiments with Day 1, 3 and 5 worms respectively. The thickness of the first SU-8

layer in each of these molds was 7 μm, while the second and third SU-8 layers were patterned to the thickness values reported in **Table 4.1**.

Step 3: Assembly of the e-chip.

The e-chip is assembled by aligning and bonding the PDMS chip to the ITO-patterned glass coverslip using air plasma (50 W, 250 mTorr, 35 s). As PDMS does not bond very strongly to ITO, we used an epoxy glue (5-minute epoxy from Ace Hardware) to secure the PDMS chip on the glass coverslip. In order to access the ITO electrodes, we glued copper wires to the exposed ITO pads on the glass slide using a conductive silver epoxy (8331-14G from mgchemicals).

CHAPTER 6

Hardware-based Emulation Of The Functionality Of The ASH Chemosensory Neuron In *C. elegans*.

Hardware based emulation of the nervous system has long been proposed as a computational platform for real-time simulation and investigation of biological neuronal networks. Developing such a computational platform for *C. elegans* nervous system is a feasible goal because: a) it has a simple nervous system (302 neurons with approximately 7000 synapses), and b) there exists a complete description of the morphology and synaptic connectivity of its entire nervous system. As a step towards this goal, here we present an analog circuit for emulating the functionality of the worm's chemosensory ASH neuron. The circuit was designed to implement a first-order differential equation model of the stimulus-evoked calcium transients in the ASH neuron. We simulated this circuit in CADENCE as well as built it on a breadboard. The transient response of this circuit to a step input was qualitatively similar to the stimulus-evoked calcium transients presented in Chapter 4 and 5.

6.1 Introduction

The synergy of microfluidic devices/systems for manipulating *C. elegans* with optical imaging techniques for monitoring neuronal activity has unearthed a plethora of possibilities in the neurobiology of *C. elegans* [80], [81]. The microfluidics assisted

neuronal recording approach/machinery in *C. elegans* has allowed monitoring spatiotemporal dynamics of a population of neurons and correlate them with the worm's behavior [79], [50], [51]. With this approach, as data from a large population of neurons become available, computational procedures would become valuable as experimental tools for uncovering new insights about the connections, architecture, and overall functionality of worm's nervous systems.

Computational procedures in neuroscience typically involve the use of mathematical/computational models to provide a quantitative description of the functionality the nervous system. These computational models capture the essential features of the nervous system at multiple spatial-temporal scales, including but not limited to single ion channel dynamics, behavior of neuronal networks, learning, memory and sensory processing [113], [114], [115]. Although very useful, their use has often been limited to simulations of small neuron networks so as to keep the computational complexities to a minimum. Computational models (such as Multi-compartment neuron models) that attempt to account for detailed physiological aspects of a neuron can easily require hundreds of differential equations [113]. And, thus, an effort to simulate the behavioral dynamics of a large population of neurons might be a challenging as well as an expensive computational task.

Advances in high-speed computational platforms and procedures have been deemed critical for breaking the computational barriers that limit large-scale neuronal network simulations. Towards this end, several researchers have proposed the use of

dedicated supercomputers [116] and large-scale digital gate arrays [117]. However, the quest for such high-speed digital simulations overlooks the fact that the single neuron dynamics underlying the deterministic or digital communication between neurons are inherently analog in nature. And therefore, several researchers have proposed the development of Analog Very-Large-Scale-Integrated (aVLSI) circuits for emulating the analog-digital hybrid architecture of a biological nervous system [118], [119], [120]. The inherent dense and parallel architecture of aVLSI circuits, offers an exceptional computational medium for hardware implementation and thus, real-time operation of large-scale neuron network simulations [121], [122]. Therefore, unlike general purpose computers, aVLSI circuits can enable the investigation of large-scale neuron networks without waiting for hours or days for the simulation to run.

Several aVLSI circuits have been designed to model the complex dynamics of neuronal ion channels and synaptic channels. These circuits [reviewed in (Ref. 123)] have been used as fundamental building blocks for real-time emulation of the electro-physiological behavior of large neuronal networks as observed in biological systems. Numerous circuit design strategies have been proposed in the literature for implementing these circuits. These strategies can be primarily grouped into two categories, a) Bottom-Up and b) Top-Down.

a) Bottom-Up strategy

This strategy involves designing circuits that can model the conductance dynamics of individual ion channels and using them as fundamental building blocks to emulate the

behavior of the entire neuron. Circuits designed for implementing the ion channel dynamics have been based on two approaches, as described below.

- *Biophysical modeling approach* - This approach exploits the biophysical equivalence between the transport of ions in a biological neuron and charge carriers in a transistor [124], [125]. In both cases, charges are transported across a voltage controlled energy barrier. For the neuron, ions (such as Na^{+2}, K^{+} and Ca^{+2}) are transported across the voltage gated ion channels, whereas for the transistor, electrons or holes are transported across the voltage controlled source-drain channel. And, interestingly, in both instances, the transport of charge across the energy barrier is governed by a Boltzman distribution, which results in an exponential voltage dependence. These similarities have been successfully utilized to design silicon models of ionic channels using sub-threshold mode transistors. Furthermore, multiple instances of such silicon ionic models have been utilized to build Hodgkin-Huxley based neurons as well as emulate the activity of real neurons such as the thalamus relay neuron.
- *Phenomenological modeling approach* - This approach utilizes the differential equation models (such as Hodgkin-Huxley [126] and FitzHugh-Nagumo [127] neuron models), that have been formulated for describing the ion channel dynamics. Silicon ionic models are built by directly implementing these differential equations on analog circuits [128], [129].

b) Top-Down strategy

This strategy involves designing circuits that directly extract the neuronal activity without reproducing the detailed dynamics of individual ion channels. Several SiN (Silicon

Neurons) circuits have been reported in the literature that directly emulate the action potentials (also known as spikes) observed in mammalian neurons [119], [123]. These circuits particularly attempt to reproduce the characteristic metrics of action potentials which include, the spike threshold, refractory period, spike frequency adaptation as well as threshold adaptation. This strategy reproduces neuronal activity dynamics with reduced circuit complexity and as a result makes the approach feasible for implementing large networks of neurons.

Here, we propose to utilize aVLSI circuits to emulate the nervous system of *C. elegans*. The nervous system of *C. elegans* comprises 302 neurons with approximately 7000 synapses [130]. Moreover, unlike other multicellular organisms, *C. elegans* nervous system has been mapped out down to the synaptic level [130]. This unique advantage, makes the aVLSI based hardware implementation of *C. elegans* nervous system, a feasible goal. As a step towards this goal we demonstrate the design and implementation of an analog circuit for emulating the functional response of the ASH chemosensory neuron in *C. elegans*. We would like to highlight that, unlike mammalian neuron, *C.elegans* neurons do not show any spiking behavior or action potentials [131], [132]. And, as most SiN circuits reported in the literature, emulate the spiking behavior of mammalian neurons, they cannot be directly employed for emulating *C. elegans* neurons. Here, we utilized a combination of the phenomenological modeling approach and the Top-Down circuit design strategy for emulating the functionality of the ASH neuron.

6.2 Results and Discussion

6.2.1 A first-order differential equation model for the ASH neuron response

We first constructed a mathematical model to simulate the response of the ASH neuron. The response of many *C. elegans* sensory neurons (including ASH) is believed to be governed by two different types of functional cells [133], 1.) On-Cell and 2.) Off-Cell. These cells shape the neuron's response at the onset (On-Cell) and offset of a stimulus (Off-Cell). Depending on the type of the stimulus, either one or both cells might contribute to the neuron's stimulus-evoked response. For example, in case of a chemical stimulus such as glycerol, both cells might contribute to the neuron's response while in case of an electrical stimulus only the On-Cell might contribute. For the sake of clarity, we present the ASH neuronal responses to these stimuli in **Figure 6.1**.

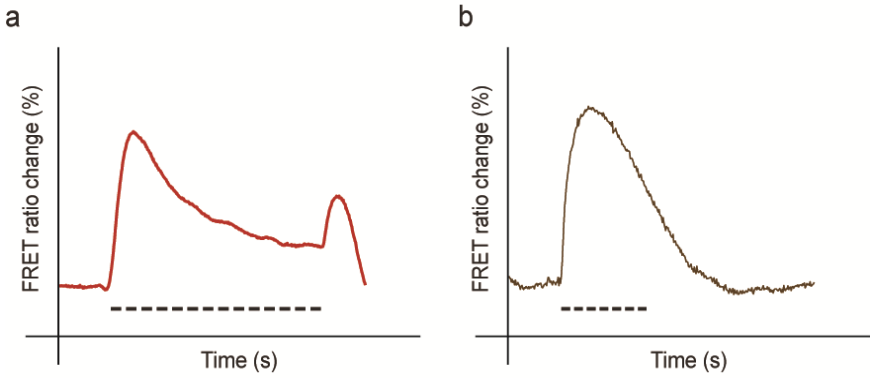

Figure 6.1: Experimentally obtained calcium transient in ASH neuron in response to different stimuli. **(a)** For a chemical stimulus (Glycerol). **(b)** For an electrical stimulus (electric current). The dashed line represents the presence of the stimulus.

The functionality of both 'Cells' was modeled with a first-order differential equation as shown below:

- Differential equation model for the 'On-Cell' :

$$\frac{\mathrm{d\ Ca(t)}}{\mathrm{dt}} = \phi_{on} * \mathrm{I}_{on} * e^{-\mathrm{I}_{on}.\tau_{on}.\mathrm{t}} - \beta_{on} * \mathrm{Ca(t)} \qquad \textbf{Eq}^{\mathbf{n}}\ \mathbf{6.1}$$

$$\frac{\mathrm{d\ Ca(t)}}{\mathrm{dt}} = \alpha_{on} * \mathrm{e}^{-\mathrm{I}_{on}.\tau_{on}.\mathrm{t}} - \beta_{on} * \mathrm{Ca(t)} \qquad \textbf{Eq}^{\mathbf{n}}\ \mathbf{6.2}$$

Where,

$$\mathrm{t}_{on} \leq \mathrm{t} \leq \mathrm{t}_{off}$$

$$\alpha_{on} = \phi_{on} * \mathrm{I}_{on}$$

$$\alpha_{on} * \mathrm{e}^{-\mathrm{I}_{on}.\tau_{on}.\mathrm{t}} = influx\ term$$

$$-\beta_{on} * \mathrm{Ca(t)} = efflux\ term$$

This equation (**Eq$^{\mathbf{n}}$ 6.2**) relates the rate of change of calcium to the rate of influx and efflux of calcium in the cell. It states that, upon the onset of stimulus (i.e. at time $t = t_{on}$), (a) calcium enters the cell at a rate equal to 'α_{on}' (calcium influx), which then decays exponentially with a time constant '$I_{on}*\tau_{on}$' and (b) the neuron depletes itself of calcium at a rate proportional to the extra Ca^{2+} present inside the cell due to depolarization, with a proportionality constant, 'β' (Ca^{2+} efflux). Here, 'I_{on}' models the dependency between the rate of calcium influx and the duration of the calcium transient, stating that, shorter duration calcium transients are accompanied with higher rates of calcium influx.

- Differential equation model for the 'Off-Cell' :

$$\frac{\mathrm{d\ Ca(t)}}{\mathrm{dt}} = \phi_{off} * \mathrm{I}_{off} * e^{-\mathrm{I}_{off}.\tau_{off}.\mathrm{t}} - \beta_{off} * \mathrm{Ca(t)} \qquad \textbf{Eq}^{\mathbf{n}}\ \mathbf{6.3}$$

$$\frac{\mathrm{d\ Ca(t)}}{\mathrm{dt}} = \alpha_{off} * e^{-\mathrm{I}_{off}.\tau_{off}.\mathrm{t}} - \beta_{off} * \mathrm{Ca(t)} \qquad \textbf{Eq}^{\mathbf{n}}\ \mathbf{6.4}$$

Where,

$$t \geq t_{off}$$

$$\phi_{off} = \int_{t_{on}}^{t_{off}} \alpha_{on} * e^{-I_{on}.\tau_{on}.t}\ dt$$

$$\alpha_{off} = \phi_{off} * I_{off}$$

$$\alpha_{off} * e^{-I_{off}.\tau_{off}.t} = influx\ term$$

$$-\beta_{off} * Ca(t) = efflux\ term$$

The form of this differential equation (**Eq^{n} 6.4**) is similar to that of the 'On-Cell'. However, unlike the 'On-Cell', the influx term for the 'Off-Cell' depends on the total calcium influx during the presence of the stimulus, as indicated by the term ϕ_{off}. This equation (**Eq^{n} 6.4**) states that, upon the offset of the stimulus (at $t = t_{off}$), (a) calcium enters the cell at a rate equal to 'α_{off}', which then decays exponentially with a time constant '$I_{off}*\tau_{off}$' and (b) the neuron depletes itself of calcium at a rate proportional to the extra Ca^{2+} present inside the cell, with a proportionality constant, 'β_{off}' (Ca^{2+} efflux).

6.2.2 Analog circuit design for emulating the ASH neuron response

We designed an analog circuit to implement the 'On' and 'Off' cell responses and utilized them as fundamental building blocks to reproduce the observed ASH neuronal responses to different stimuli. To do so, we built an analog circuit that implemented the differential equation models described in **Eq^{n} 6.2** and **Eq^{n} 6.4**. The basic architecture of this analog circuit consists of three sub-blocks (**Figure 6.2**): 1.) Influx, 2.) Efflux and 3.) Integrator.

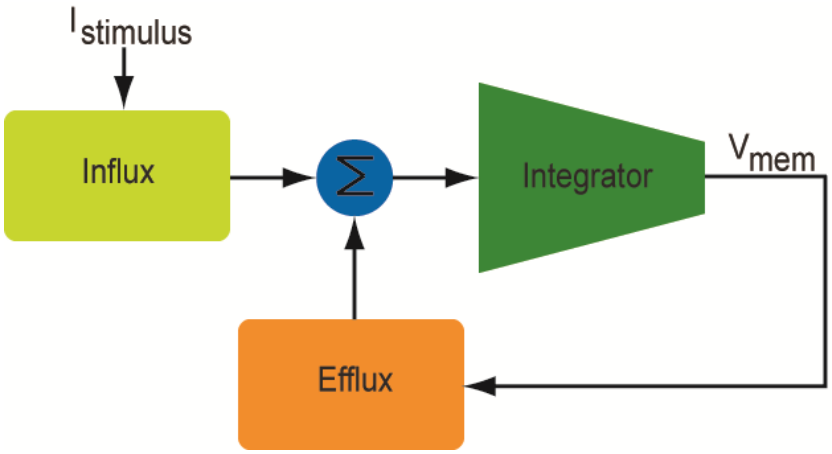

Figure 6.2: Architecture of the analog circuit designed for emulating the ASH response. This architecture implements the differential equations illustrated in **Eq^{n} 6.2** and **Eq^{n} 6.4**. The influx and the efflux sub-blocks output a current that represents the influx and efflux terms in these equations, while the integrator sub-block evaluates the equation and outputs a voltage that represents the instantaneous calcium concentration.

The Influx and Efflux sub-blocks consist of transconductance analog circuits and output a current proportional to the rate of Ca^{+2} influx and efflux inside the cell, respectively. The difference of the current output from the Influx and Efflux sub-blocks is integrated onto a capacitor by the integrator block. This capacitor represents the neuronal cell membrane, while the voltage on the capacitor represents the net calcium flux inside the cell. Next, we present a detailed description of the sub-circuits that constitute the individual sub-blocks (influx, efflux and integrator) for each cell type (On-Cell and Off-Cell).

a) 'On-Cell' Circuit

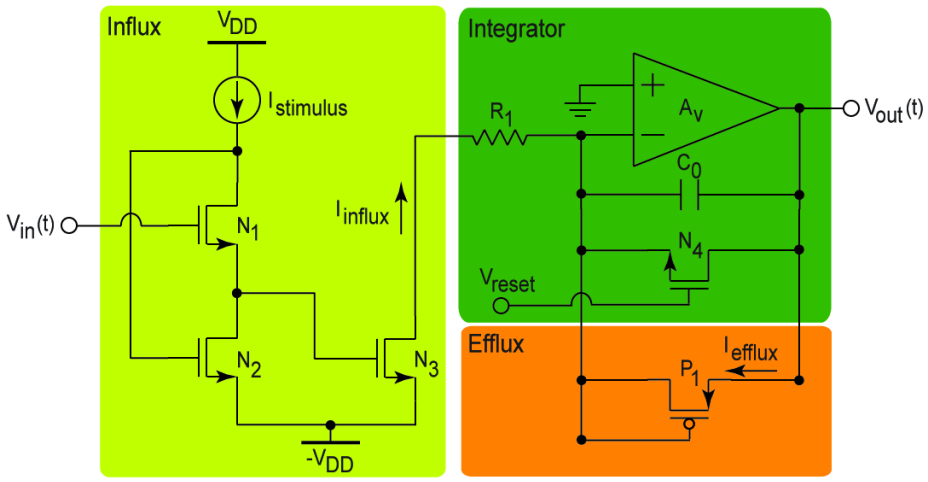

Figure 6.3: Transistor level circuit for emulating the On-Cell response.

- **Influx sub-block**

This sub-block emulates the rate of influx of calcium, which is modeled by the first term in **Eq^{n} 6.2**. The sub-circuit consists of transistors N1-N3 and the current source $I_{stimulus}$. The input current $I_{stimulus}$ is selected such that transistors N2 and N3 operate in the subthreshold region. Transistor N1 is used as a voltage controlled resistor, where its resistance is increased with time. To understand the operation of this circuit, consider the circuit shown in **Figure 6.4**.

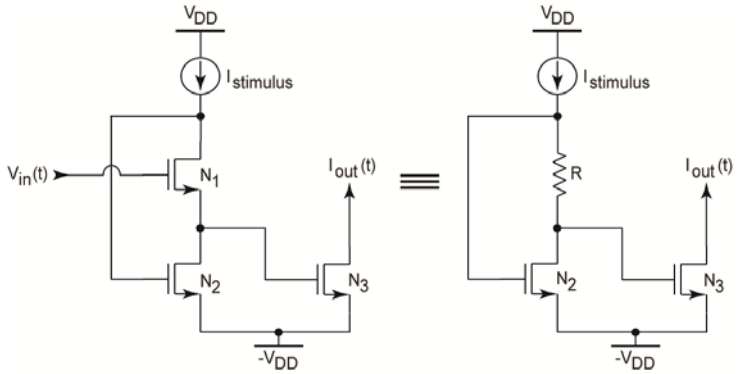

Figure 6.4: Circuit for the Influx sub-block.

Here R is used to represent the resistance offered by transistor N1 at a particular time instance. Using KVL around the gate-source loop of N2 and N3 gives,

$$V_{GS2} - V_{GS3} - I_{IN}R = 0 \qquad \textbf{Eq}^{\textbf{n}}\ \textbf{6.5}$$

Assuming, equal threshold voltages for N2 and N3, **Eq^{n} 6.5** can be reduced to **Eq^{n} 6.6**, where V_{OV} ($V_{OV} = V_{GS} - V_T$) represents the transistor's overdrive voltage. The overdrive voltage for a transistor operating in the subthreshold region with $V_{DS} >> V_T$, is given by **Eq^{n} 6.7** [134].

$$V_{OV2} = V_{OV3} - I_{IN}R \qquad \textbf{Eq}^{\textbf{n}}\ \textbf{6.6}$$

$$V_{GS} - V_T = V_{OV} \approx nV_T \ln\left(\frac{I_{DS}}{\left(\frac{W}{L}\right) I_t}\right) \qquad \textbf{Eq}^{\textbf{n}}\ \textbf{6.7}$$

Substituting **Eq^{n} 6.7** into **Eq^{n} 6.6**, we get,

$$nV_T \ln\left(\frac{I_{IN}}{\left(\frac{W_2}{L_2}\right) I_t}\right) = nV_T \ln\left(\frac{I_{OUT}}{\left(\frac{W_3}{L_3}\right) I_t}\right) - I_{IN}R \qquad \textbf{Eq}^{\textbf{n}}\ \textbf{6.8}$$

Solving **Eq^{n} 6.8** for I_{OUT} assuming equal W/L ratios for N_2 and N_3, we get,

$$I_{OUT} \approx I_{IN} \exp\left(\frac{I_{IN}R}{nV_T}\right) \qquad \textbf{Eq}^{\textbf{n}}\ \textbf{6.9}$$

It should be noted that the resistance R is function of time. We assume that R varies linearly with time, with a proportionality constant K, i.e. $R \approx Kt$ (t denotes time). Incorporating this in **Eq^{n} 6.9**, we get,

$$I_{OUT} \approx I_{IN} \exp\left(\frac{I_{IN}Kt}{nV_T}\right) \qquad \textbf{Eq}^{\textbf{n}}\ \textbf{6.10}$$

The form of **Eq^{n} 6.10** is similar to that of the influx term in **Eq^{n} 6.2**. The value of I_{IN} is set to represent the strength of the stimulus while the output current, I_{OUT}, represents the rate of calcium influx.

- **Efflux sub-block**

This sub-block emulates the rate of efflux of calcium, which is modeled by the second term in **Eq^n 6.2** and comprises the sub-circuit shown in **Figure 6.5**.

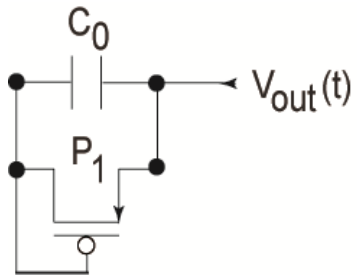

Figure 6.5: Circuit for the Efflux sub-block.

The sub-circuit consists of an RC circuit formed by the diode connected transistor P_1 and the capacitor C_0. The source of P_1 is driven by the voltage on C_0. Here, P_1 serves as a voltage controlled resistor and modulates the rate of decay of the charge stored on C_0. The resistance offered by P_1 decreases as the voltage on C_0 increases. As a result, the instantaneous rate of decay of the voltage (V_{C0}) on C_0 or equivalently the current I_{OUT} flowing through P_1 is proportional to the magnitude of the voltage V_{C0}, as shown in **Eq^n 6.11**.

$$\frac{\partial V_{C0}}{\partial t} \approx I_{OUT} = -\beta V_{C0} \qquad \textbf{Eq}^n\ \textbf{6.11}$$

The form of **Eq^n 6.11** is similar to the efflux term in **Eq^n 6.2**. The voltage V_{C0} on C_0 represents the net calcium flux inside the cell, while I_{OUT} represents the rate of calcium efflux.

- **Integrator sub-block**

This sub-block integrates the difference of the current output from the influx and efflux sub-blocks onto a capacitor.

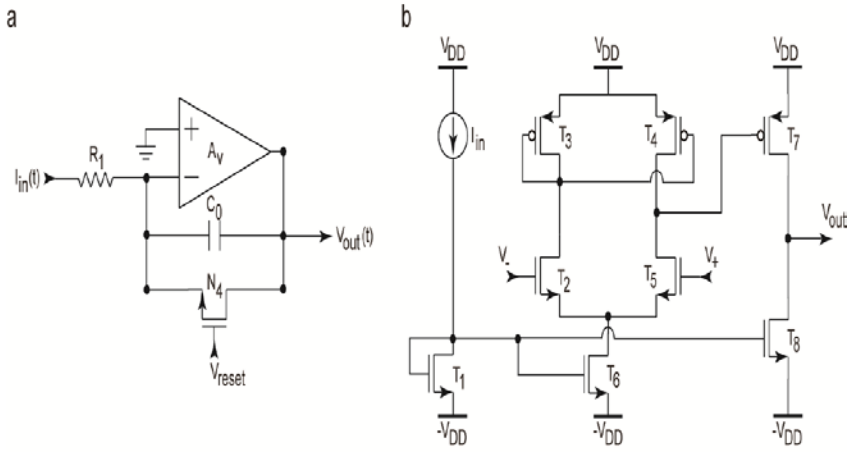

Figure 6.6: Circuit for the Integrator sub-block. **(a)** Schematic of the integrator. Here, $I_{in}(t)$ which represents the difference of the current output from the influx and efflux sub-blocks is integrator onto the capacitor C_0. **(b)** Transistor level circuit of the differential amplifier incorporated in the integrator shown in (a).

The integrator comprises a differential amplifier and a capacitor C_0 as shown in **Figure 6.6a**. The transistor N_4 is used as a switch to reset or nullify the charge stored on C_0. The differential amplifier incorporated in the integrator is shown in **Figure 6.6b**. It consists of three stages. The first stage is a single ended differential amplifier. The second stage is common source amplifier and the third stage is a source follower. The open-loop gain of the differential amplifier was 280.

b) 'Off-Cell' Circuit

The circuit designed for emulating the 'Off-Cell' response in shown in **Figure 6.7**. Similar to the 'On-Cell' circuit, the basic architecture of this circuit comprised three

sub-blocks namely, the influx, efflux and the integrator. Moreover, except for the influx sub-block, the efflux and the integrator sub-blocks incorporate the same sub-circuits as those utilized in the 'On-Cell' circuit.

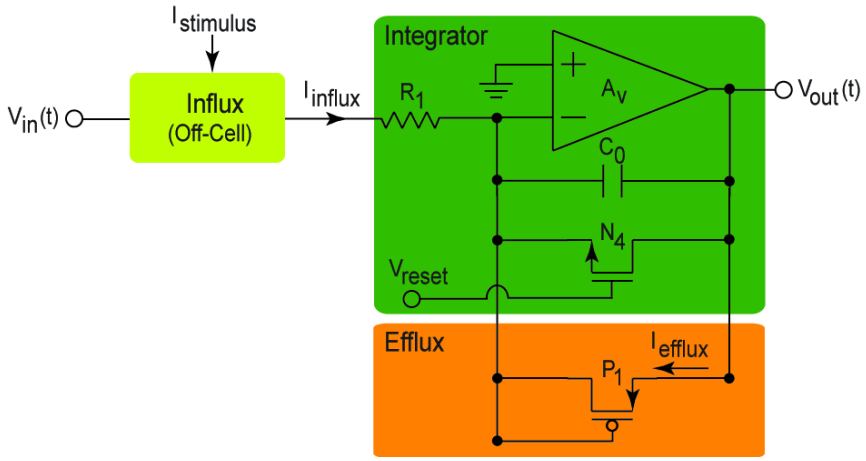

Figure 6.7: Transistor level circuit for emulating the Off-Cell response.

- **Influx sub-block**

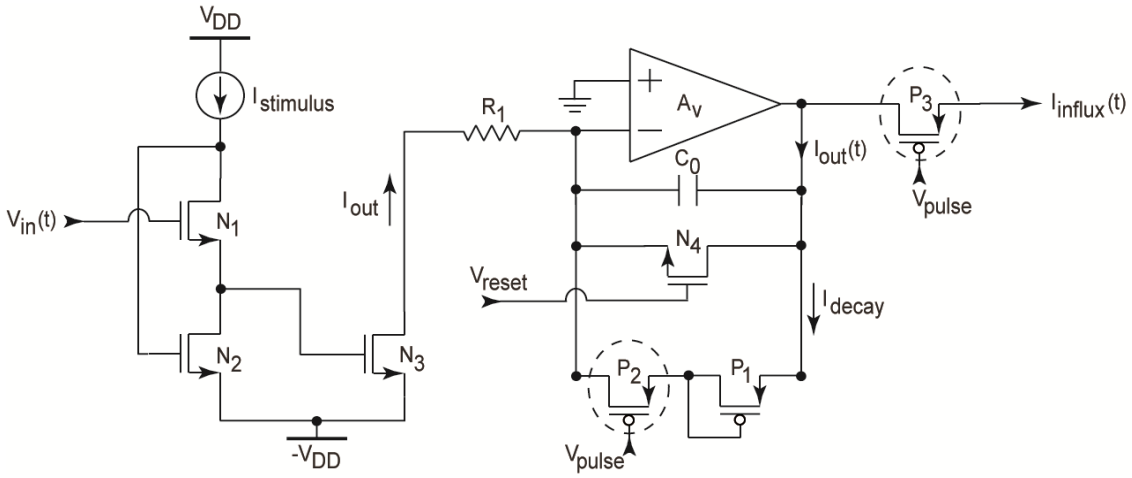

Figure 6.8: Circuit for emulating the Influx sub-block in the 'Off-Cell'.

The sub-circuit for the influx sub-block comprises a modified version of the 'On-Cell' circuit (**Figure 6.8**). These modifications include the presence of transistors N_5 and

N_6 (shown by dashed circles in Figure 6.8). These transistors are essentially used as switches and serve to represent the presence or absence of the stimulus. These switches are driven by a pulse (V_{pulse}). When V_{pulse} is low - which represents the presence of the stimulus – N_5 and N_6 are switched off and the current, I_{out} , which is given by **Eq^n 6.10**, is integrated onto C_0 (**Figure 6.8**). We should highlight that, N_5 remains off when V_{pulse} is low and as a result, the voltage developed on C_0 does not decay significantly during this time period. Consequently, this voltage represents the term α_{off} in **Eq^n 6.4**. When V_{pulse} is high - which represents the absence of the stimulus - N_5 and N_6 are switched on. Subsequently, P_1 turns on and initiates the decay of the voltage developed on C_0. This gives an output current which is similar in form to the influx term in **Eq^n 6.4**.

6.2.2 Simulation Results

We utilized the ‘On-Cell’ and ‘Off-Cell’ circuits as building blocks to simulate the ASH calcium transients in response to a chemical and electrical stimulus. We configured these building blocks as illustrated in **Figure 6.9** and acquired the circuit’s output in response to a positive step input applied at the terminal - V_{pulse}. Here, the step input – V_{pulse} , represents the stimulus. The output transient characteristics as shown in **Figure 6.10** are qualitatively similar to the stimulus-evoked calcium transients in the ASH neuron (**Figure 6.1**).

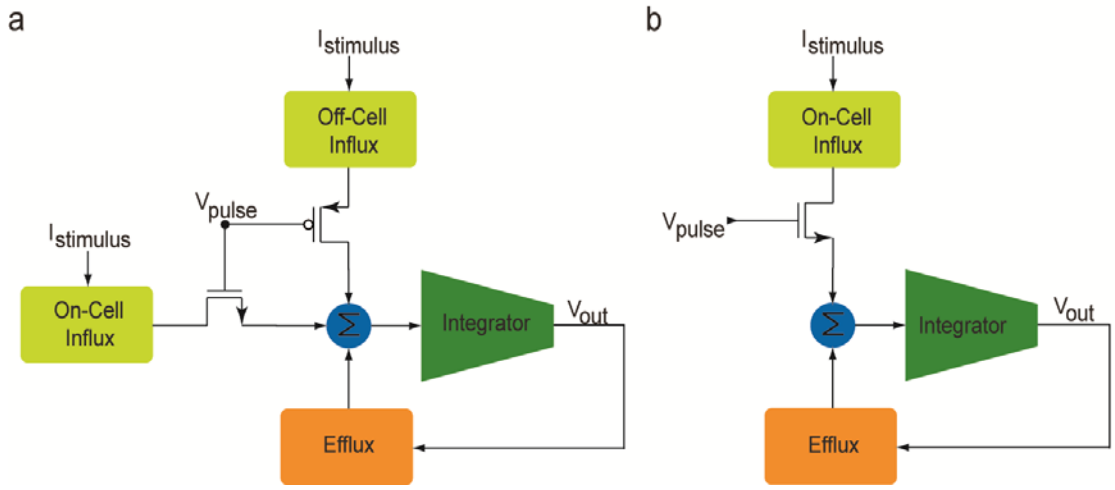

Figure 6.9: Architecture of the circuit designed to simulate the ASH neuron calcium transients in response to, **(a)** a chemical stimulus and **(b)** an electrical stimulus.

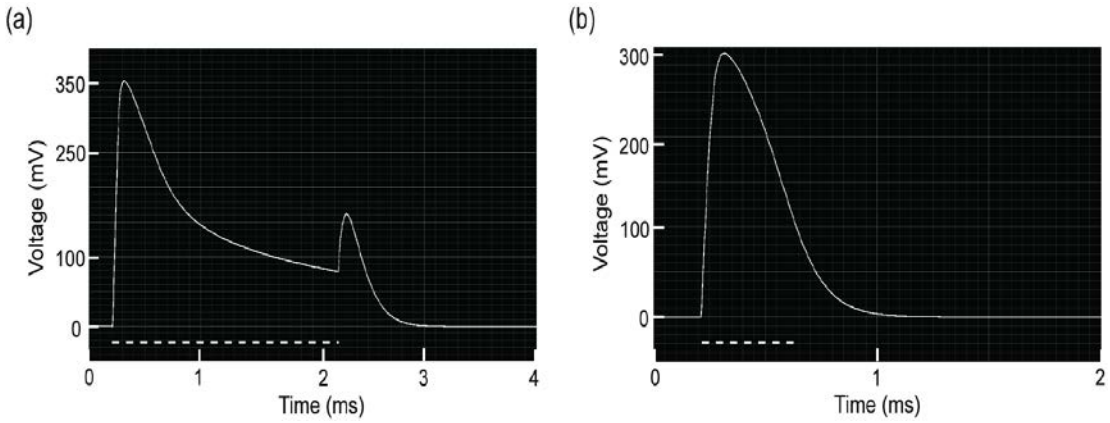

Figure 6.10: Transient response of the circuit designed for simulating the ASH calcium transients in response to, **(a)** a chemical stimulus and **(b)** an electrical stimulus. In both cases, the output was acquired in response to a positive step input whose pulse width is denoted by the dashed line.

6.2.3 Hardware based emulation of the ASH neuron response

We further built breadboard prototypes of the proposed circuits (both 'On' and 'Off' cells) and utilized them as building blocks to demonstrate hardware based emulation of the ASH neuron response. This prototype was built using off-the-shelf

components which included, BJT's (Bipolar Junction Transistor), Operational Amplifiers (LM741C) and a MOSFET array (MC10000B). We should highlight that the MOSFET's used in the circuit shown in **Figure 6.4** were replaced with BJT's in the breadboard prototype. This however, does not alter the circuit's functionality, because the I-V (Current vs Voltage) characteristic of a BJT is analogous to that of the sub-threshold mode MOSFET, i.e. the output current in both cases is an exponential function of the input voltage. We configured the 'On-Cell' and 'Off-Cell' circuit blocks as illustrated in **Figure 6.9** and acquired the output transients ($V_{out}(t)$ in **Figure 6.9**) in response to a positive step input applied at the terminal V_{pulse} (shown in **Figure 6.9**). The form of the output transients (**Figure 6.11**) is similar to the stimulus-evoked ASH neuron calcium transients shown in **Figure 6.1**.

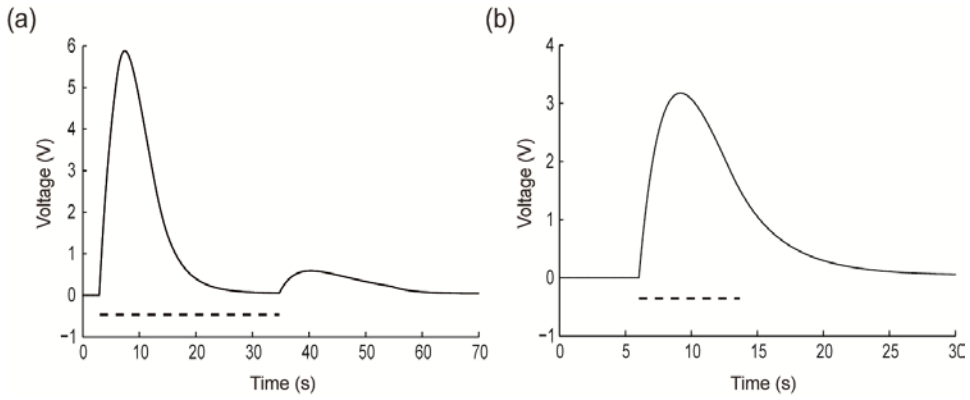

Figure 6.11: Transient response of the breadboard prototype circuit built designed for emulating the ASH calcium transients in response to, **(a)** a chemical stimulus and **(b)** an electrical stimulus. In both cases, the output was acquired via a DAQ card, in response to a positive step input whose pulse width is denoted by the dashed line.

6.3 Conclusion

Here, we presented an analog circuit that can emulate the observed neuronal activity in *C. elegans*. The circuit was designed to implement a first-order differential

equation model of the chemosensory neuron, ASH, in *C. elegans*. Drawing analogy to the 'On' / 'Off' coding strategy exhibited by the worm's sensory neurons [133], two different circuit blocks - 'On-Cell' and 'Off-Cell' - were designed to emulate the ASH neuron response at the onset and offset of a stimulus, respectively. The circuit architecture of each of these blocks was modularized into different sub-circuits (influx, efflux and integrator) whose parameters (such as the input current, gain, input/output impedance, etc) could be individually tuned to modulate the different characteristic metrics (such as the rate of calcium influx, rate of calcium efflux and the amplitude of the calcium transient) observed in the worm's neuronal responses. We utilized the 'On-Cell' and 'Off-Cell' circuits as fundamental building blocks to implement silicon neurons (in software as well as on hardware), whose input output characteristics were qualitatively similar to the stimulus-evoked ASH neuron responses. It should be emphasized that, here, we did not make any attempt to optimize the performance of the proposed silicon neuron circuits in terms of their size and power consumption. However, this would be of utmost importance while implementing large arrays of silicon neurons for emulating the activity of a network of neurons.

A unique advantage of any hardware based computational platform is its ability to operate in real-time. Hence, we believe that such a computational platform would allow to simulate and investigate in real-time, the different computational paradigms used by neuron circuits to generate complex behavioral patterns displayed by *C. elegans*. For example, chemotaxis in *C. elegans*, which is defined as the worm's locomotion behavior in response to a chemical attractant or repellant, critically depends on the worm's ability

to compute the rate of change of the chemical concentration as it moves through its environment [135], [133]. This computation, in turn, is performed by a network of chemosensory neurons, interneurons and motorneurons as shown in **Figure 6.12**.

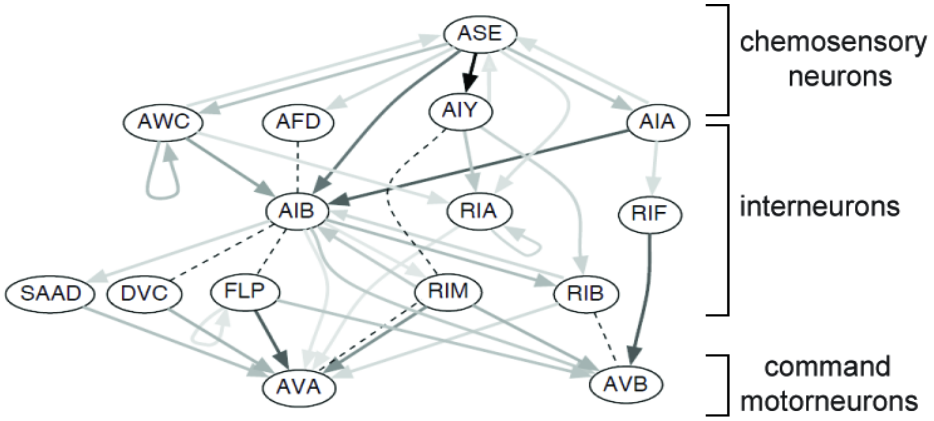

Figure 6.12: A chemosensory neuron network in *C. elegans* [adapted from [133]]. Shown are the polysynaptic interneuron pathways that communicate information from the chemosensory neuron ASE to the command motor neurons AVA and AVB. Here, arrows denote chemical synapses while the dashed lines denote gap junctions.

The chemosensory neurons sense the chemical stimulus and with the help of interneurons, communicate this information to the motorneurons which finally innervate the locomotory muscles of the worm and result in a specific locomotion pattern. Here, we should highlight that the communication pathways from the chemosensory neurons to the command motorneurons are overwhelmingly polysynaptic [130], [136] and this makes the experimental investigation of these neuronal pathways a daunting challenge. In such cases, we believe that a hardware based computational platform involving silicon neurons would enable an efficient investigation of these neuronal pathways. For example, a network of (SiN) silicon neurons can be connected in a fashion similar to the connectivity of neurons in *C. elegans* and then by activating and deactivating specific neurons on hardware, one can investigate different communication pathways in the network and

hypothesize the impact they might have on the worm's locomotion pattern. By modulating the strength of communication between silicon neurons (via the inclusion of weights), one can study the impact of variations in synaptic strengths on the signal propagation within the worm's neuronal network.

We believe that, the complete description of the morphology and synaptic connectivity of all the neurons (302 neurons with approximately 7000 synapses) in *C. elegans* [130], raises the prospects of developing a hardware based computational platform for emulating the entire nervous system of *C. elegans*. We envision that such a platform would assist neurobiologists in making inferences about the neuronal origins of the wide repertoire of behavioral patterns displayed by the worm.

CHAPTER 7

Conclusions and Future Work

7.1 Conclusions

The unique ability of microfluidics to handle small-sized objects has enabled the development of several microfluidic devices to conduct neuroscience studies in *C. elegans*. The key features that make these devices powerful for *C. elegans* research, include 1) they can be fabricated in an inexpensive manner via soft-lithography, 2) they can be constructed out of PDMS – an optically transparent and gas permeable elastomer, which allows to maintain the preparation, both visible as well as viable, 3) they can create well-controlled micro-environments for the worms to reside in, which greatly reduces experimental variability resulting from chemical or physical changes in the environment, 4) they are amenable to automation, which facilitates the acquisition of a large amount of statistically meaningful data, and 5) fluid flow inside micron sized channels is laminar and thus allows to precisely deliver a fluidborne stimulus with immense precision. Here, we utilized these advantages and demonstrated the design and development of microfluidic devices/systems for manipulating *C. elegans* as well as imaging stimulus-evoked activity in their nervous system. The important contributions of this thesis include:

7.1.1 Microfluidic approaches for immobilizing and imaging *C. elegans*

Immobilization of *C. elegans* (~40-50 μm in diameter and 1 mm long) constitutes an important step for many experiments that are based on the observation of cellular and sub-cellular features in intact worms. These experiments include laser ablations of neurons for studying neuronal networks and axon regeneration [57-59], monitoring neuronal responses at the presence of various stimuli [60], analyzing the nematode's anatomical features [61] and imaging cellular development and gene expression [62]. To this end, we demonstrated two microfluidic approaches for immobilizing *C. elegans*.

- *CO_2 immobilization* - This approach creates a CO_2 micro-environment to cease the worm's movement and it proved to be efficient for the long term worm immobilization (1-2 hours).
- *Compressive immobilization* – This approach utilizes a deformable membrane to mechanically restrict the worm and it is appropriate for immobilizing the worm for shorter periods of time (minutes).

Both techniques can be used to immobilize worms of different age groups (L4's to adults). The proposed techniques are easy to implement and allow worm recovery within a few seconds after immobilization. Additionally, the CO_2 method offers the advantage of long-term fluorescent imaging due to the creation of low-oxygen environment that reduces fluorescent photobleaching. This long-term fluorescence imaging capability of the 'CO_2 immobilization' technique was employed to visualize the movement of chromosomal structures inside the cell.

7.1.2 An automated microfluidic platform for calcium imaging in *C. elegans*

Calcium imaging is an optical imaging technique that allows monitoring of the amount of Ca^{2+} inside the cell. This technique has been considered as a prime method for monitoring the neuronal activity in *C. elegans*. To this end, we demonstrated a microfluidic platform for automated calcium imaging methodology that enabled the characterization and statistical analysis of neuronal functionality from large populations of worms.

- **Calcium imaging microfluidic platform**

The platform consists of a microfluidic biochip, an epifluorescent microscope equipped with a z-moving stage, a dual-color imager (for FRET imaging) attached to a back-illuminated CCD camera, and a valve manifold for controlling the delivery of the stimulus, buffer and worm-containing solutions. The platform was interfaced to a custom made labVIEW software which facilitated the acquisition of stimulus evoked calcium imaging data. Depending on the application, the platform is capable of acquiring data from tens to hundreds of worms in an hour. The use of a generic interface (labVIEW) that is compatible with most off-the-shelf hardware devices (eg. CCD camera, shutter controllers, data acquisition boards, etc) makes the platform an easy-to-use tool that can be replicated by other researchers or interfaced with other imaging setups.

- **Stimulus-evoked calcium imaging in *C. elegans***

The operation of the platform is versatile with respect to different microfluidic designs that can deliver different forms of stimuli (eg. chemical, mechanical, thermal or

electrical). To demonstrate this, we designed two microfluidic devices for stimulating the worm with a chemical and an electrical stimulus. We interfaced these devices with the microfluidic platform and monitored the worm's neuronal activity in response to a chemical stimulus (glycerol) as well an electrical stimulus (electric current). The form of the neuronal calcium transients was observed to be dependent on the type of stimulus used. The chemical stimulus – glycerol - evoked a biphasic neuronal response, i.e. it caused the neuron to respond when the stimulus was switched on as well as switched off. On the other hand, the electrical stimulus – electric current – evoked a response only when the stimulus was switched on. More importantly, we showed for the first time that : (i) electric current can be used to induce neuronal activation (previous work by other groups have used electric fields and not electric currents), (ii) it is possible to selectively activate parts of the worm body (e.g. head, tail) due to the novel microelectrode-microfluidic integration scheme, (iii) the magnitude and polarity of the electric current give rise to distinct cellular phenomena (e.g. neuronal depolarization versus hyperpolarization).

- **Effects of aging on neuronal functionality in *C. elegans***

The ability of the platform to acquire large amounts of calcium imaging data was utilized to study aging of the nervous system – a stochastic process which requires a large dataset in order to obtain statistically significant conclusions. We studied the effects of aging on the stimulus-evoked neuronal functionality in *C. elegans*. The stimulus-evoked neuronal activity in both cases – chemical as well as electrical stimulus – was observed to be age-dependent. Moreover, distinct trends in the age-dependent neuronal functionality

were observed for each stimulus. Glycerol evoked neuronal activity was observed to increase for younger ages followed by a decrease in older ages. In contrast, electrically evoked neuronal activity increased with the age and did not show any decline up to the oldest age (Day 7 worms) tested in our experiments. We envision the use of the microfluidic platform as a generic tool for obtaining repeatable and accurate functional imaging data from a large population of worms in studies where neuronal stimulation and monitoring is desired.

7.1.3 Hardware-based emulation of *C. elegans* neuronal functionality

Hardware based emulation of the nervous system has long been proposed as a computational platform for real-time simulation and investigation of the different computational paradigms used by the nervous system to generate specific behaviors in an organism. We believe that such a platform would assist neurobiologists in making inferences about the neuronal origins of the wide repertoire of behavioral patterns displayed by the worm. Developing such a computational platform for *C. elegans* nervous system is a feasible goal because : a) it has a simple nervous system (302 neurons with approximately 7000 synapses), and b) there exists a complete description of the morphology and synaptic connectivity of its entire nervous system [130]. As a step towards this goal, we presented an analog circuit for emulating the functionality of the ASH chemosensory neuron in *C. elegans*. We should highlight that, this is the same neuron from which we previously recorded calcium transients in response to a chemical and electrical stimulus. The analog circuit was designed to implement a first-order differential equation model of the stimulus-evoked calcium transients in the ASH neuron.

We simulated this circuit in cadence as well as built it on a breadboard. The transient response of this circuit to a step input was qualitatively similar to the experimentally obtained calcium transients in the ASH neuron.

7.2 Future Work

We envision the work demonstrated in this thesis to take the following future research directions:

7.2.1 Microfluidic platform for screening anti-aging drugs

We envision the development of a calcium imaging based microfluidic platform for high-throughput screening of drug compounds with anti-neurodegeneration effects. Neurodegenerative diseases (such as Parkinsons, Alzheimer, Dementia, etc) are highly correlated with the aging of nervous system. As a result, screening technologies that can efficiently and rapidly identify compounds with anti-aging effects are much needed for the development of anti-neurodegenerative compounds. From a pharmaceutical standpoint, the drug discovery process consists of high-throughput *in vitro* screening assays, typically performed in cell cultures. This process is particularly challenging for the discovery of anti-neurodegenerative compounds as the in vitro assays fail to represent the accumulative effects of aging. To circumvent this problem, the use of model organisms such as *C. elegans*, in *in-vivo* assays is considered to be a potential candidate for the discovery of anti-aging compounds [137]. *C. elegans* with a lifespan of 2-3 weeks [12], has revealed several genes that are known to be involved in aging [83]. They however pose a challenge as a model organism - due to their small size, manipulating

them is skill intensive and requires extensive manual labor resulting in low throughput. Further, there also lacks a robust assay for measuring the aging of *C. elegans* nervous system.

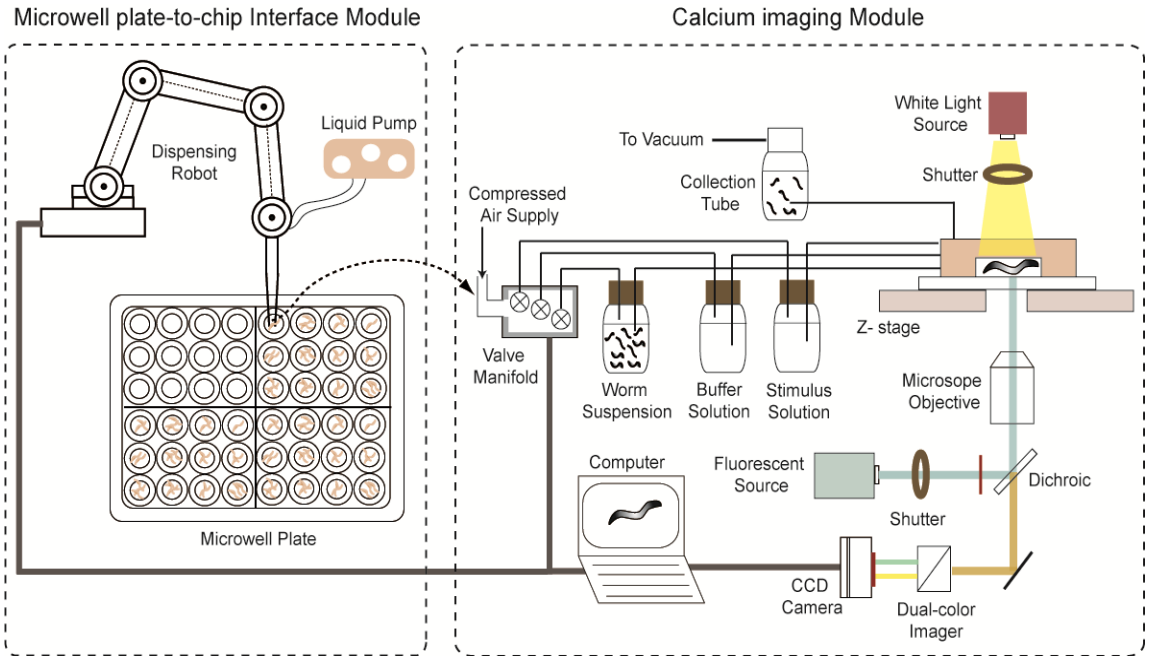

Figure 7.1: A high-throughput platform for screening anti-aging drugs. A robotic arm and a well plate of chemical compounds to be tested (shown on left) are interfaced with the calcium imaging module (shown on right) described in chapter 4.

Here, we propose to utilize the age-dependant stimulus evoked neuronal response in *C. elegans* to perform high-throughput screening of anti-aging compounds. To do so, the calcium imaging microfluidic platform described in chapter 4, can be interfaced with a robotic arm and a well-plate of chemical compounds to be screened (**Figure 7.1**). *C. elegans* can be grown in the various test compounds in the well-plate and automatically transported into the microfluidic device by the robotic arm. The anti-aging effect of a particular chemical compound can then be tested by measuring the stimulus evoked calcium transients in drug treated worms and comparing them with the non-treated

worms. The use of such a platform is not only limited to the screening of anti-aging compounds, but can also be used to identify longevity genes as well as assess the effect of environmental factors on aging.

7.2.2 Investigating neuronal networks *in vivo* in *C. elegans* using Direct Current Electric Stimulation

We envision the combination of calcium/microfluidic imaging and direct electric current stimulation as a unique approach to study neuronal networks in *C. elegans*. The ease with which, an electrical stimulus can be precisely controlled in terms of delivery, strength and spatial location, makes it a powerful tool to probe into the physiology of the nervous system of *C. elegans*. In this thesis, we showed for the first time, that electric currents can be used to locally induce neuronal activation (both depolarization as well as hyperpolarization). Furthermore, we believe that unlike electric fields, direct electric current can be used to activate any neuron in the worm's body. Thus, by utilizing novel multi-electrode designs that span the entire body of the worm, it might be possible to selectively activate a particular neuron and study its signal flow path. Such a technique would enable to study *in vivo* the functional connectivity in the *C. elegans* nervous system.

APPENDICES

Appendix A

Fabrication Process Flow Of The Microfluidic Devices

A.1 Fabrication process flow of the microfluidic device presented in Chapter 4

This device facilitated imaging the activity of the worm's olfactory neurons in response to a fluid-borne chemical stimulus delivered to the worm's nose. The fabrication process flow for this device is divided into two modules, a) fabricating the photoresist mold and b) fabricating the PDMS microfludic chip, as explained below.

a) Fabricating the photoresist mold – This mold consists of two layers which are lithographically made using the SU-8 photoresist. Both layers have a similar fabrication process flow as outlined below :

Step 1 : Wafer dehydration

Dehydrate the silicon wafer on a hotplate at 180° C for approximately 10 minutes.

Step 2 : Spin the photoresist

The type of SU-8 photoresist to be spun depends on the layer thickness to be fabricated. We recommend SU-8 2007 for thicknesses between 7-15 µm, SU-8 2015 for 15-42 µm and SU-8 2050 for 50-120 µm. Spin the photoresist on the silicon wafer for 5 sec @ 500 rpm and for 30 sec @ 'T' rpm. The spin speed 'T' used to achieve the desired SU-8 layer thickness is selected from **Figure A.1**.

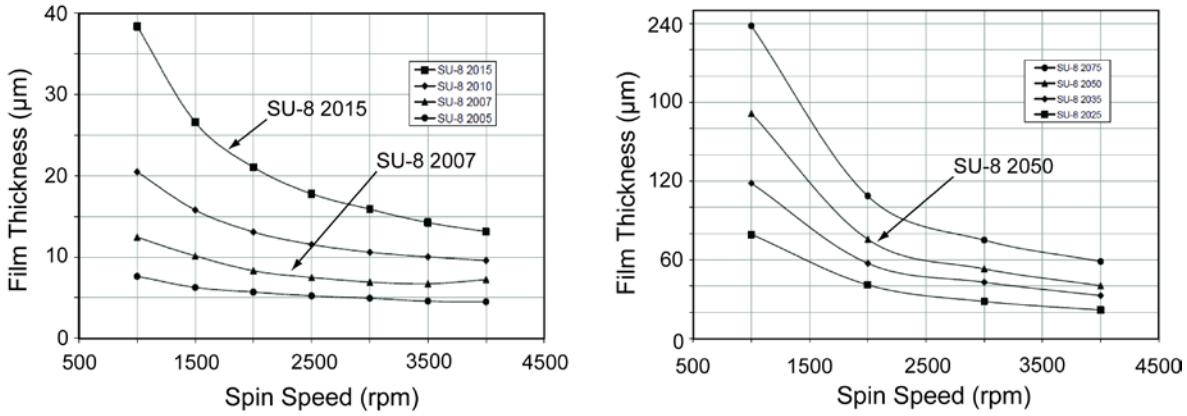

Figure A.1 : Film thickness vs Spin speed chart for SU-8 2007, SU-8 2015 (left) and SU-8 2050 (right). [adapted from microchem website : www.microchem.com].

Step 3 : Soft bake

Soft bake the wafer for 'SB1' min @ 65° C and 'SB2' min @ 95° C. The bake times 'SB1' and 'SB2' used for the different SU-8 layer thicknesses are listed in **Table A.1**.

SU-8 Type	Film Thickness (µm)	Soft Bake Time (min)	
		@65° C SB1 (min)	@95° C SB2 (min)
SU-8 2007	7 - 15	1	2 - 3
SU-8 2015	16 – 30	1	3 – 4
	31 - 42	2	5 – 7
SU-8 2050	50 - 60	2 - 3	10 - 15

Table A.1 : Soft bake time vs Film thickness.

Step 4 : UV exposure

Expose the wafer to UV and deliver the appropriate amount energy based on the film thickness. The dosage energy recommended for different SU-8 layer thicknesses is listed in **Table A.2**.

SU-8 Type	Film Thickness (µm)	Dosage Energy (mJ / cm^2)
SU-8 2007	7 - 15	110 - 140
SU-8 2015	16 – 30	140 - 150
	31 - 42	150 - 160
SU-8 2050	50 - 60	150 - 200

Table A.2 : Dosage energy vs Film thickness.

Step 5 : Post-expose bake

Bake the wafer on a hotplate for 'PB1' min @ 65° C and for 'PB2' min @ 95° C. The post-exposure bake time 'PB' used for the different SU-8 layer thicknesses is listed in **Table A.3**.

SU-8 Type	Film Thickness (µm)	Post-expose Bake Time (min)	
		@65° C PB1 (min)	@95° C PB2 (min)
SU-8 2007	7 - 15	1	3 - 4
SU-8 2015	16 – 30	1	4 - 5
	31 - 42	1	5 - 6
SU-8 2050	50 - 60	1 - 2	6 - 7

Table A.3 : Post-expose bake time vs Film thickness.

Step 6 : Develop

Develop the wafer using 'SU-8 Developer' for approximately 15 minutes. Rinse the wafer with iso-propanol and dry it using a N_2 gun. Repeat this process until the unexposed SU-8 is completely removed off the wafer.

Step 7 : Hard bake

Bake the wafer on a hotplate for 10 min @ 180° C.

It should be noted that fabricating additional SU-8 layers, subsequent to layer 1, require alignment and thus need an extra processing step in addition to the steps listed above. This step is executed after spinning the photoresist and includes the removal of the photoresist that covers the alignment marks patterned in layer 1. The alignment marks are exposed by removing the photoresist using acetone with the help of a cotton swab.

b) Fabricating the PDMS microfluidic chip

Step 1 : Silanize the SU-8 mold

Place the SU-8 mold in a vacuum chamber along with a small quantity of a silanizing agent such as Trimethylchlorosilane (TMCS). Silanize the mold for approximately 30 minutes.

Step 2 : Mix PDMS with curing agent

Take 80 g PDMS and mix it with the curing agent in the ratio 10:1, i.e. one gram of curing agent for every 10 g of PDMS. We refer this mixture as “PDMS mixture” in the following steps.

Step 3 : Pour the PDMS mixture onto the SU-8 mold

Place the mold in a petri dish and fix it using a scotch tape. Apply scotch tapes around the entire circumference of the silicon wafer. This helps in preventing PDMS from going underneath the wafer. Next, pour the PDMS mixture onto the SU-8 mold.

Step 4 : Degas the PDMS mixture that was poured on the mold

Place the petri dish containing the mold in a vacuum chamber until all the air bubbles have been removed. It should be emphasized that, air bubbles that settle near sharp features on the mold might not get easily removed using vacuum. Manually remove these bubbles using a sharp 25 gauge needle.

Step 5 : Cure the PDMS mixture

Place the petri dish in an oven at 65° C for approximately 2 hrs. Peel the hardened PDMS off the mold and divide it into individual chips using a sharp blade.

Step 6 : Drill holes inside the PDMS chips

All holes but the one that corresponds to the worm inlet, are drilled using 0.75 mm I.D. hole puncher (Z708798 Harris Uni-Core from sigma-aldrich). The worm inlet is drilled using a 2 mm I.D. hole puncher (Z708844 Harris Uni-Core from sigma-aldrich).

Step 7 : Cleaning the holes

Drilling holes inside PDMS generates a significant amount of scrap that can easily clog the microfluidic channels. To clean this scrap, rub the inside surface of the hole with a 25 gauge needle (Needle only 25 Gauge 1.5 inch from Becton-Dickinson) and remove the PDMS particles that are stuck on the inside surface.

Step 8 : Cleaning the hole corresponding to the worm inlet

It is very critical to have the worm inlet absolutely clean. To do so, take a 25 gauge needle and dip its tip into a very small quantity of PDMS mixture. Now, use this needle to coat the inside surface of the hole with the PDMS mixture and then place in the oven at 65° C for approximately 15-30 minutes.

Step 9 : Bonding the PDMS chip to a glass slide

The PDMS chip is plasma bonded to a microscope glass coverslip using air plasma (Plasma Prep II ; SPI supplies) at 50 W and 250 mTorr for 35 s. To make the plasma bond strong, the chip is placed in the oven at 65 for 10 minutes.

A.2 Fabrication process flow of the microfluidic device presented in Chapter 5.

This device facilitated imaging the activity of the worm's olfactory neurons in response to an electric current stimulus. The fabrication process flow for this device is divided into three modules, a) fabricating ITO (Indium Titanium Oxide) electrodes on a glass slide, b) fabricating the photoresist mold and c) fabricating the PDMS microfludic chip, as explained below.

a) Fabricating ITO electrodes on a glass slide

Step 1 : Sample preparation

Rinse the glass slide in iso-propanol and dry it using N_2 gun.

Step 2 : ITO (Indium Titanium Oxide) deposition

Deposit 1500 Å thick ITO using the Ener-Jet Sputter.

Step 3 : Spin HMDS

Spin the adhesion promoter HMDS for 5 sec @ 500 rpm and for 15 sec @ 3000 rpm

Step 4 : Spin photoresist to a thickness of 2-3 µm

Spin photoresist S1827 for 5 sec @ 500 rpm and for 30 sec @ 5000 rpm

Step 5 : Soft bake

Bake the glass slide on hotplate for 1 minute at 115 °C.

Step 6 : UV exposure

Expose the glass slide to UV via the appropriate mask using the 'hard contact' mode exposure. Expose the photoresist for approximately 6 sec.

Step 7 : Develop the photoresist

Develop the photoresist using MF319 for approximately 2 min. Rinse the glass slide with DI water and dry it with N_2 gun.

Step 8 : Pattern the ITO

Place the glass slide in a solution of HCL:H_2O mixed in the ratio 1:1 for approximately 1 min 30 sec. Rinse the slide with DI H_2O and dry it with N_2 gun.

Step 9 : Remove the photoresist

Place the slide in acetone for approximately 3 min. Rinse it with iso-propanol and finally dry it with N_2 gun.

b) Fabricating the photoresist mold

This mold consists of three layers which are lithographically made using the SU-8 photoresist. These layers are fabricated using the process flow listed in **A.1 (a).**

c) Fabricating the PDMS microfluidic chip

The PDMS chip is fabricated using the process flow listed in **A.1 (b)**. Here, in the final step, the PDMS chip is bonded to the ITO coated glass slide fabricated in **A.2 (a)**. It should be noted that, ITO does not form a strong bond with PDMS. And thus, to prevent any leakage via the ITO electrodes, an epoxy glue (5 Minute Epoxy from Ace Hardware)

is applied to edges of the PDMS chip. To provide electrical access to the ITO electrodes, wires are bonded to it using silver conductive epoxy (8331-14G from mgchemicals).

Appendix B

Experimental Protocol For The Setup Of The Calcium Imaging Microfluidic Platform

Here, we describe the experimental protocol for acquiring chemical stimulus-evoked calcium transients from the olfactory neurons in *C. elegans*, using the automated microfluidic platform presented in Chapter 4.

B.1 Microfluidic chip interface setup protocol

Index	Part Nos.	Part Description	Company
1	NA	Microfluidic Chip	NA
2	14-170-11B	Polyethylene tubing I.D. = 0.023’’ O.D. = 0.038’’	fishersci
3	BB521-63	Polyurethane tubing I.D. = 0.063’’ O.D. = 0.125’’	scicominc
4	14-817-33	20 cc syringes with luer lock tip	fishersci
5	P35503	Support stand	labdepotinc
6	64-0147	Base mount for syringe holder system	labdepotinc
7	64-0153	Add-on bracket for syringe holder system	labdepotinc
8	731-8221	0.8 mm barb to female luer	bio-rad
9	731-8224	0.8 mm barb to male luer	bio-rad
10	732-8300	0.8 mm barb to barb connector	bio-rad

11	732-8102	2-way stopcock	bio-rad
12	4650	Sterile acrodisc syringe filters	Pall
13	75165A684	Dispensing needles	mcmaster
14	VG-065-00-00	Multi-stage vacuum generator. (These pumps operate using a compressed air supply. So make sure that you have a compressed air pressure supply with an output of atleast 60 psi).	Gastmfg
15	LFAA1201610H	Solenoid valves	Theleeco

Table B.1: Materials required for the microfluidic chip interface setup.

Step 1

Insert polyethylene tubing (item 2) into the holes drilled inside the microfluidic chip. Insert these tubing pieces into all the holes, except the hole that corresponds to the worm inlet.

Step 2

Connect the hole corresponding to the worm inlet channel to a polyethylene tubing (item 3) via barb connector (item 10) and then place the microfluidic chip on the z-stage of an inverted microscope.

Step 3

Connect the chip outlet to a vacuum source (item 14) and then turn on the vacuum.

Step 4

Take a set of five 24 mL syringes (item 4) and place them on a support stand (item 5,6,7). Fill 4 of them with a buffer solution (S. Basal) and 1 with a solution of the chemical stimulus.

Step 5

Connect the syringes to the respective tubings on the microfluidic device. The setup at this point should look as that shown in **Figure B.1**.

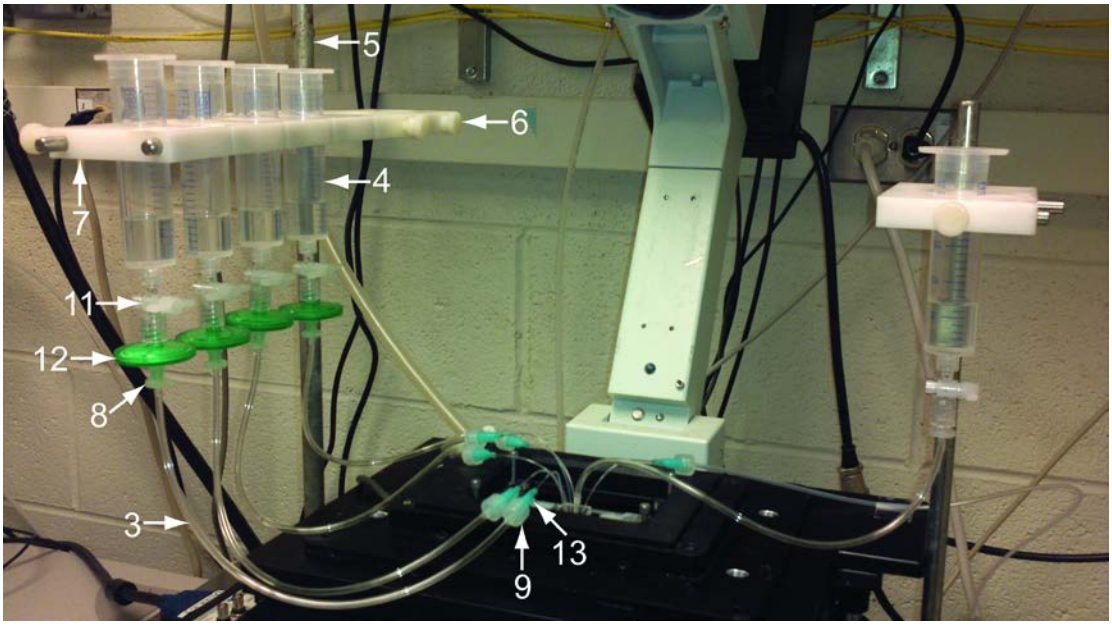

Figure B.1 : Snapshot of the setup showing the fluidic connections between the syringes and the microfluidic chip. The materials shown in this snapshot are referred by their index numbers shown in Table B.1.

B.2 Hardware interface setup protocol

Index	Part Nos.	Part Description	Company
1	IX71	Inverted fluorescence microscope	Olympus
2	QUANTEM:512SC	CCD Camera	Photometrics

3	DV^2	Dual color imager equipped with Dichroic : 505dcxr Filter 1 : 470/30 nm Filter 2 : 535/30 nm	MAG Biosystems
4	BNC-2110	DAQ card	National Instruments
5	NZ100CE	Piezo z-stage and its controller	Prior scientific
6	Lambda SC	Shutter and its controller (used as a fluorescence shutter)	Sutter Instrument
7	SH05	Beam shutter (used as a white light shutter)	Thorlabs
8	SC10	Beam shutter controller	Thorlabs
9	2N3904	NPN transistor	Digikey
10	E3631A	Power supply	Agilent
11	1241-3	Holed rubber stopper	Sciencestuff
12	PMG-60	Micro gauge 0-60 psi	pneumadyne
13	R-800-60-W/K	Regulator (60 psi)	airtrolinc
14	732-8302	0.8mm barb T connector	bio-rad
15	LFAA1201610H	Solenoid valves	theleeco
16	731-8224	0.8 mm barb to male luer	bio-rad

Table B.2: Materials required for the hardware interface setup.

Step 1

Equip the inverted microscope with a z-stage (item 5), dual color imager (item 3), CCD camera (item 2), white light shutter (item 7) and fluorescence shutter (item 6), as illustrated in **Figure B.2**.

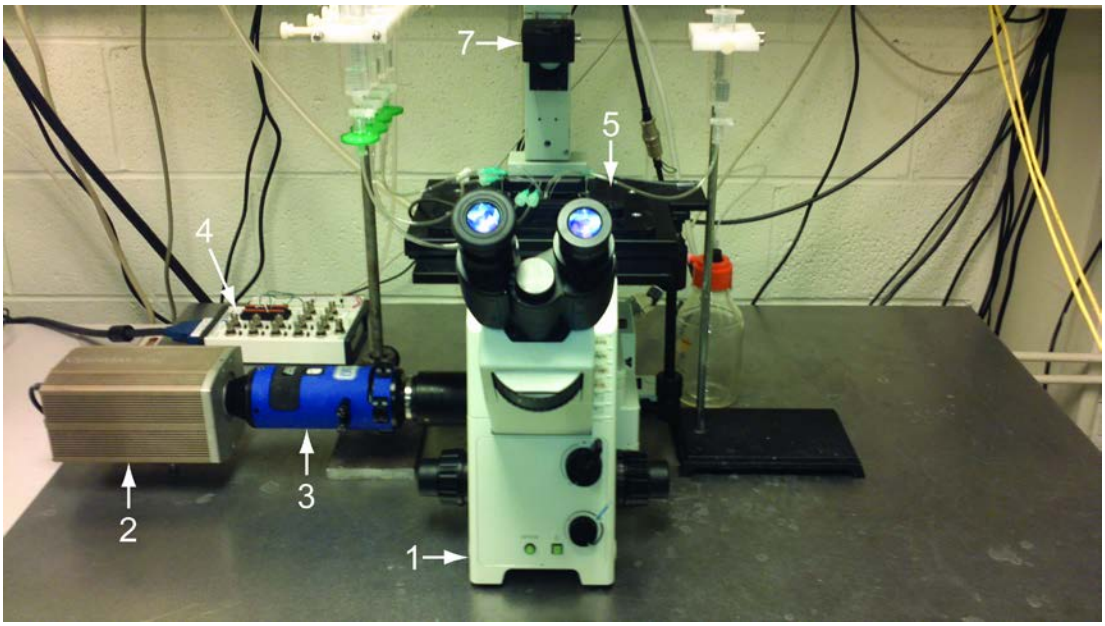

Figure B.2 : Snapshot of the setup showing the inverted microscope equipped with a camera, dual color imager and light shutters. All the hardware is controlled by a DAQ card (also shown in the setup). The various hardware devices shown in this snapshot are referred by their index numbers shown in Table B.2.

Step 2

Connect the 20 cc syringes that are already connected to the worm inlet channel and the side channel of the microfluidic chip, to an air pressure source via a pressure regulator (item 13) and a valve (item 15 in Table B.1) as shown in **Figure B.3**.

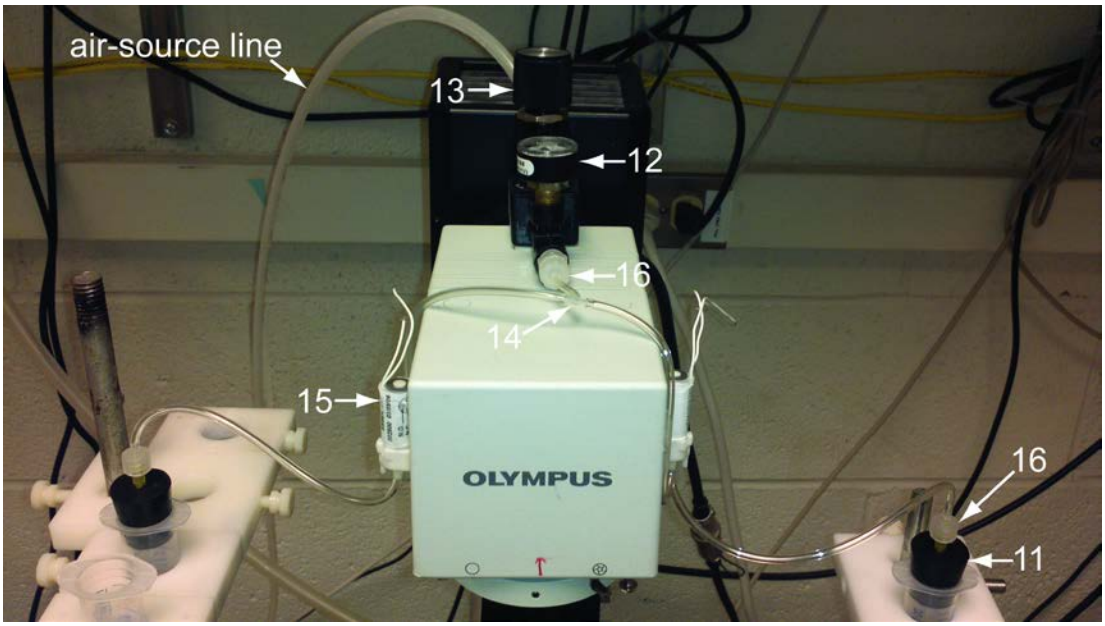

Figure B.3 : Snapshot of the setup showing the fluidic connections between the air pressure source and the 20 cc syringes. The materials shown in this snapshot are referred by their index numbers shown in Table B.2.

Note that, at this point there are a total of 3 valves connected in the system. In the subsequent steps we shall refer these valves as shown below :

Nos.	**Valve connection**	**Acronym**
1	Connected to the side channel.	ScV
2	Connected to the chip inlet.	InV
3	Connected to the microfluidic channels that steer the stimulus over the worm's nose.	StV

Table B.3 : Acronyms defined for the different valves used in the setup.

Step 3

Connect the valves and the various controllers (i.e. z-stage and shutter controllers) to the DAQ card as shown in **Figure B.4.**

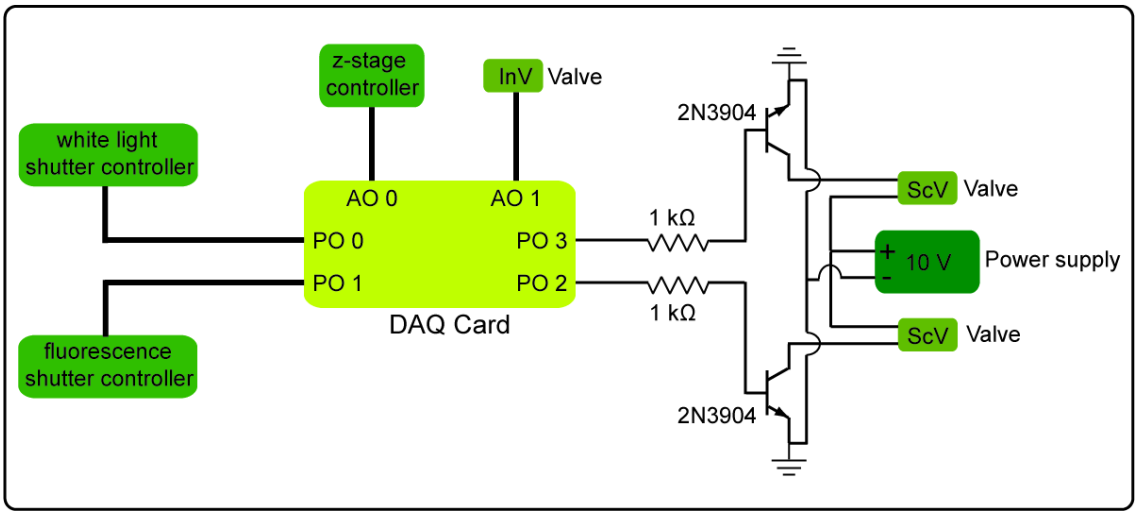

Figure B.4 : Wiring diagram for connecting the DAQ card (item 4 in Table B.2) to the z-stage and shutter controllers (items 5-7 in Table B.2) and the valves (item 15 in Table B.1).

B.3 Software interface setup protocol

Index	Part Nos.	Part Description	Company
1	LabVIEW 8.5	LabVIEW	National Instruments
2	SITK	LabVIEW driver for the QUANTEM:512SC CCD camera	R cubed software

Table B.4 : Softwares/drivers required for the software interface setup.

The software interface is implemented in LabVIEW (version 8.5). The front panel of this software is shown in **Figure B.5.** Follow the steps outlined below to acquire stimulus-evoked calcium imaging data from the ASH neuron.

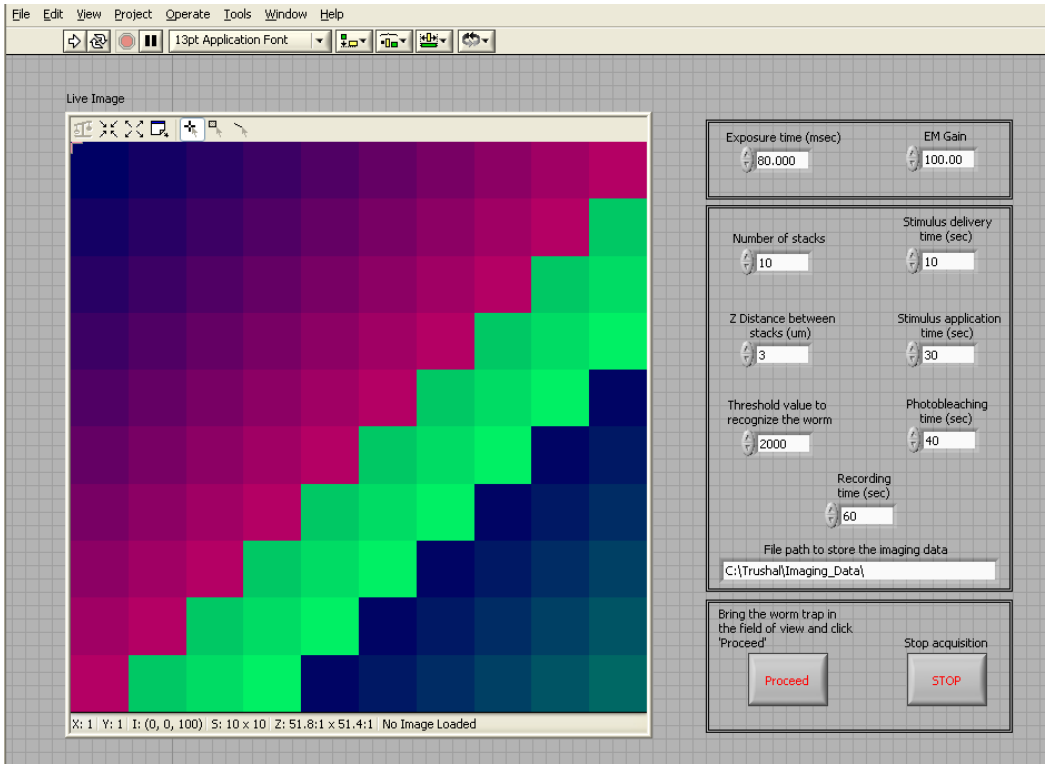

Figure B.5 : Snapshot of the front panel of the LabVIEW program built for the automated acquisition of calcium imaging data. The left half of this panel shows the Live Image of the microfluidic chip and the right half shows the various tabs for User Defined Inputs.

Step 1

Specify the values of the parameters that are displayed on the top-right section in the front panel window. These parameters include :

a.) Exposure time : This refers to the exposure time that the CCD camera would use while capturing images. Recommended value = 80 ms.

b.) EM Gain : This refers to electron multiplier gain of the CCD camera. Recommended value = 100.

c.) Number of stacks : This refers to the total number of z-stacks that will be acquired in order to find the focal plane of the neuron. Recommended value = 10.

d.) Z distance between stacks : This refers to the distance that the z-stage would move each time for acquiring an image stack in order to find the focal plane of the neuron. Recommended value = 3 μm.

e.) Stimulus delivery time : This refers to the amount of time that the program would wait before delivering the stimulus. The value depends on the experiment.

f.) Stimulus application time : This refers to the amount of time the stimulus will be present. The value depends on the experiment.

g.) Photobleaching time : This refers to the amount of time the neuron will be photobleached. Recommended value = 40 to 60. This value depends on the age of the worm.

h.) Recording time : This refers to the amount of time the calcium imaging data would be recorded. The value depends on the experiment.

i.) File path : This refers to the path of the folder where the program stores all the calcium imaging data.

Step 2

Click the ‘RUN’ button in the front panel window.

Step 3

Bring the worm trap channel into the field of view and then click ‘Proceed’.

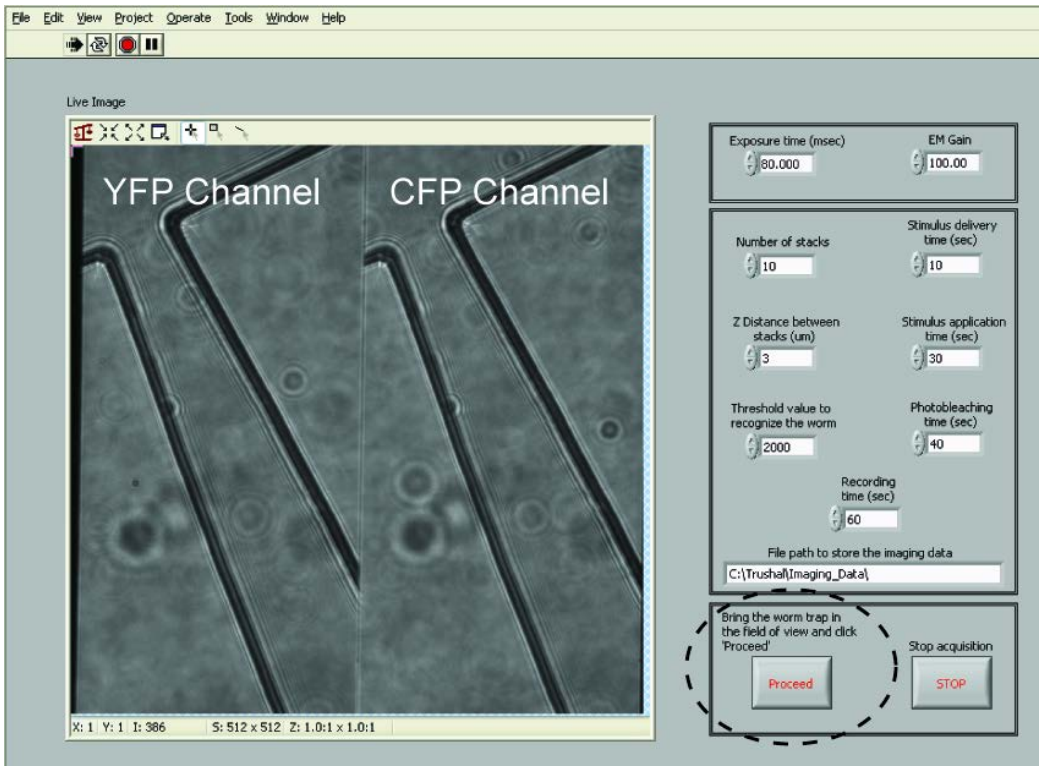

Figure B.6 : Illustration of Step 3. The 'Proceed' button is highlighted by the dashed circle.

Step 4

An image of the worm trap will be displayed. Draw a rectangular region in the YFP channel of the image, such that it does not enclose the worm trap channel. The program utilizes this region to calculate the background light intensity. Click OK.

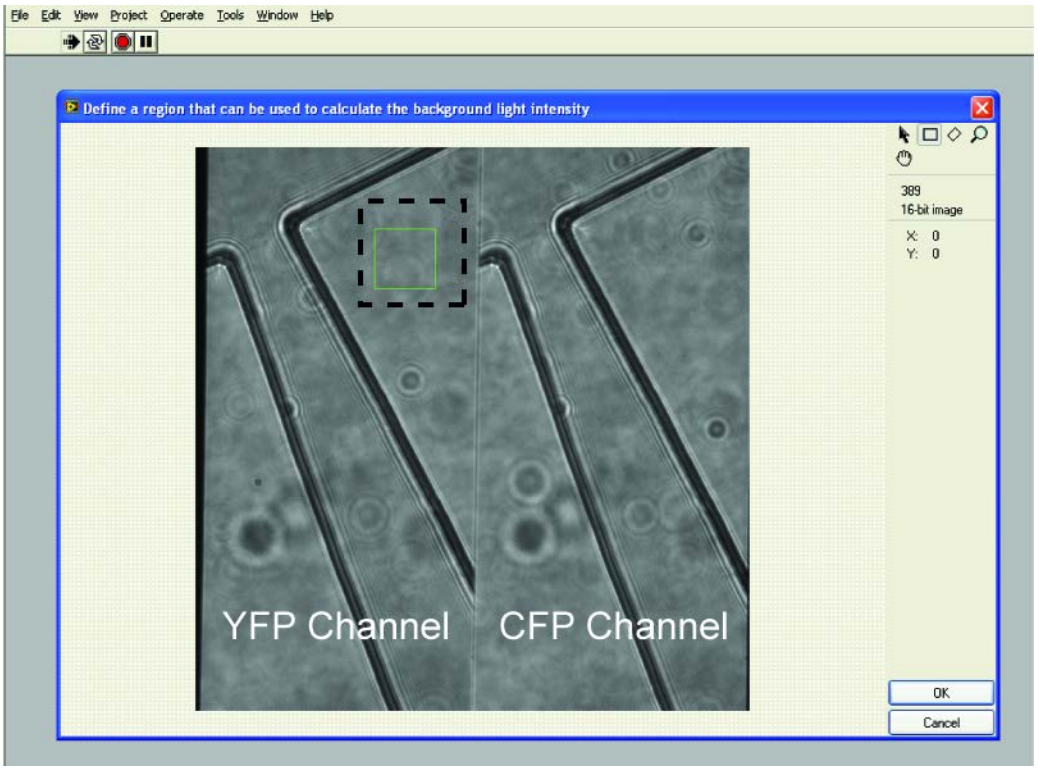

Figure B.7 : Illustration of Step 4. The dashed rectangle shows the region of interest.

Step 5

An image of the worm trap will be displayed once more. Draw a rectangular region in the YFP channel of the image, such that it encloses the end of the worm trap. The program utilizes this region to search for the ASH neuron. Click OK.

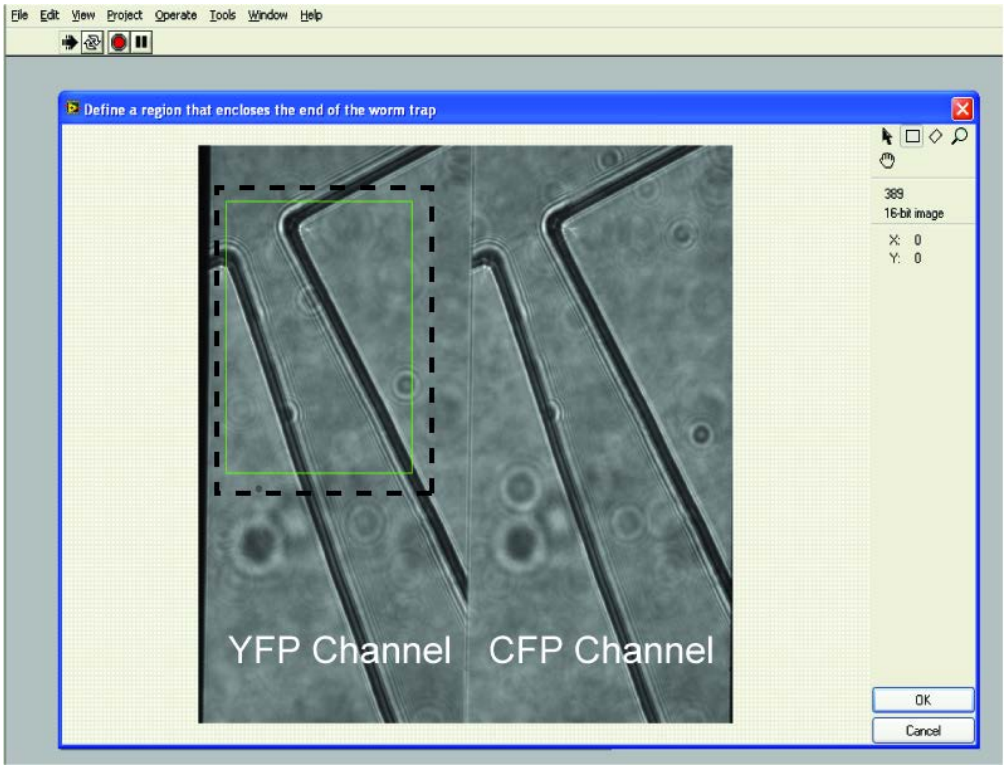

Figure B.8 : Illustration of Step 5. The dashed rectangle shows the region of interest.

Step 6

An image of the worm trap will be displayed again. Draw a rectangular region in the YFP channel of the image, such that it encloses the beginning of the worm trap. The program utilizes this region to monitor's the worm's entry into the trap. Click OK.

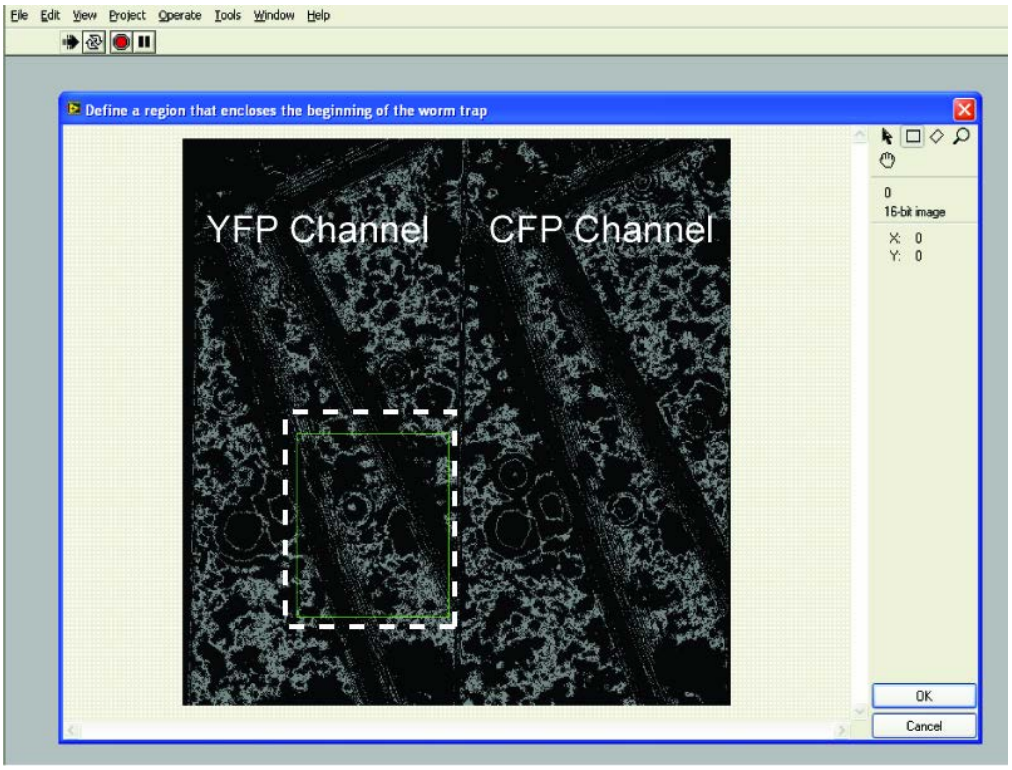

Figure B.9 : Illustration of Step 6. The rectangular region is highlighted by the dashed rectangle. The image of the worm-trap shown in this step would be a thresholded version of the original image.

The LabVIEW software records and stores the calcium imaging data for individual worms in a folder defined by the user in step 1. This data is stored as a stack of images in the '.tif' format.

B.4 FRET ratio extraction protocol

We implemented an image tracking software in LabVIEW for extracting the FRET ratio transient from the recorded calcium imaging data. The front panel of this software is shown in **Figure B.10**. Follow the steps outlined below to extract the FRET ratio from individual recordings.

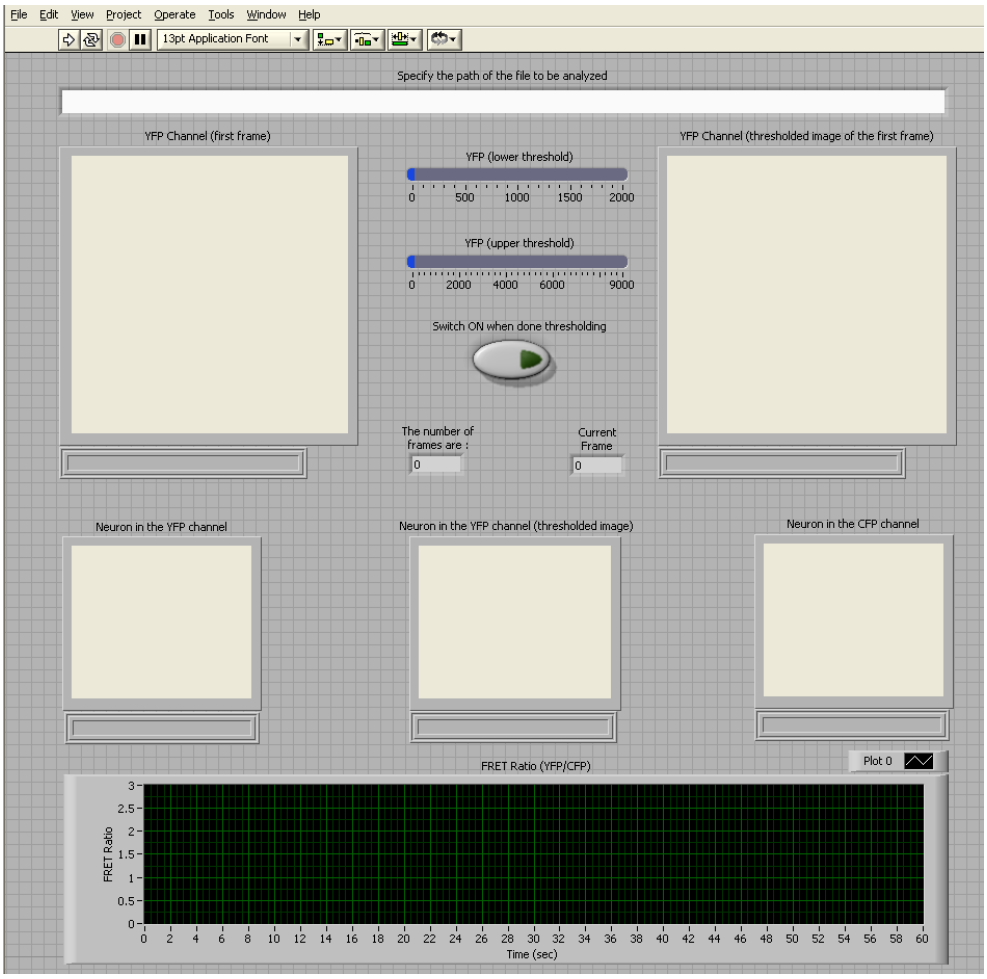

Figure B.10 : Snapshot of the front panel of the LabVIEW program built for extracting the FRET ratio transient from the recorded calcium imaging data.

Step 1

Enter the path of the '.tif' file to be analyzed.

Step 2

Click the 'RUN' button in the front panel window.

Step 3

A fluorescent image of the worm will be displayed. Define a rectangular region in the YFP channel of the image, that can be used to calculate the background intensity. Click OK.

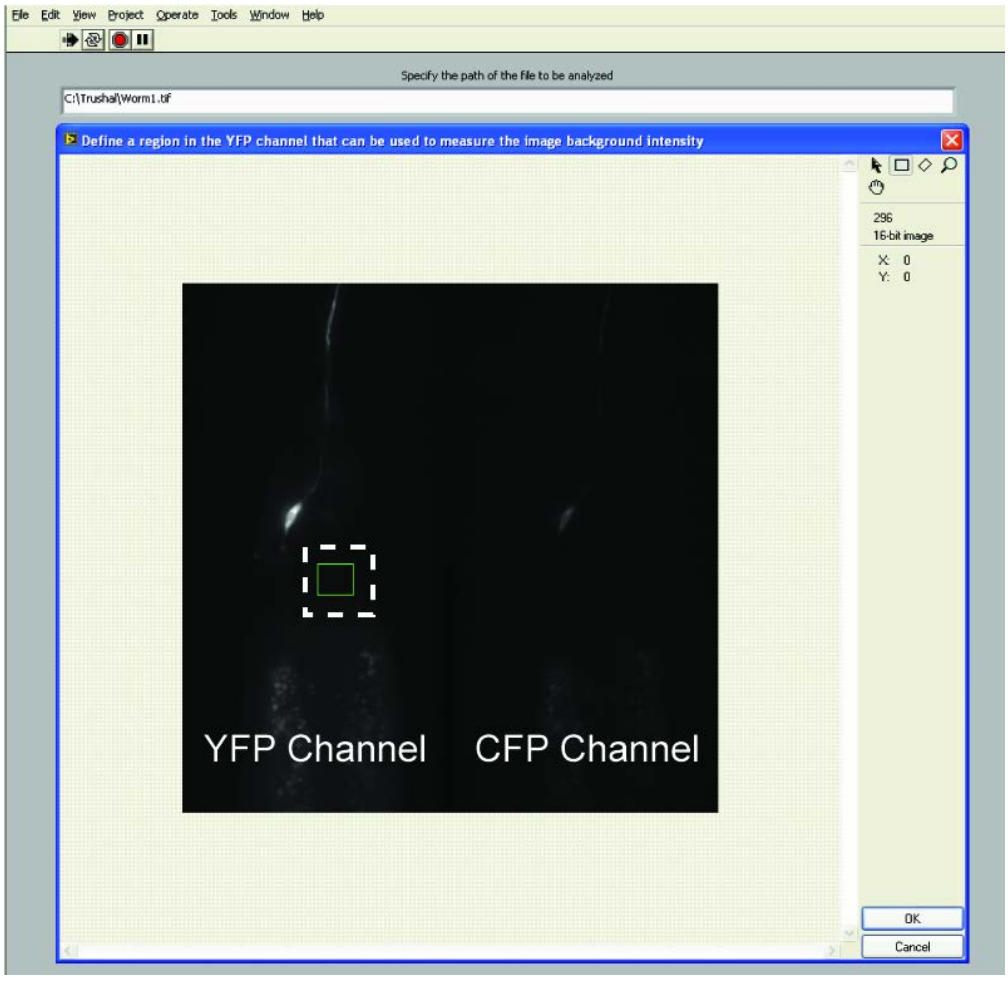

Figure B.11 : Illustration of Step 3. The rectangular region is highlighted by the dashed rectangle.

Step 4

The fluorescent image of the worm will be displayed again. Define a rectangular region that encloses the ASH neuron in the YFP channel of this image. The program tracks the ASH neuron as long as it remains within this rectangular region.

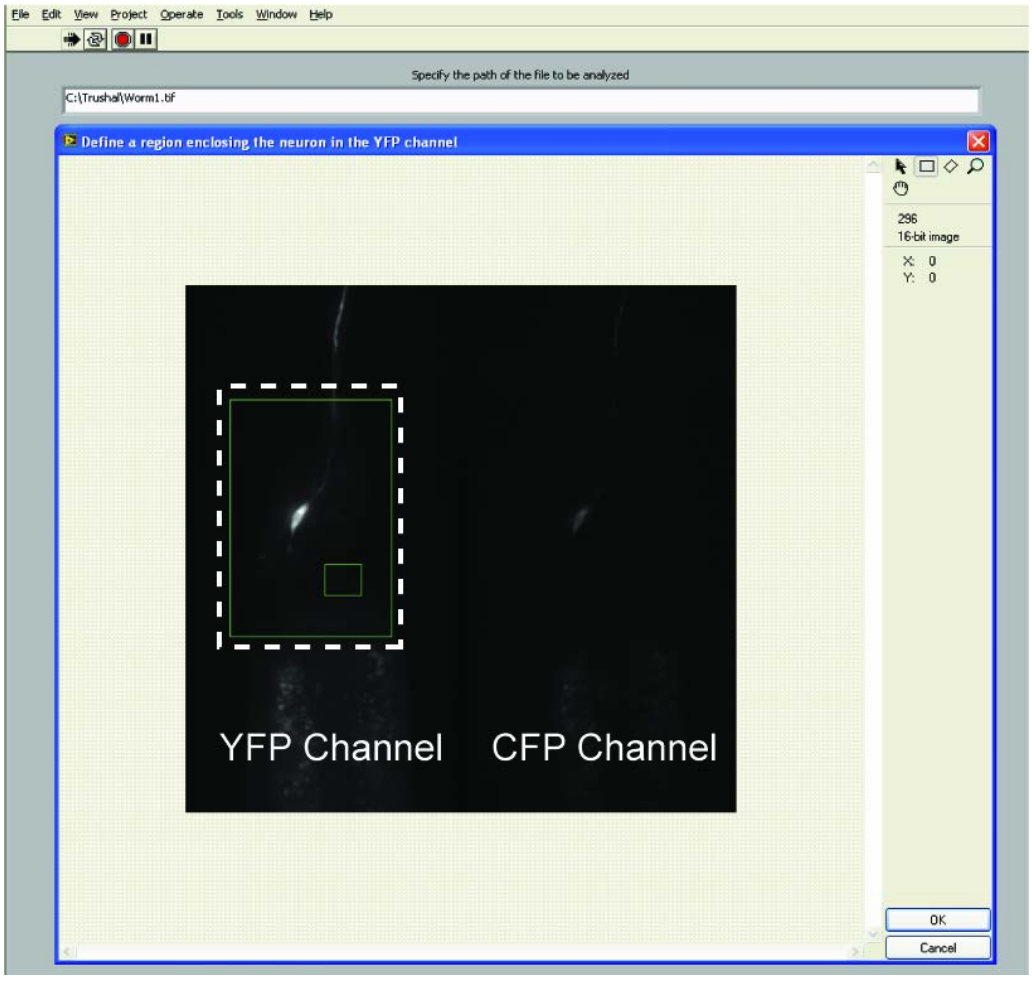

Figure B.12 : Illustration of Step 4. The rectangular region is highlighted by the dashed rectangle.

Step 5

Threshold the ASH neuron in the YFP channel using the ‘threshold intensity bar’ shown in the front panel.

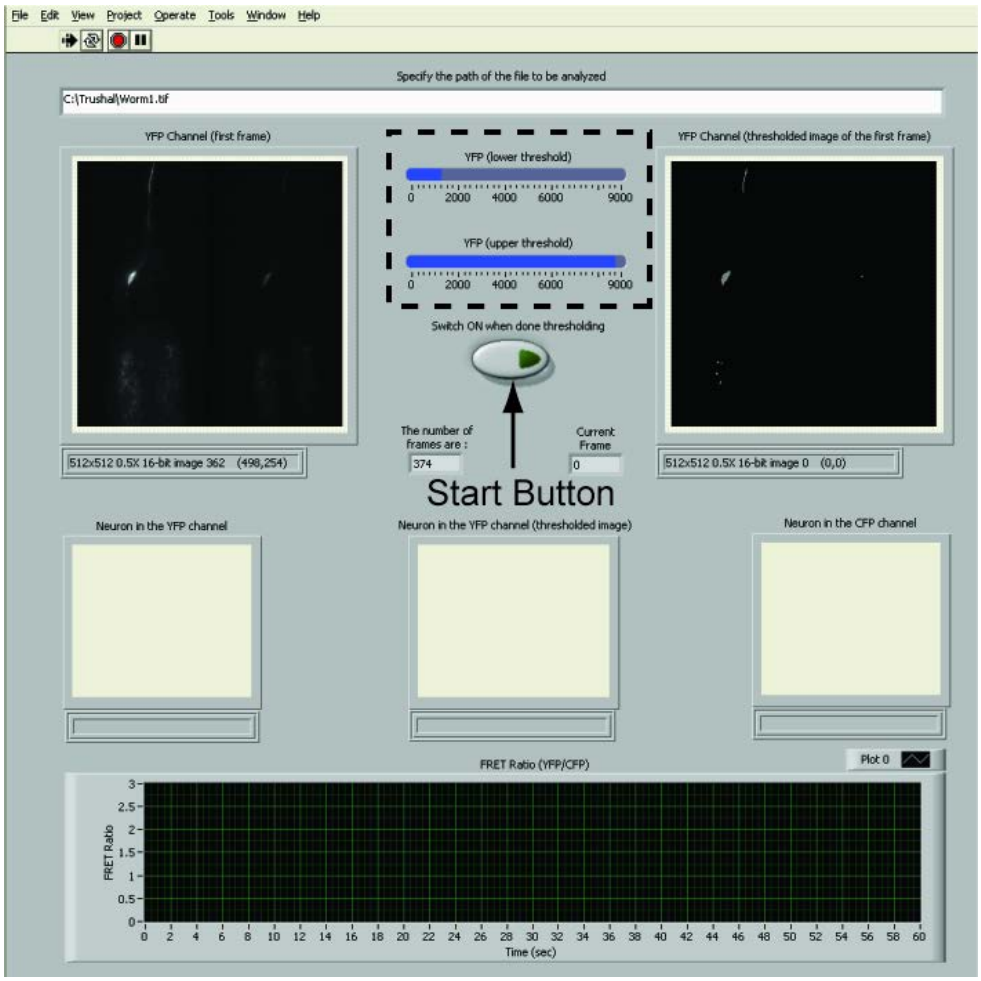

Figure B.13 : Illustration of Step 5. The 'threshold intensity bar' is highlighted by the dashed rectangle.

Step 6

Click the '**Start**' button in the front panel to start tracking.

B.5 FRET ratio processing protocol

The FRET ratios extracted in B.4 are further processed to eliminate the effect of photobleaching and calculate the percentage change in the FRET ratio as a function of time.

Step 1

Compile the FRET ratios for all the worms into a single excel file, such that each row corresponds to the FRET ratio transient from a single worm. Let this new file be referred as ‘FRET_Compilation’.

Step 2

Process the file ‘FRET_Compilation’ using the matlab code presented below. This code compensates for the photobleaching effects in the FRET ratio values and subsequently computes the FRET ratio as a percentage change from the baseline. The variable, ‘**r_abs**’ stores the absolute FRET ratio values and the variable, ‘**r_per**’, stores the values for the percentage change in the FRET ratio.

Matlab code for computing the FRET ratio trace :

```
clc
clear all
ratio = [];
A_ratio = [];
PBCurve = [];
ratio_absolute = [];
per_change = [];
ratio_abs_as = [];
per_change_as = [];
dir = ('C:\Users\TVC\Desktop\');
file_ratio = strcat(dir,'FRET_Compilation.xlsx');
A_ratio = xlsread(file_ratio);
dim = size(A_ratio);

for count = 1:dim(1,1)

ratio = A_ratio(count,:);
len = length(ratio);

% These are the values before stimulus was applied
ratio_bs = ratio(1:63);
```

```
% These are the values after stimulus was applied
ratio_as = ratio(64:len);


% Time points before stimulus was applied
t_bs = [0:0.08:(0.08*(63))];

% Time points after stimulus was applied
t_as = [0:0.08:0.08*(len-64-1)];

% Estimating the photobleaching curve before stimulus application
start_pt = ratio(1);
end_pt = ratio(63);
PBK1 = (log(end_pt./start_pt))./(t_bs(length(t_bs)));
PBCurve1 = start_pt.*exp((PBK1.*t_bs));

% Estimating the photobleaching curve after stimulus application
start_pt = sum(ratio(54:64))./11;
end_pt = sum(ratio(len-10:len))./11;
PBK2 = (log(end_pt./start_pt))./(t_as(length(t_as)));
PBCurve2 = start_pt.*exp((PBK2.*t_as));

% Net photobleaching curve
PBCurve(count,:) = [PBCurve1 PBCurve2];

% Estimating the photobleaching curve after stimulus application
r_abs(count,:) = (ratio - PBCurve(count,:));
r_per(count,:) = ((ratio_absolute(count,:))./(PBCurve(count,:))).*100;

end
```

BIBLIOGRAPHY

BIBLIOGRAPHY

1. Dougherty, K.J. and O. Kiehn, *Functional organization of V2a-related locomotor circuits in the rodent spinal cord.* Annals of the New York Academy of Sciences. 1198(1): p. 85-93.

2. Gammie, S.C., *Current Models and Future Directions for Understanding the Neural Circuitries of Maternal Behaviors in Rodents*. 2005. p. 119-135.

3. Friedrich, R.W., G.A. Jacobson, and P. Zhu, *Circuit Neuroscience in Zebrafish.* Current Biology. 20(8): p. R371-R381.

4. Nakamori, T., *Demonstration of a Neural Circuit Critical for Imprinting Behavior in Chicks.* The Journal of neuroscience. 30(12): p. 4467-4480.

5. Hyson, R.L., *The analysis of interaural time differences in the chick brain stem.* Physiology & Behavior, 2005. 86(3): p. 297-305.

6. Santiago-Medina, M., J.P. Myers, and T.M. Gomez, *Imaging adhesion and signaling dynamics in Xenopus laevis growth cones.* Developmental Neurobiology.

7. Sengupta, P. and A.D.T. Samuel, *Caenorhabditis elegans: a model system for systems neuroscience.* Current Opinion in Neurobiology, 2009. 19(6): p. 637-643.

8. Keene, A.C. and S. Waddell, *Drosophila olfactory memory: single genes to complex neural circuits.* Nat Rev Neurosci, 2007. 8(5): p. 341-354.

9. Angstadt, J.D. and A.O.W. Stretton, *Slow active potentials in ventral inhibitory motor neurons of the nematode Ascaris.* Journal of Comparative Physiology A: Neuroethology, Sensory, Neural, and Behavioral Physiology, 1989. 166(2): p. 165-177.

10. Stretton, A., et al., *Motor Behavior and Motor Nervous System Function in the Nematode Ascaris suum.* The Journal of Parasitology, 1992. 78(2): p. 206-214.

11. Williamson, R. and A. Chrachri, *Cephalopod Neural Network.* Neurosignals, 2004. 13: p. 87-98.

12. Riddle, D.L., *C. elegans II*. 1997, New York: Cold Spring Harbor Laboratory Press.

13. Schafer, W.R., *Neurophysiological methods in C. elegans: an introduction*, in *WormBook*, V. Ambros, Editor. 2006.

14. Richmond, J.E. and E.M. Jorgensen, *One GABA and two acetylcholine receptors function at the C. elegans neuromuscular junction.* Nat Neurosci, 1999. 2(9): p. 791-7.

15. Brockie, P.J., et al., *The C. elegans glutamate receptor subunit NMR-1 is required for slow NMDA-activated currents that regulate reversal frequency during locomotion.* Neuron, 2001. 31(4): p. 617-30.

16. Lee, R.Y., et al., *Mutations in the alpha1 subunit of an L-type voltage-activated Ca2+ channel cause myotonia in Caenorhabditis elegans.* EMBO J, 1997. 16(20): p. 6066-76.

17. O'Hagan, R., M. Chalfie, and M.B. Goodman, *The MEC-4 DEG/ENaC channel of Caenorhabditis elegans touch receptor neurons transduces mechanical signals.* Nat Neurosci, 2005. 8(1): p. 43-50.

18. Nakai, J., M. Ohkura, and K. Imoto, *A high signal-to-noise Ca(2+) probe composed of a single green fluorescent protein.* Nat Biotechnol, 2001. 19(2): p. 137-41.

19. Miyawaki, A., et al., *Fluorescent indicators for Ca2+ based on green fluorescent proteins and calmodulin.* Nature, 1997. 388(6645): p. 882-7.

20. Goodman, M.B., et al., *Active currents regulate sensitivity and dynamic range in C. elegans neurons.* Neuron, 1998. 20(4): p. 763-72.

21. Kerr, R., et al., *Optical imaging of calcium transients in neurons and pharyngeal muscle of C. elegans.* Neuron, 2000. 26(3): p. 583-94.

22. Lewis, J.A., et al., *The genetics of levamisole resistance in the nematode Caenorhabditis elegans.* Genetics, 1980. 95(4): p. 905-28.

23. Ryu, W.S. and A.D.T. Samuel, *Thermotaxis in Caenorhabditis elegans analyzed by measuring responses to defined thermal stimuli.* Journal of Neuroscience, 2002. 22(13): p. 5727-5733.

24. Chalfie, M. and J. Sulston, *Developmental genetics of the mechanosensory neurons of Caenorhabditis elegans.* Dev Biol, 1981. 82(2): p. 358-70.

25. Thorsen, T., S.J. Maerkl, and S.R. Quake, *Microfluidic large-scale integration.* Science, 2002. 298(5593): p. 580-4.

26. Chao, T.C. and A. Ros, *Microfluidic single-cell analysis of intracellular compounds.* Journal of the Royal Society Interface, 2008. 5: p. S139-S150.

27. Freed, L.E., et al., *Advanced tools for tissue engineering: scaffolds, bioreactors, and signaling.* Tissue Eng, 2006. 12(12): p. 3285-305.

28. Powers, M.J., et al., *A microfabricated array bioreactor for perfused 3D liver culture.* Biotechnol Bioeng, 2002. 78(3): p. 257-69.

29. Choi, N.W., et al., *Microfluidic scaffolds for tissue engineering.* Nature Materials, 2007. 6(11): p. 908-915.

30. Culotti, J.G. and R.L. Russell, *Osmotic avoidance defective mutants of the nematode Caenorhabditis Elegans.* Genetics, 1978. 90(2): p. 243-256.

31. Ward, S., *Chemotaxis by Nematode Caenorhabditis-Elegans - Identification of Attractants and Analysis of Response by Use of Mutants.* Proceedings of the National Academy of Sciences of the United States of America, 1973. 70(3): p. 817-821.

32. Sukul, N.C., *Influence of Potential Difference and Current on the Electrotaxis of Caenorhaditis elegans.* Journal of nematology, 1978. 10(4): p. 314.

33. Gabel, C.V., et al., *Neural Circuits Mediate Electrosensory Behavior in Caenorhabditis elegans*. 2007. p. 7586-7596.

34. Gray, J.M., et al., *Oxygen sensation and social feeding mediated by a C. elegans guanylate cyclase homologue.* Nature, 2004. 430(6997): p. 317-22.

35. Zhang, Y., H. Lu, and C.I. Bargmann, *Pathogenic bacteria induce aversive olfactory learning in Caenorhabditis elegans.* Nature, 2005. 438(7065): p. 179-84.

36. Qin, J. and A.R. Wheeler, *Maze exploration and learning in C. elegans.* Lab Chip, 2007. 7(2): p. 186-92.

37. Shi, W., et al., *Droplet-based microfluidic system for individual Caenorhabditis elegans assay.* Lab Chip, 2008. 8(9): p. 1432-5.

38. Luo, L., et al., *Olfactory behavior of swimming C. elegans analyzed by measuring motile responses to temporal variations of odorants.* Journal of neurophysiology, 2008. 99(5): p. 2617.

39. Hulme, S.E., et al., *Lifespan-on-a-chip: microfluidic chambers for performing lifelong observation of C. elegans.* Lab on a chip. 10(5): p. 589.

40. Lockery, S.R., et al., *Artificial dirt: microfluidic substrates for nematode neurobiology and behavior.* J Neurophysiol, 2008. 99(6): p. 3136-43.

41. Park, S.J., M.B. Goodman, and B.L. Pruitt, *Analysis of nematode mechanics by piezoresistive displacement clamp.* Proc Natl Acad Sci U S A, 2007. 104(44): p. 17376-81.

42. Doll, J.C., et al., *SU-8 force sensing pillar arrays for biological measurements.* Lab Chip, 2009. 9(10): p. 1449-54.

43. Rezai, P., et al., *Electrotaxis of Caenorhabditis elegans in a microfluidic environment.* Lab on a Chip. 10(2): p. 220-226.

44. Rezai, P., et al., *Behavior of Caenorhabditis elegans in alternating electric field and its application to their localization and control.* Applied physics letters. 96(15): p. 153702.

45. Chung, K., M.M. Crane, and H. Lu, *Automated on-chip rapid microscopy, phenotyping and sorting of C. elegans.* Nat Methods, 2008. 5(7): p. 637-43.

46. Crane, M.M., K. Chung, and H. Lu, *Computer-enhanced high-throughput genetic screens of C. elegans in a microfluidic system.* Lab Chip, 2009. 9(1): p. 38-40.

47. Hulme, S.E., et al., *A microfabricated array of clamps for immobilizing and imaging C. elegans.* Lab Chip, 2007. 7(11): p. 1515-23.

48. Rohde, C.B., et al., *Microfluidic system for on-chip high-throughput whole-animal sorting and screening at subcellular resolution.* Proceedings of the National Academy of Sciences of the United States of America, 2007. 104(35): p. 13891-13895.

49. Suzuki, H., et al., *In vivo imaging of C. elegans mechanosensory neurons demonstrates a specific role for the MEC-4 channel in the process of gentle touch sensation.* Neuron, 2003. 39(6): p. 1005-17.

50. Chronis, N., M. Zimmer, and C.I. Bargmann, *Microfluidics for in vivo imaging of neuronal and behavioral activity in Caenorhabditis elegans.* Nat Methods, 2007. 4(9): p. 727-31.

51. Chalasani, S.H., et al., *Dissecting a circuit for olfactory behaviour in Caenorhabditis elegans.* Nature, 2007. 450(7166): p. 63-70.

52. Zimmer, M., et al., *Neurons detect increases and decreases in oxygen levels using distinct guanylate cyclases.* Neuron, 2009. 61(6): p. 865-79.

53. Herndon, L.A., et al., *Stochastic and genetic factors influence tissue-specific decline in ageing C. elegans.* Nature, 2002. 419(6909): p. 808-14.

54. Emmons, S.W. and J. Lipton, *Genetic basis of male sexual behavior.* J Neurobiol, 2003. 54(1): p. 93-110.

55. Hobert, O. and H. Bulow, *Development and maintenance of neuronal architecture at the ventral midline of C. elegans.* Curr Opin Neurobiol, 2003. 13(1): p. 70-8.

56. Lettre, G. and M.O. Hengartner, *Developmental apoptosis in C. elegans: a complex CEDnario.* Nat Rev Mol Cell Biol, 2006. 7(2): p. 97-108.

57. Mori, I. and Y. Ohshima, *Neural regulation of thermotaxis in Caenorhabditis elegans.* Nature, 1995. 376(6538): p. 344-8.

58. Yanik, M.F., et al., *Neurosurgery: functional regeneration after laser axotomy.* Nature, 2004. 432(7019): p. 822.

59. Chung, S.H., et al., *The role of the AFD neuron in C. elegans thermotaxis analyzed using femtosecond laser ablation.* BMC Neurosci, 2006. 7: p. 30.

60. Hilliard, M.A., et al., *In vivo imaging of C. elegans ASH neurons: cellular response and adaptation to chemical repellents.* EMBO J, 2005. 24(1): p. 63-72.

61. Avery, L. and B.B. Shtonda, *Food transport in the C. elegans pharynx.* J Exp Biol, 2003. 206(Pt 14): p. 2441-57.

62. Nagy, A., et al., *Tailoring the genome: the power of genetic approaches.* Nat Genet, 2003. 33 Suppl: p. 276-84.

63. Guo, S.X., et al., *Femtosecond laser nanoaxotomy lab-on-a-chip for in vivo nerve regeneration studies.* Nat Methods, 2008. 5(6): p. 531-3.

64. Unger, M.A., et al., *Monolithic microfabricated valves and pumps by multilayer soft lithography.* Science, 2000. 288(5463): p. 113-6.

65. Whitesides, G.M., et al., *Soft lithography in biology and biochemistry.* Annu Rev Biomed Eng, 2001. 3: p. 335-73.

66. Nicolas, G. and D. Sillans, *Immediate and Latent Effects of Carbon-Dioxide on Insects.* Annual Review of Entomology, 1989. 34: p. 97-116.

67. Badre, N.H., M.E. Martin, and R.L. Cooper, *The physiological and behavioral effects of carbon dioxide on Drosophila melanogaster larvae.* Comparative Biochemistry and Physiology a-Molecular & Integrative Physiology, 2005. 140(3): p. 363-376.

68. Bretscher, A.J., K.E. Busch, and M. de Bono, *A carbon dioxide avoidance behavior is integrated with responses to ambient oxygen and food in Caenorhabditis elegans.* Proc Natl Acad Sci U S A, 2008. 105(23): p. 8044-9.

69. Hallem, E.A. and P.W. Sternberg, *Acute carbon dioxide avoidance in Caenorhabditis elegans.* Proc Natl Acad Sci U S A, 2008. 105(23): p. 8038-43.

70. Gray, J.M., J.J. Hill, and C.I. Bargmann, *A circuit for navigation in Caenorhabditis elegans.* Proc Natl Acad Sci U S A, 2005. 102(9): p. 3184-91.

71. Corbett, J.D., M.R. Cho, and D.E. Golan, *Deoxygenation affects fluorescence photobleaching recovery measurements of red cell membrane protein lateral mobility.* Biophys J, 1994. 66(1): p. 25-30.

72. Nabeshima, K., A.M. Villeneuve, and M.P. Colaiacovo, *Crossing over is coupled to late meiotic prophase bivalent differentiation through asymmetric disassembly of the SC.* J Cell Biol, 2005. 168(5): p. 683-9.

73. Pflugrad, A., et al., *The Groucho-like transcription factor UNC-37 functions with the neural specificity gene unc-4 to govern motor neuron identity in C. elegans.* Development, 1997. 124(9): p. 1699-709.

74. Praitis, V., et al., *Creation of low-copy integrated transgenic lines in Caenorhabditis elegans.* Genetics, 2001. 157(3): p. 1217-26.

75. Hermann, G.J., et al., *Genetic analysis of lysosomal trafficking in Caenorhabditis elegans.* Mol Biol Cell, 2005. 16(7): p. 3273-88.

76. Wang, J.W., et al., *Two-Photon Calcium Imaging Reveals an Odor-Evoked Map of Activity in the Fly Brain.* Cell, 2003. 112(2): p. 271-282.

77. Stosiek, C., et al., *In vivo two-photon calcium imaging of neuronal networks.* Proceedings of the National Academy of Sciences of the United States of America, 2003. 100(12): p. 7319-7324.

78. Kimura, K.D., et al., *The C. elegans Thermosensory Neuron AFD Responds to Warming.* Current Biology, 2004. 14(14): p. 1291-1295.

79. Faumont, S. and S.R. Lockery, *The Awake Behaving Worm: Simultaneous Imaging of Neuronal Activity and Behavior in Intact Animals at Millimeter Scale.* J Neurophysiol, 2006. 95(3): p. 1976-1981.

80. Ben-Yakar, A., N. Chronis, and H. Lu, *Microfluidics for the analysis of behavior, nerve regeneration, and neural cell biology in C. elegans.* Current Opinion in Neurobiology, 2009. 19(5): p. 561-567.

81. Chronis, N., *Worm chips: Microtools for C. elegans biology.* Lab on a Chip. 10(4): p. 432-437.

82. Chokshi, T.V., A. Ben-Yakar, and N. Chronis, *CO2 and compressive immobilization of C. elegans on-chip.* Lab on a Chip. 9(1): p. 151-157.

83. Johnson, T.E., et al., *Longevity genes in the nematode Caenorhabditis elegans also mediate increased resistance to stress and prevent disease.* Journal of Inherited Metabolic Disease, 2002. 25(3): p. 197-206.

84. Wolkow, C.A., et al., *Regulation of C. elegans Life-Span by Insulinlike Signaling in the Nervous System.* Science, 2000. 290(5489): p. 147-150.

85. Mank, M., et al., *A FRET-based calcium biosensor with fast signal kinetics and high fluorescence change*. Biophys J, 2006. 90(5): p. 1790-6.

86. Bargmann, C.I., *Comparative chemosensation from receptors to ecology.* Nature, 2006. 444(7117): p. 295-301.

87. Foster, T.C., *Calcium homeostasis and modulation of synaptic plasticity in the aged brain.* Aging Cell, 2007. 6(3): p. 319-25.

88. Chalasani, S.H., et al., *Neuropeptide feedback modifies odor-evoked dynamics in Caenorhabditis elegans olfactory neurons.* Nature neuroscience. 13(5): p. 615.

89. Schafer, W., *Egg-laying*. WormBook, ed. T.C.e.R. Community. 2005: WormBook.

90. Horvitz, H.R., et al., *Serotonin and octopamine in the nematode Caenorhabditis elegans.* Science, 1982. 216(4549): p. 1012-4.

91. Trent, C., *Genetic and Behavioral Studies of the Egg-Laying System of Caenorhabditis elegans*. 1982: Massachusetts Institute of Technology, Cambridge, USA.

92. Stopfer, M., et al., *Impaired odour discrimination on desynchronization of odour-encoding neural assemblies.* Nature, 1997. 390(6655): p. 70-4.

93. Tanaka, N.K., K. Ito, and M. Stopfer, *Odor-evoked neural oscillations in Drosophila are mediated by widely branching interneurons.* J Neurosci, 2009. 29(26): p. 8595-603.

94. Mank, M., et al., *A genetically encoded calcium indicator for chronic in vivo two-photon imaging.* Nat Methods, 2008. 5(9): p. 805-11.

95. Chung K., C.M.M., and Lu H. in *the Proceedings of the Eleventh International Conference on Miniaturized Systems for Chemistry and Life Sciences (microTAS).* 2007. France.

96. Evans, T.C., *Transformation and microinjection* in *Wormbook*, T.C.e.R. Community, Editor. 2006.

97. Stiernagle, T., *Wormbook*, ed. T.*C.e.*R. Community.

98. Doty, R.W., *Electrical stimulation of the brain in behavioral context.* Annual Review of Psychology, 1969. 20(1): p. 289.

99. Histed, M.H., V. Bonin, and R.C. Reid, *Direct activation of sparse, distributed populations of cortical neurons by electrical microstimulation.* Neuron, 2009. 63(4): p. 508.

100. Asanuma, H., S.D. Stoney, and C. Abzug, *Relationship between afferent input and motor outflow in cat motorsensory cortex*. 1968. p. 670-681.

101. Salzman, C.D., et al., *Microstimulation in visual area MT: effects on direction discrimination performance*. 1992. p. 2331-2355.

102. Movshon, J.A. and W.T. Newsome, *Visual Response Properties of Striate Cortical Neurons Projecting to Area MT in Macaque Monkeys*. 1996. p. 7733-7741.

103. Moore, T. and M. Fallah, *Control of eye movements and spatial attention*. 2001. p. 1273-1276.

104. Testerman, R.L., M.T. Rise, and P.H. Stypulkowski, *Electrical stimulation as therapy for neurological disorders.* Engineering in Medicine and Biology Magazine, IEEE, 2006. 25(5): p. 74-78.

105. McCaig, C.D. and A.M. Rajnicek, *Electrical fields, nerve growth and nerve regeneration*. 1991. p. 473-494.

106. Shapiro-Ilan, D.I., et al., *Directional movement of steinernematid nematodes in response to electrical current.* Journal of Invertebrate Pathology, 2009. 100(2): p. 134-137.

107. ManiÃ¨re, X., et al., *Running Worms: C. elegans Self-Sorting by Electrotaxis.* PLoS ONE. 6(2): p. e16637.

108. Chokshi, T.V., D. Bazopoulou, and N. Chronis, *An automated microfluidic platform for calcium imaging of chemosensory neurons in Caenorhabditis elegans.* Lab on a Chip. 10(20): p. 2758-2763.

109. Phair, R.D. and T. Misteli, *Kinetic modelling approaches to in vivo imaging.* Nat Rev Mol Cell Biol, 2001. 2(12): p. 898-907.

110. Tsai, H., et al., *Intracellular Calcium Buffering Declines in Aging Adrenergic Nerves.* Neurobiology of Aging, 1997. 18(2): p. 229-233.

111. Murchison, D. and W.H. Griffith, *Calcium buffering systems and calcium signaling in aged rat basal forebrain neurons.* Aging Cell, 2007. 6(3): p. 297-305.

112. Campbell, L.W., et al., *Aging Changes in Voltage-Gated Calcium Currents in Hippocampal CA1 Neurons*. 1996. p. 6286-6295.

113. Koch, C., *Biophysics of computation: information processing in single neurons.* 1999.

114. Schutter, E.d., *Computational neuroscience: realistic modeling for experimentalists.* 2001.

115. Abbott, L.F. and P. Dayan, *Theoretical neuroscience: computational and mathematical modeling of neural systems.* 2001.

116. Markram, H., *The Blue Brain Project.* Nat Rev Neurosci, 2006. 7(2): p. 153-160.

117. Mak, T.S.T., et al., *A Component-Based FPGA Design Framework for Neuronal Ion Channel Dynamics Simulations.* Neural Systems and Rehabilitation Engineering, IEEE Transactions on, 2006. 14(4): p. 410-418.

118. Misha, M. and D. Rodney, *A Silicon Neuron.* Nature, 1991. 354(6354): p. 4.

119. Van Schaik, A., *Building blocks for electronic spiking neural networks.* Neural Networks, 2001. 14(6-7): p. 617-628.

120. Simoni, M.F., et al., *A multiconductance silicon neuron with biologically matched dynamics.* Biomedical Engineering, IEEE Transactions on, 2004. 51(2): p. 342-354.

121. Mead, C., *Analog VLSI and neural systems.* 1989.

122. Hopfield, J., *The effectiveness of analogue "neural network" hardware.* Network (Bristol), 1990. 1(1): p. 27-40.

123. Indiveri, G., et al., *Neuromorphic silicon neuron circuits.* Frontiers in Neuroscience, 2011.

124. Hynna, K.M. and K. Boahen, *Thermodynamically Equivalent Silicon Models of Voltage-Dependent Ion Channels*. 2007. p. 327-350.

125. Rachmuth, G. and C.S. Poon, *Transistor analogs of emergent iono-neuronal dynamics.* HFSP J, 2008. 2(3): p. 156-66.

126. Hodgkin, A.L. and A.F. Huxley, *A quantitative description of membrane current and its application to conduction and excitation in nerve*. 1952. p. 500-544.

127. FitzHugh, R., *Impulses and Physiological States in Theoretical Models of Nerve Membrane.* Biophysical journal, 1961. 1(6): p. 445-466.

128. Simoni, M.F., et al., *A multiconductance silicon neuron with biologically matched dynamics.* IEEE Trans Biomed Eng, 2004. 51(2): p. 342-54.

129. Linares-Barranco, B., et al., *A CMOS implementation of FitzHugh-Nagumo neuron model.* Solid-State Circuits, IEEE Journal of, 1991. 26(7): p. 956-965.

130. White, J.G., et al., *The Structure of the Nervous System of the Nematode Caenorhabditis elegans*. 1986. p. 1-340.

131. Lockery, S.R. and M.B. Goodman, *The quest for action potentials in C. elegans neurons hits a plateau.* Nat Neurosci, 2009. 12(4): p. 377-378.

132. Liu, Q., G. Hollopeter, and E.M. Jorgensen, *Graded synaptic transmission at the Caenorhabditis elegans neuromuscular junction*. 2009. p. 10823-10828.

133. Thiele, T.R., S. Faumont, and S.R. Lockery, *The Neural Network for Chemotais to Tastants in Caenorhabditis elegans is Specialized for Temporal Differentiation.* The Journal of neuroscience, 2009. 29(38).

134. Gray, P.R., et al., *Analysis and design of analog integrated circuits.* 2001.

135. Dunn, N.A., et al., *A Neural Network Model of Chemotaxis Predicts Functions of Synaptic Connections in the Nematode Caenorhabditis elegans.* Journal of Computational Neuroscience, 2004. 17(2): p. 137-147.

136. Achacoso, T.B. and W.S. Yamamoto, *AY's Neuroanatomy of C. elegans for Computation.* 1992.

137. Olsen, A., Vantipalli, M.C. and Lithgow, G.J., *Using Caenorhabditis elegans as a Model for Aging and Age-Related Diseases.* Annals of the New York Academy of Sciences, 2006. 1067: p. 120-128.